

NASA Technical Memorandum 100735

**Dynamic Sea Surface Topography,
Gravity, and Improved Orbit Accuracies
from the Direct Evaluation of SEASAT
Altimeter Data**

J. G. Marsh, F. Lerch, and C. J. Koblinsky
*NASA/ Goddard Space Flight Center
Greenbelt, Maryland*

S. M. Klosko, J. W. Robbins, R. G. Williamson,
and G. B. Patel
*ST Systems Corporation
Lanham, Maryland*

NASA

National Aeronautics and
Space Administration

Goddard Space Flight Center
Greenbelt, Maryland

1989

Contents

1	Introduction	1
2	Mathematical Model	3
2.1	Sea Surface Height, Dynamic Topography, and Ocean Circulation	3
2.2	The Altimeter Measurement	4
2.2.1	Using Orbital Data for Parameter Estimation	6
2.2.2	The Geopotential	7
2.2.3	The GEM-T1 Earth and Ocean Tide Models	7
2.2.4	The Geoid Height Calculation	9
2.2.5	Tides and Sea Level Variability	9
2.2.6	Summary of Altimeter Range Modeling	10
2.3	Modified Least Squares Method of Estimation	10
2.3.1	Altimeter and Surface Gravity Data Weights	16
2.3.2	The Solution and Its Statistics	16
3	The Altimeter Observations	18
3.1	SEASAT Data Selection Criteria	18
3.1.1	Overland Flagging	18
3.1.2	AGC Acceptance Criteria	18
3.1.3	High Degree Geoidal Mask	19
3.1.4	Elimination of Data from Shallow Seas and from Continental Shelves	19
3.1.5	Elimination of Regions of Poorer Ocean Tidal Modeling	19
3.1.6	Wet Troposphere Range Correction	21
3.1.7	Altimeter Data Noise	21
3.1.8	Data Selection Summary	21
3.2	SEASAT Data Correction Procedures	21

3.2.1	Correction for Sea-State Bias	22
3.2.2	Correction for High Degree Geoid Contributions	22
3.2.3	Recalculation of the Observation Uncertainty	23
3.3	Altimeter Bias Assessment	23
3.4	Altimeter Correction Errors	24
3.4.1	Atmospheric Refraction	24
3.4.2	Ionospheric Refraction	25
3.4.3	Geoid	25
4	Improved Gravity Field Model: PGS 3337	27
4.1	GEM-T1 Overview	27
4.2	SEASAT Altimetry	30
4.3	Surface Gravimetry	33
4.4	Improved Geoid Modeling	36
4.5	Gravity Model Extension to Degree and Order 50: Impact on Error Assessment	36
5	Dynamic Topography Solution	45
5.1	QSST from <i>in situ</i> Climatological Data ($\bar{\eta}_\rho$)	45
5.2	Definition of $\bar{\eta}_A$ with Respect to $\bar{\eta}_\rho$	46
5.3	The SEASAT Estimate of QSST ($\bar{\eta}_A$)	48
5.4	Error Estimates for $\bar{\eta}_A$	51
5.5	Separation of Ocean and Gravity Signals	54
5.6	Correlation Between Gravity and QSST Solutions	63
5.7	Importance of Signal Constraints	63
6	Gravity Model Performance	66
6.1	Orbital Tests Using Independent Laser/Doppler Observations	66
6.2	The Radial Accuracy of SEASAT	67

7	Conclusions	71
8	Acknowledgements	72
A	Normalized Harmonic Coefficients for Gravitational Model PGS-3337	A-1
B	Tidal Coefficients	B-1
C	Color Plates	C-1

List of Tables

1	Wahr Love Numbers for Earth Model 1066A	8
2	Rms Fit of SEASAT Altimeter Data Using: GEM-T1 for h_{sat} and $h_{N_{ref}}$ with $\bar{\eta}_\rho$. .	24
3	Rms Fit of SEASAT Altimeter Data Using: PGS-3337 for h_{sat} and $h_{N_{ref}}$ with $\bar{\eta}_A$. .	25
4	Data Utilized in the GEM-T1 gravity model	28
5	Spherical Harmonic Expansion of $\bar{\eta}_\rho$ by Engelis (1987)	46
6	Spherical Harmonics of $\bar{\eta}_\rho$ - Set III in Table 5	46
7	Comparison of $\bar{\eta}_{A_{ann}}$ and $\bar{\eta}_{\rho_{ann}}$	47
8	Gravity Model Testing Using Orbital Tracking Observations	67
9	SEASAT Altimeter Crossover Analysis: Estimate of Nongeographically Correlated Radial Orbit Error From Recent GSFC Gravitational Models	68
A1	Zonal Coefficients*	A-2
A2	Sectorial and Tesseral Coefficients*	A-3
B1	Ocean Tidal Coefficient Recovery for PGS-3337	B-2

List of Figures

1	Altimeter measurement model.	11
2	Fit to Engelis (1987) harmonics for $\bar{\eta}_\rho$ to form QSST power law.	15
3	Dynamic ocean topography relative to a 2250 db reference surface - $\bar{\eta}_\rho$ (Levitus, 1982).	20
4	A comparison of GEM-T1 and GEM-L2 calibrated rms coefficient errors by degree.	29
5	A comparison of GEM-T1 and PGS-3337 error estimates.	31
6	A comparison of PGS-3337 and GEM-T1 calibrated rms coefficient errors by degree.	32
7	(a) A map of the SEASAT observations utilized in PGS-3337 from July 28 - August 15, 1978. (b) A map of the SEASAT observations utilized in PGS-3337 during the 3 day repeat orbit.	34
8	(a) The PGS-3337 data sample locations. In total, 48,955 $1^\circ \times 1^\circ$ equi-angular mean anomalies were used. (b) Geophysically predicted anomalies of the June 1986 field.	35
9	(a) Coefficient by coefficient estimate of the uncertainties for GEM-T1. (b) Coefficient by coefficient estimate of the uncertainties for PGS-3337.	37
10	The uncertainty in global geoid height from the complete covariance propagation using GEM-T1 only (top) or GEM-T1 plus surface gravimetry (bottom).	38
11	The uncertainty in global geoid height from the complete covariance propagation using GEM-T1 plus SEASAT altimetry (top) or PGS-3337 (bottom).	39
12	(a) The geoid uncertainties for the 10×10 degree and order portions of the GEM-T1 model. (b) The geoid uncertainties for the 10×10 degree and order portions of the PGS-3337 model.	40
13	The power spectrum for $\bar{\eta}_A$ from PGS-3337 and $\bar{\eta}_\rho$	41
14	A comparison of the PGS-3325 and PGS-3337 rms coefficient errors by degree.	44
15	The QSST model from PGS-3337 after the correction for the permanent tides.	49
16	The 10×10 harmonic representation of $\bar{\eta}_\rho$	50
17	The geostrophic flow implied by $\bar{\eta}_{A_{ann}}$ from PGS-3337.	52
18	The geostrophic currents implied from $\bar{\eta}_{\rho_{ann}}$	53
19	The covariance estimate of the geographical PGS-3337 QSST errors for the correlated $\bar{\eta}_{A_{ann}}$ using a contour interval of 5cm.	55

20	PGS-3337 QSST error, where only the ocean area is presented and a 1.0 cm contouring interval is used.	56
21	Histogram of the calibration factors k_{lm} for the combination gravity fields containing altimetry and surface gravimetry (PGS-3325 and PGS-3339).	58
22	The ratio of the condition numbers for the PGS-3325 and PGS-3339 36×36 gravitational solutions.	60
23	The reduction of the error variances of PGS-3339 with PGS-3325.	61
24	The effect on the rms coefficient errors by degree in the PGS-3325 versus PGS-3339 solutions.	62
25	The correlation between $\bar{\eta}_\rho$ and $h_{N_{ref}}$ from PGS-3337.	64
26	The geographical distribution of the crossover misclosures that result when using PGS-3337 and the Doppler/altimeter data sets.	69

Acronyms

AGC	Automatic Gain Control
CNES	Centre Nationale d'Etudes Spatiale (FRANCE)
EM	Electro-Magnetic
ERS-1	ESA Earth Resources Satellite
ESA	European Space Agency
FNOC	U.S. Navy Fleet Numerical Ocean Center
GDR	Geophysical Data Record
GEM	Goddard Earth Model
GEOS	Geodynamic Experimental Ocean Satellite
GEOSAT	U.S. Navy GEOdetic SATellite
GEOSAT ERM	GEOSAT Exact Repeat Mission
GSFC	NASA Goddard Space Flight Center
IAG	International Association of Geodesy
IAU	International Astronomical Union
IUGG	International Union of Geodesy and Geophysics
JPL	Jet Propulsion Laboratory of the California Institute of Technology
LAGEOS	LAser GEOdynamics Satellite
MERIT	Monitoring Earth Rotation and Intercomparison of Techniques
MODE	Mid-Ocean Dynamics Experiment
NASA	National Aeronautics and Space Administration
NMC	U.S. National Meteorological Center
OSU	Ohio State University
PGS	Preliminary Gravity Solution
QSST	Quasi-stationary Sea Surface Topography
RMS	Root Mean Square
SEASAT	NASA Oceanographic (SEA) Research SATellite
SMMR	Scanning Multichannel Microwave Radiometer
TOPEX	NASA/CNES Ocean TOPography EXPeriment
TRANET	TRacking NETwork
WOCE	World Ocean Circulation Experiment

Mathematical Symbols

a_e	Earth's semi-major axis for its reference ellipsoid
ΔD	dynamic height of the ocean relative to a reference state
f_c	Coriolis parameter
g	local gravitational acceleration
G	gravitational constant
h	the sea surface height relative to a reference ellipsoid
h_{alt}	observed altimeter range
Δh_{alt}	altimeter instrument and environmental corrections
h_B	altimeter bias
h_N	the geoid height relative to a reference ellipsoid
h_{sat}	radial height of a satellite relative to a reference ellipsoid
h_{T_0}	the geocentric body tide relative to a reference ellipsoid
Δh_W	sea state bias in the altimeter measurement
h_e	altimeter instrument noise
$k_{2,f}$	Love numbers
M_e	the mass of the Earth
p	pressure in the ocean
p_a	pressure of the atmosphere at the ocean surface
p_b	pressure at the bottom of the ocean
r	the geocentric satellite distance
s	salinity of the ocean
T	Temperature of the ocean
T	disturbing potential of the Earth
u_g, v_g	east/west and north/south geostrophic ocean currents
U_s	the static geopotential of the Earth
$W_{\frac{1}{3}}$	significant wave height of the ocean
x, y, z	local east/west, north/south, and vertical coordinates
α	the specific volume of the ocean
γ	normal value of gravity on a reference ellipsoid
ρ	density in the ocean
ρ_0	mean ocean density
$\delta_{2,f}$	Love number phase
η	height of the air-sea interface with respect to the geoid
η_a	the atmospheric load contribution to η
η_A	the altimeter derived model of η
η_b	the barotropic contribution to η
η_T	the ocean tidal contribution to η
η_T	the solid Earth tidal contribution to η
η_ρ	the steric contribution to η
λ	the satellite east longitude
ϕ	the satellite geocentric latitude

1 Introduction

One of the major goals of oceanography is to determine the global ocean circulation. Satellite altimetry, in conjunction with accurate knowledge of the Earth's gravitational field and the ocean's density field, can provide a significant step towards this goal (Wunsch and Gaposchkin, 1980). However, before major advances can be made with this observational system, a number of hurdles must be overcome in order to reduce the errors to an acceptable level. This document examines the ability of altimeter technology on the NASA Oceanographic (SEA) Research Satellite (SEASAT) to determine the mean shape of the dynamic sea surface. A new solution technique is presented where simultaneously the dynamic topography and the gravity field are solved. In addition, the altimeter data is used in the solution for the satellite position.

Near-Earth satellites have intermittently flown radar altimeters since the 1973 experiment on the NASA SKYLAB. The altimetric ranging acquired by SKYLAB and, in 1975 to 1978 by the NASA Geodynamics Experimental Ocean Satellite (GEOS-3), were harbingers of an era in physical oceanography when space-based technologies will observe worldwide oceanographic processes. With the launch of SEASAT in 1978, spaceborne altimeters acquired ocean surface topography at wavelengths greater than 40 km (Brammer and Sailor, 1980). A cost-effective role of altimetry was established for detecting the surface topography of the oceans and for providing previously inaccessible gravitational information. The U.S. Navy Geodetic Satellite (GEOSAT) launched in 1985 is currently providing a wealth of new altimetry measurements. The European Space Agency's (ESA) Earth Research Satellite (ERS-1, launch in 1990) and USA/France Ocean Topography Experiment (TOPEX/Poseidon, launch in 1992) missions will ensure an abundance of altimetric observations for the next decade.

The space-borne radar altimeter maps a sea surface that is far more complex than the attenuated gravity field at altitude. This sea surface resembles the equipotential gravitational surface known as the geoid. However, the sea surface departs by a few percent from the geoid, and these anomalies reflect the ocean circulation patterns.

The general circulation of the ocean is Quasi-stationary (Q-) in character, and this is reflected in the Sea Surface Topography (SST). Stable highs and lows are found in the QSST that are associated with the major circulation features of the ocean. The QSST component in the altimeter-mapped surface is small (1.5 m) in comparison to variations in the geoid (± 100 m), and it is difficult to separate from the geoid over the same spatial dimensions. The gravitational and oceanographic problems are entwined with shared signals over a large range of spatial wavenumbers. Some of these signals are effectively decoupled because of their temporal variability, but others are not. Unfortunately, many of the important insights sought from the altimetry, about the general circulation of the oceans, remain largely obscured by imperfect knowledge of the geoid. Any improvement made in the gravitational models directly improves the isolation of the oceanic signal at these wavelengths and the accuracy of the orbital reference for the altimeter measurements.

This document describes a model for the mean global ocean dynamic topography from SEASAT altimeter data. The QSST has been represented as a spherical harmonic series truncated at a degree and order at which expected geoid errors exceed the amplitude of the QSST. Mather *et al.* (1978) gave one of the earliest numerical results for this dynamic surface by comparing altimetric and

geoidal surfaces. This work provided estimates of a few zonal harmonic terms for the QSST. Tai and Wunsch (1983) used an improved gravitational model (Goddard Earth Model (GEM) - L2, Lerch *et al.*, 1982a, and Lerch *et al.*, 1985) in determining a map of the QSST within the Pacific basin with a resolution of approximately 20°. Cheney and Marsh (1982) attempted a similar approach comparing the Goddard Space Flight Center (GSFC) altimetric mean sea surface, which combined GEOS-3 and SEASAT data, and the GEM-L2 geoid. Engelis (1985) used GEM-L2 and a mean sea surface of Rapp (1982, 1985) and produced a model for QSST in spherical harmonics complete to degree and order 6. Tai and Wunsch (1984) combined the geoid information from GEM-L2 with the Preliminary Gravity Solution-S4 (PGS-S4, see Lerch *et al.*, 1982b). PGS-S4 is a gravitational model that utilized SEASAT altimetry to help reduce geoid errors arising in terms above degree and order 6. More recently, Tai (1988) has incorporated the latest GSFC gravitational model GEM-T1 (Marsh *et al.*, 1987). Recently, Tapley *et al.* (1988) and Engelis and Knudsen (1989) have published an analysis of the SEASAT dynamic topography which parallel, somewhat, the activity described in this document. The dominant errors in all of the previous cited QSST determinations were the uncertainties in the geoid and the radial positioning of the satellite.

The present solution departs markedly from most of the analyses previously cited in that a simultaneous solution was performed for the invariant and tidally perturbed gravitational field, the satellite orbits including SEASAT, and the QSST directly from the altimeter, laser, optical, and doppler observations acquired on 17 unique satellite orbits. This solution is an outgrowth of the work being performed at GSFC to develop advanced gravitational models in preparation for the TOPEX Mission. GEM-T1 (Marsh, *et al.*, 1987, 1988) is the first of a new series of GSFC models that will be produced for TOPEX. GEM-T1 has now been extended through the inclusion of surface gravimetry and SEASAT altimetry to estimate along with the other parameters in the solution, a model of the QSST that is complete to degree and order 10. This new solution, PGS-3337, is a preliminary version of GEM-T3. PGS-3337, unlike GEM-T1, is complete in harmonics to degree and order 50.

2 Mathematical Model

The effects of the gravitational field of the Earth dominate the altimeter signal. The geopotential perturbs the spacecraft orbit changing its height above the oceans by about 5 km. Additionally, the geoid signal accounts for over 95% of the deviation of the ocean surface from the ellipsoid. This signal is quite strong in satellite altimeter measurements, which have a precision of a few centimeters. Therefore, the altimeter observations can make a significant contribution to gravitational model development and provide an important resource of satellite tracking information over remote ocean regions far removed from land-based tracking systems. Separating a gravitational signal from these measurements requires, at a minimum, detailed modeling of the non gravitational signal (*i.e.*, oceanographic) embedded within the altimeter range observations. This section describes the simultaneous solution technique for the gravitational potential, the geoid, dynamic sea surface topography and satellite ephemeris from satellite altimeter data.

2.1 Sea Surface Height, Dynamic Topography, and Ocean Circulation

The height of the air-sea interface (η) with respect to the geoid is related to the general circulation of the ocean through the hydrostatic relation

$$\frac{\partial p}{\partial z} = -g\rho \quad (1)$$

and the geostrophic momentum equations

$$u_g = -\frac{1}{f_c \rho} \frac{\partial p}{\partial y} ; \quad v_g = \frac{1}{f_c \rho} \frac{\partial p}{\partial x} \quad (2)$$

where:

- p ocean pressure
- g local gravitational acceleration
- ρ density of sea water
- f_c Coriolis parameter
- u_g, v_g east/west and north/south geostrophic currents
- x, y, z local east/west, north/south, and vertical coordinates

Integrating Equation (1) from a depth z_0 to the ocean surface, yields

$$\eta - \eta_a = \frac{1}{g\rho_0} p(z = z_0) - \frac{1}{\rho_0} \int_{z_0}^0 \rho dz \quad (3)$$

Where the atmospheric load on the ocean is defined as ($\eta_a = -\frac{1}{g\rho_0} p_a$), p_a is sea level pressure, and ρ_0 is the mean density.

In order to isolate the non gravitationally forced variations in sea level caused by the ocean circulation, the ocean tides (η_T) were removed from $\eta - \eta_a$. Let η' be the ocean surface height with respect to the geoid after removing atmospheric load and tidal contributions ($\eta' = \eta - \eta_a - \eta_T$).

Then, the mean value of η' represents sea level change caused by the general circulation (QSST $\equiv \bar{\eta}'$). It is assumed that the mean is for the time period of the observations. For notational convenience in the remainder of this document, the prime will be dropped and QSST will be denoted as $\bar{\eta}$. Note that the surface geostrophic currents can be obtained from Equations (2) and (3) when $z_0 = \eta$ as

$$u_g = \frac{g}{f_c} \frac{\partial \eta'}{\partial y}; \quad v_g = -\frac{g}{f_c} \frac{\partial \eta'}{\partial x} \quad (4)$$

Dynamic topography has been estimated for years with *in situ* measurements using a form of Equation (3) (Sverdrup *et al.*, 1946, Chapter XII). In this model, the assumed relationship between η' and the interior ocean is

$$\eta' \simeq \eta_\rho = -\frac{1}{\rho_0} \int_{z_0}^0 \rho dz \quad (5)$$

The integration variable on the right-hand side is changed to pressure to form

$$\Delta D = \int_{p_{ref}}^p [\alpha(s, T, p) - \alpha(3.5\%, 0^\circ, p)] dp \quad (6)$$

Where α is the specific volume and ΔD is the dynamic height in dynamic meters (units of work per unit mass) relative to a reference state. The reference state is defined by a temperature (T) of 0°C and a salinity (s) of 35 parts per thousand. Dynamic height is the geopotential distance between two pressure surfaces in the ocean. The dynamic meter is defined such that the magnitude of 1 dyn-m is about 1 m of vertical displacement ($\eta_\rho = 10 \int_0^D \frac{1}{g} dD$). The barotropic contribution ($\eta_b = \frac{1}{g\rho_0} p_b$, where p_b is bottom pressure) is assumed negligible, and the reference surface or 'surface of no motion' (p_{ref}) is assumed to be a geopotential.

The sea surface height of the ocean relative to the geoid (η) has been commonly measured with tide gauges, relative to a local coordinate system, under the assumption that the geoid is coincident with mean sea level. Comparative studies of the temporal variations in η and D (the baroclinic contribution to sea level) have been made at a few locations with *in situ* measurements (*e.g.*, Wunsch, 1972; Tabata *et al.*, 1986). Generally, these comparisons show a strong correlation between η and D . Evaluation of the barotropic contribution (η_b) has been rare because of the difficulty in measuring pressure at great depths (Brown *et al.*, 1975). However, direct measurements (Hallock *et al.*, 1989) and diagnostic models (Gill and Niiler, 1973) suggest that $|\eta_b| \ll |\eta_\rho|$ at most locations.

2.2 The Altimeter Measurement

The power of satellite altimeter measurements comes from the ability to obtain both mean and temporal measurements of η on a global basis, relative to a global coordinate system, from the relationship

$$\eta = h - h_{T_g} - h_N \quad (7)$$

where h is the sea surface height derived from the altimeter, h_{T_g} is the geocentric body tide, and h_N is the geoid height, all relative to a reference ellipsoid surface of the Earth.

The altimetric range is used to measure the instantaneous sea surface height. The satellite altimeter measurement is given by:

$$h = h_{sat} - (h_{alt} + \Delta h_{alt} + h_{\epsilon} - h_B) \quad (8)$$

where:

- h sea surface height above the reference ellipsoid
- h_{sat} radial height of the satellite orbit defined as the distance from the center of mass of the satellite to the Earth's ellipsoid
- h_{alt} the observed altimeter range corrected for instrument offsets from the sea surface to the satellite center of mass
- Δh_{alt} instrument and environmental corrections
- h_{ϵ} the instrument noise, which was about 10 cm rms for SEASAT
- h_B bias that results from both the invariant bias in the altimeter instrument and error in the knowledge of the Earth's semi-major axis for its reference ellipse (a_e)

The reference ellipsoid is defined, in the model, by $a_e = 6378137$ m and $1/\text{flattening} = 298.257$.

Using Equations (3), (7), and (8), η' is related to the altimeter measurements by

$$\eta' = h_{sat} - (h_{alt} + \Delta h_{alt} + h_{\epsilon} - h_B) - (h_{N_{ref}} + h_{\Delta N}) - h_{T_g} - \eta_T - \eta_a \quad (9)$$

where the geoid has been separated as $h_N = h_{N_{ref}} + h_{\Delta N}$. In the model, $h_{N_{ref}}$ is a reference gravitational model geoid of maximum spherical harmonic degree and order l_{max} . $h_{\Delta N}$ is the residual geoid height from l_{max+1} to l_{∞} .

The altimetric derived model for $\bar{\eta}$, hereafter denoted as $\bar{\eta}_A$, will be obtained as a surface spherical harmonic series

$$\bar{\eta}_A = \sum_{n=0}^{n_1} \sum_{m=0}^n \sum_{\alpha=1}^2 \bar{\eta}_{A_{\alpha mn}} S_{\alpha mn} \quad (10)$$

and:

$$S_{\alpha mn} = \begin{cases} P_n^m(\sin \phi) \cos m\lambda & \alpha = 1 \\ P_n^m(\sin \phi) \sin m\lambda & \alpha = 2 \end{cases} \quad (11)$$

where $\bar{\eta}_{A_{\alpha mn}}$ are the harmonic coefficients of $\bar{\eta}_A$, and n_1 corresponds to the limiting wavelength, which in practice is restricted by the presence of geoid errors.

A spherical harmonic series behaves best when it is determined from complete global coverage over the bounding sphere (because of its orthogonality properties). The SEASAT data provide a dense observational base for computing $\bar{\eta}_A$ over the ocean surface. However, data coverage was restricted from 72° N to approximately 66° S latitude because of orbit inclination and ice coverage in the Southern Hemisphere. Data were not available over the land surfaces. Therefore, mathematical stabilization of the $\bar{\eta}_{A_{\alpha mn}}$ were required. A form of least squares collocation (Moritz, 1980) was used to control the power in the recovered coefficients. This approach reduces the modeling instability over areas lacking data. However, the $\bar{\eta}_{A_{\alpha mn}}$ have no meaning over land areas, nor are they useful for assessing $\bar{\eta}$ over regions that have not been sampled by the SEASAT altimetry (i.e., areas masked out in the data selection procedures).

Equation (9) shows that accurate knowledge of the orbital position (h_{sat}), geoid (h_N), tides (h_{Tg}, η_T), measurement corrections ($\Delta h_{alt}, h_B$, and η_a), and temporally varying ocean surface ($\langle \eta \rangle$) are required to successfully model $\bar{\eta}$. Some of these accuracy requirements are addressed in the following paragraphs.

2.2.1 Using Orbital Data for Parameter Estimation

The orbit ephemeris (h_{sat}) is obtained from a numerical integration of the equations of motion taking into account the variety of forces that perturb the satellite's orbit (Martin *et al.*, 1985). Orbital state parameters are adjusted to minimize the misclosure between tracking observations and the calculated position of the satellite over a specified arc length. The orbital state parameters include epoch position and velocity, as well as empirical terms that are used to scale nonconservative forcing effects (*e.g.*, atmospheric drag and solar radiation pressure effects). The adjustment is iterated to convergence through minimization of the weighted observation residuals. If several separate satellite orbits are simultaneously evaluated over a wide range of inclinations, mean motions, and eccentricities, further adjustments can be performed on the global conservative force models. The Goddard Earth Models, as well as other satellite derived geopotential and tidal models, are developed in this way (Marsh *et al.*, 1988).

The inertial orbital position of the satellite, X_t , at time t , is a function of the initial state position of the satellite, X_e , and the force model used to integrate the orbit. A simplified form showing how the observations affect the adjustment of the orbit and non-orbit parameters is given by

$$\delta r = \frac{\partial O}{\partial P} \Delta P + \frac{\partial O}{\partial X_t} \frac{\partial X_t}{\partial X_e} \Delta X_e \quad (12)$$

The observation residuals, δr , are to be minimized. $\frac{\partial O}{\partial P}$ are the partial derivatives of the observations with respect to a large number of station, geodynamic and Earth orientation parameters. $\frac{\partial O}{\partial P}$ are the differential corrections to these and the orbital state parameters, ΔP and ΔX_e , required to minimize δr .

Many forces included in the parameters P act on the satellite and require modeling to meet the precise orbit computation goals of present and future altimeter missions. The satellite accelerations (\ddot{R}) are calculated from an evaluation of numerous forcing effects (Marsh, *et al.*, 1988)

$$\ddot{R} = \ddot{R}_{PM} + \ddot{R}_{at} + \ddot{R}_{tide} + \ddot{R}_{drag} + \ddot{R}_{rad} + \ddot{R}_{io} + \ddot{R}_T \quad (13)$$

where:

- \ddot{R}_{PM} the point mass effects of the Earth, Moon, Sun and i planets
- \ddot{R}_{at} along track accelerations
- \ddot{R}_{tide} accelerations from the tide model
- \ddot{R}_{drag} drag force accelerations
- \ddot{R}_{rad} accelerations from the solar radiation pressure
- \ddot{R}_{io} the indirect oblateness effects because of the relative acceleration of the satellite with respect to the Moon
- \ddot{R}_T additional acceleration arising from the gravitational disturbing potential

The minimization of δr is done within a least squares adjustment. This adjustment is complicated by imperfect models, algorithms and unknown systematic sources of error. If many geodynamical parameters are to be recovered then global tracking data, a dense sampling of orbits, and high data accuracy are required to achieve physically meaningful results. Discussions of the orbit problem for altimeter analyses are given by Colombo (1984), Tapley and Rossborough (1985), Wagner (1985), Born *et al.*(1988), and Engelis (1988).

2.2.2 The Geopotential

The geopotential consists of both a static part, that is defined by the unperturbed mass distribution of the Earth, and a dynamic part, commonly known as the indirect tidal potential. This latter part results from the mass deformation of the Earth caused by the gravitational forces of the Sun and the Moon. Both parts are considered and have been improved upon as a result of the GEM-T1 analysis where a simultaneous solution was made for spherical harmonic coefficients of both the static and tidal potential. In this document, it is shown how this solution, through the addition of surface gravimetry and SEASAT altimetry, is extended to include the estimation of $\bar{\eta}_A$ and the simultaneous improvement of the static geopotential. The non-gravitational and dynamic tidal models, that are used as *a priori* in the analysis, are those of GEM-T1.

The static geopotential is represented herein in classical spherical harmonics form by:

$$U_s = \frac{GM_e}{r} \left\{ 1 + \sum_{l=2}^{l_{max}} \sum_{m=0}^l \left[\frac{a_e}{r} \right]^l \tilde{P}_l^m(\sin \phi) [\tilde{C}_{lm} \cos(m\lambda) + \tilde{S}_{lm} \sin(m\lambda)] \right\} \quad (14)$$

where:

G	the gravitational constant
M_e	the mass of the Earth
r	the geocentric satellite distance
ϕ	the satellite geocentric latitude
λ	the satellite east longitude
\tilde{P}_l^m	the associated Legendre functions of the first kind
$\tilde{C}_{lm}, \tilde{S}_{lm}$	the geopotential coefficients

Here, the use of the tilde indicates normalized harmonics. The geopotential forces are computed as the gradient of the potential.

2.2.3 The GEM-T1 Earth and Ocean Tide Models

Geopotential models have become more accurate as data and computer capabilities have improved. Consequently, basic assumptions about the overall description of the gravitational model as a time invariant set of terms that require augmentation of only a simple modeling of luni-solar tidal effects (*e.g.*, GEM-L2) have been substantially modified in recent solutions. The GEM-T1 solution included parameters for additional spherical harmonic terms describing the temporal variation of the field at the main tidal frequencies.

Table 1: Wahr Love Numbers for Earth Model 1066A

Band	Tidal Line	$k_{2,f}$
Long Period	All	0.299
Diurnal	145555 (O_1)	0.298
	163555 (P_1)	0.287
	165545	0.259
	165555 (K_1)	0.256
	165565	0.253
	166554 (PSI)	0.466
Semi-diurnal	All	0.302

The ocean tidal model for the force model calculations consisted of over 600 individual coefficients, many of which were estimated from oceanographic models using linear admittances (Christodoulidis *et al.*, 1986) since they were unavailable from oceanographic sources. These terms represented the longest wavelength components of 32 major and minor tidal lines. Of the 600 values, 66 tidal terms were simultaneously adjusted within the solution representing dynamic corrections based upon observed orbital behavior for 12 major tidal frequencies.

The tidal recovery was made in the presence of the Wahr (1979, 1981) frequency-dependent solid Earth tidal model. Table 1 gives the Love numbers ($k_{2,f}$) computed by Wahr based upon the Earth model 1066A of Gilbert and Dziewonski (1975). The Wahr model was developed assuming a uniformly rotating Earth composed of an elastic inner core and mantle, as well as a liquid core. Note that the phase angle is zero for the Wahr model; that is, the model is free of dissipation. These solid Earth Love numbers fully characterize the response of the 1066A Earth to the nonloading tide-generating potential. $k_{2,f}$ and $\delta_{2,f}$ are the Love numbers and phases that describe the body response of the Earth at different frequencies, f .

If the Earth's response lacked any frequency dependence then:

$$k_{2,f} \equiv k_2; \quad \delta_{2,f} \equiv \delta_2 \quad (15)$$

for each constituent f associated with unique tidal frequencies. Then the total body tide potential could be simply computed in the time domain using the potential:

$$U_B = \sum_d \frac{k_2}{2} \frac{\mu g a_e^2}{r_d^3} \left[\frac{a_e}{r} \right]^3 \left[\left(\frac{r_d \cdot r}{r_d r} \right)^2 - 1 \right] \quad (16)$$

where r_d is the geocentric vector to the Sun or Moon and μ is the gravitational constant for the Sun or Moon.

All of the remaining solid Earth tidal frequencies were modeled with this frequency-independent model with a Love number $k_2 = 0.30$ with zero phase. This includes the zero-frequency tides

($f = 0$). For reasons of computational efficiency, this basic background model was used with deviations from Table 1 individually modeled. Therefore, the resulting GEM/PGS gravity fields and their geoid do not contain this permanent body tidal deformation. This is consistent with the International Association of Geodesy (IAG)'s 1980 resolution on modeling the permanent tide but disagrees with the Report of the Special Study Group No. 5.39 of the IAG on Fundamental Geodetic Constants (Rapp, 1983a,b). Study Group No. 5.39 recommends that the zonal harmonics of the gravitational solution contain at least part (*i.e.*, the part dependent on the secular Love number) of this permanent tidal deformation. The treatment of the $f = 0$ body tidal contribution as it applies to $\bar{\eta}_A$ is discussed in Section 5.

2.2.4 The Geoid Height Calculation

The geoidal height ($h_{N_{ref}}$) given in Equation (9) is obtained from the gravitational model by Brun's formula

$$h_{N_{ref}} = \frac{T}{\gamma} \quad (17)$$

where T is the disturbing potential referred to an ellipsoid through the removal from U_s in Equation (14) of the ellipsoidal parts of the C_{20} , C_{40} , and C_{60} zonal harmonics and γ is the normal value of gravity on the ellipsoid.

In the implementation of Equation (9), a high degree and order gravitational model (Rapp and Cruz, 1986) was used to compute $h_{\Delta N}$. All terms in this model for ($51 \leq l \leq 300$) were used in Equations (14) and (17) to calculate the value of $h_{\Delta N}$. This computation was performed using a spherical approximation (Rizos, 1979). This and other correction/masking algorithms will be more fully discussed in Section 3.

2.2.5 Tides and Sea Level Variability

In the altimeter treatment, Section 3, some algorithms and tests are described that were employed to control the quality of the corrections in Equation (9). Taken individually:

h_T , The solid Earth tides were determined using an algorithm presented in the Monitoring Earth Rotation and Intercomparison of Techniques (MERIT) Standards (Melbourne *et al.*, 1983) for station tidal displacements.

η_T The ocean tidal corrections were computed using the models developed by Schwiderski (1980, 1981, 1983) for the M_2 , S_2 , N_2 , K_2 , O_1 , P_1 , and K_1 frequencies. An independent set of models (Parke, 1982) were used to check the Schwiderski values. Plate 1b (the color plates are shown in Appendix C at the end of the document) presents the instantaneous ocean tide differences between the Schwiderski and Parke models at the SEASAT sampled subsatellite points. In certain regions, like the Gulf of Alaska, the models disagree on the average by more than 50 cm.

(η) The nontidal ocean variability in h could not be modeled out of the data. However, the complete SEASAT data span was sampled, and these effects were averaged out as best as possible. Plate 1c presents a map of $\langle\eta\rangle$ from an analysis of the SEASAT data using colinear pass analyses (Cheney *et al.*, 1983). Furthermore, the restricted geographical extent of features such as western boundary currents would not be represented by the wavelengths in the present solution for $\bar{\eta}_A$.

2.2.6 Summary of Altimeter Range Modeling

The altimeter range residual obtained from *a priori* models, as in Equation (9), is minimized through parameter adjustment in the least squares solution. The ocean and solid Earth tides (η_T and h_{T_g}) are kept fixed. The satellite range (h_{sat}), the geoid height ($h_{N_{ref}}$), the altimeter bias (h_B), and the quasi-stationary sea surface height ($\bar{\eta}_A$) are all simultaneously adjusted as shown in Figure 1.

2.3 Modified Least Squares Method of Estimation

A modified least squares technique was used as part of the solution procedure to achieve improved conditioning for the gravitational and QSST models. This technique utilizes *a priori* power spectrums that serve as a form of constraint on the behavior of the adjusting coefficients. The estimation technique employed is analogous to the least squares collocation method of Moritz (1980). This correspondence has been previously shown in Lerch *et al.* (1977, 1988). Its effect on the solution stability is thoroughly discussed in Marsh *et al.* (1988). Only a brief review of the material is presented here.

The principal of the method is to minimize the quadratic norm, Q , combining signal and noise with respect to the unknowns y (Lerch *et al.*, 1988 eq. 3.1 and Moritz, 1980, eq. 21.38)

$$Q = z^T K^{-1} z + n^T D^{-1} n \quad (18)$$

where:

- y the complete set of solution parameters for the geopotential, satellite tracking stations, Earth orientation, dynamic tides, orbits, and $\bar{\eta}_A$.
- n the adjusted satellite tracking, gravity anomaly, and altimetry data residuals.
- D a diagonal matrix for the satellite observation residuals whose diagonal elements represent the weighted variances of the observations.
- z the signal, that consists of the harmonic coefficients for the geopotential model and $\bar{\eta}_{A_{ann}}$, representing a subset of y , with an *a priori* value of zero.
- K a diagonal matrix where the elements are the expected variances of the coefficients for the geopotential and $\bar{\eta}_A$.

For simplicity, and to aid in a discussion of data weighting and solution conditioning, Equation

Form of Altimeter Observation Equation

$$A_{\text{range}} = R - (N + \bar{\eta} + T) + B$$

Where:

- R is radial distance of satellite to Earth's ellipsoid: *Adjusted*
- N is geoid height from reference model: *Adjusted*
- $\bar{\eta}$ is quasi-stationary sea surface height: *Adjusted*
- T is tidal correction - Schwiderski ocean, MERIT solid Earth: *Fixed*
- B is altimeter bias accounting for instrument errors and Δa_e : *Adjusted*
- A is the altimeter range corrected for media, high order geoid, sea state and off nadir effects

Figure 1. Altimeter measurement model.

(18) can be rewritten as:

$$Q = \epsilon_1 \sum_l \sum_m \frac{C_{lm}^2 + S_{lm}^2}{\sigma_{lm}^2} + \epsilon_2 \sum_a \sum_n \sum_m \frac{\bar{\eta}_{A_{anm}}^2}{\sigma_{anm}^2} + w_j \sum_j \sum_i \frac{\delta r_{ij}^2}{\sigma_{ij}^2} \quad (19)$$

where:

- σ_{lm}^2 the coefficient variances for C_{lm}, S_{lm} .
- σ_{anm}^2 the coefficient variances for $\bar{\eta}_{A_{anm}}$.
- δr_{ij} the i -th tracking residual from the j -th homogeneous data subset (e.g., laser ranging on the LAsER GEODynamic Satellite (LAGEOS), altimeter ranging from SEASAT and surface gravity anomalies).
- ϵ_1, ϵ_2 calibration factors that compensate for errors in the nominal solution conditioning power laws.
- σ_{ij}^2 the preliminary variances given to the i -th observation of the j -th data set. These variances are usually constant for all observations in the j -th subset. While $\sigma_{ij}^2 = \sigma_j^2$ for most data sets, the i subscript is used to signify that the solution observations can receive individualized weights. In PGS-3337, certain laser systems exhibiting high-noise levels had their observations downweighted and all surface gravity anomalies received individual weights reflecting their variable accuracy.
- w_j the balance of relative weights of the individual data subsets, taking into account such factors as the *a posteriori* rms of fit to these subset observations. However, while the *a posteriori* rms is an important indicator of problematic data, optimal values for w_j have been found that deviate by as much as a factor of 50 or more from this rms weighting scheme.

In the ideal case, $[\sum \frac{\delta r_{ij}^2}{\sigma_{ij}^2} \div \text{num}]$ approaches unity within a least squares adjustment. This is common when the observations are unbiased, uncorrelated, and the σ_{ij}^2 reflect the noise within the observations. However, the problem discussed in this document does not conform to an ideal case. The solution suffers from systematic data errors, imperfect environmental data corrections, imperfect and unmodeled force effects, and other problems of varying origin/magnitude where precise observations (the laser ranges) only fit within a factor of 3 to 10 of their pass-by-pass (bias-free) noise assessment. These problems cause optimization of data weights to be a major undertaking, and data noise has only a modest impact on the final data weights obtained in the gravitational solutions.

Since satellite orbital characteristics are variable, some of the satellites experience much larger and more difficult to model forces such as air-drag at lower altitudes. The *a posteriori* rms gives a minimum for determining the effective data set weights by reflecting, in a relative sense, these force modeling difficulties. However, when these errors are present, they do not manifest themselves as random data residuals. This nonrandomness (mostly found within a pass of observation residuals) must also be accommodated through a downweighting of the data (Lerch *et al.*, 1988). Furthermore, this requires taking into account the typical number of points in a pass so affected. This reweighting is accomplished in the solution through the optimization of the w_j .

Lerch *et al.*(1988) shows that the w_j can be determined for any given data subset, so long as

the data subset contributes appreciably to the overall solution. The w_j can be optimally obtained through numerical experiments that test subset solutions lacking the specific data set of interest versus the complete solution containing all data. This is an improved method over the iterative and trial and error approach that was used in the optimization of GEM-T1 (Marsh *et al.*, 1987). In Lerch *et al.*(1988), it is further shown that the systematic problems reflected in the tracking data residuals can be effectively accomodated through the downweighting of the data.

A large downweighting of the data has been applied in the present gravitational solutions. Therefore, a review of this necessity is in order to assist in understanding its cause. The weights in Equation (19) , where the preliminary values indicated by σ_{ij}^2 are scaled by w_j , have been found to obey the following general relationship across the 23 different identifiable data subsets in GEM-T1 (See Table 1 in Lerch *et al.*, 1988.)

$$W_j = \frac{w_j}{\sigma_{ij}^2} \sim \frac{1}{(NOBS_j)(RMS_j)^2} \quad (20)$$

where:

- σ_{ij} the same for each i of a given j .
- RMS_j the *a posteriori* rms of the observation residuals for the j -th data subset.
- $NOBS_j$ a value corresponding to a typical number of points in a pass of tracking data in subset j scaled by a factor that changes with differing tracking technologies.
- W_j the absolute weight for the observations of the normal equations for data set j .

The empirical approximation in Equation (20), given more formally in the previously referenced Lerch report, applies more strictly to data types where the precision of the data is small compared to the *a posteriori* rms of fit obtained over a typical orbital arc length using these data. The third generation laser systems are clearly the dominant data type being utilized that displays this characteristic. The extremely precise laser observations have residuals that exhibit biases and slopes within a pass of tracking data. These systematic trends are at a magnitude that exceed the noise-only data precision by a good amount. These data require reweighting to account for the lack of randomness in the residual series. Application of the algorithm shown in Equation (20) reduces the weight of the *NOBS* "correlated" points found within a typical pass of data to that of a single point. For the laser and electronic systems, *NOBS* was anywhere from 30 to 100 points. As indicated in Equation (20), the effective weight given to the individual data points were reduced by a factor of 0.01 to 0.02 in the solution. The optical data were less precise but had far less data within a typical pass, so these data were not downweighted to the same extent.

Similiar downweighting of the data was applied to the altimeter data where the observations themselves are highly precise, but their residuals exhibit strong systematic trends over typical continuous satellite subtracks. The weights selected for the altimeter and surface gravimetry are discussed in Section 2.3.1.

Continuing with the other terms in Equation (18), the values of the expected sizes of individual coefficients are based upon previous investigations (*e.g.*, Kaula, 1966), which show that they follow the general approximate rule

$$\sigma_{lm} = \frac{10^{-5}}{l^2} \quad (21)$$

This expression, known as Kaula's rule, has been modified over the years to more closely reflect the strength of the known long-wavelength terrestrial gravitational field. This correction has been implemented in the solution by setting $\epsilon_1 = 2$. This value reduces the resulting *a priori* spectrum of the terms by $\sqrt{2}$.

The rms coefficient sizes ($\sigma_{\alpha nm}$) for $\bar{\eta}_{A_{\alpha nm}}$ have been obtained from climatological *in situ* data. Levitus (1982) has constructed a global dynamic height model, hereafter denoted $\bar{\eta}_\rho$, from over 70 years of ship data. Temperature and salinity measurements as a function of pressure were used to estimate density through an equation of state and then integrated using Equation (6) from $p_{ref} = 2250$ db to the surface ($p = 0$ db) to solve for the dynamic height variation from a reference state. These estimates of dynamic topography were gridded on a 1° grid. The dynamic heights were converted to η_ρ using the relationship: $\eta_\rho = 10 \int_0^D \frac{1}{\rho} dD$. This is the best information available for modeling $\sigma_{\alpha nm}$, and it is a reasonable first guess suitable for estimating the expected power (in meters) of $\bar{\eta}$.

Engelis (1987) has performed a spherical harmonic analysis of $\bar{\eta}_\rho$. Several solutions were computed in an attempt to harmonically decompose $\bar{\eta}_\rho$. One solution used a simple least squares algorithm considering only those points defined in the $\bar{\eta}_\rho$ grid. This particular attempt was limited to 10×10 in harmonics (Section 5). The overall power in $\bar{\eta}_\rho$ was found to be in excess of 60 cm. This harmonic model closely resembled the analysis strategy and was suitable for estimating the rms coefficient sizes expected from a realistic model of $\bar{\eta}$. A simple linear fit to the Engelis coefficients is given

$$\sigma_{\alpha nm} = -0.01344n + 0.13959 \text{ (meters)} \quad (22)$$

and it is displayed graphically in Figure 2.

This function was used to generate the diagonal terms of the collocation matrix employed to condition the recovery of $\bar{\eta}_{A_{\alpha nm}}$.

In summary, the modified least squares method has the desirable effect of simultaneously minimizing the weighted observation residuals and the overall size of the geopotential and $\bar{\eta}_{A_{\alpha nm}}$. This technique tends to reduce the aliasing effects of higher degree and order information into the low degree and order portion of the model. It helps to prevent highly correlated parameters within the solution from adjusting to unreasonably large values. This technique has previously been shown to provide stability within solutions with large numbers of unknowns having a wide range of parameter recovery sensitivities.

Along with implementing the least squares method, the determination of the scale and weighting factors was a significant task in optimizing the solution. As seen in Equation (19), optimal values for the data weights are required, and the w_j (which establish the overall scale of the covariance error estimates of the solution) need to be obtained through external error calibrations. Marsh *et al.* (1987) detail this process for GEM-T1.

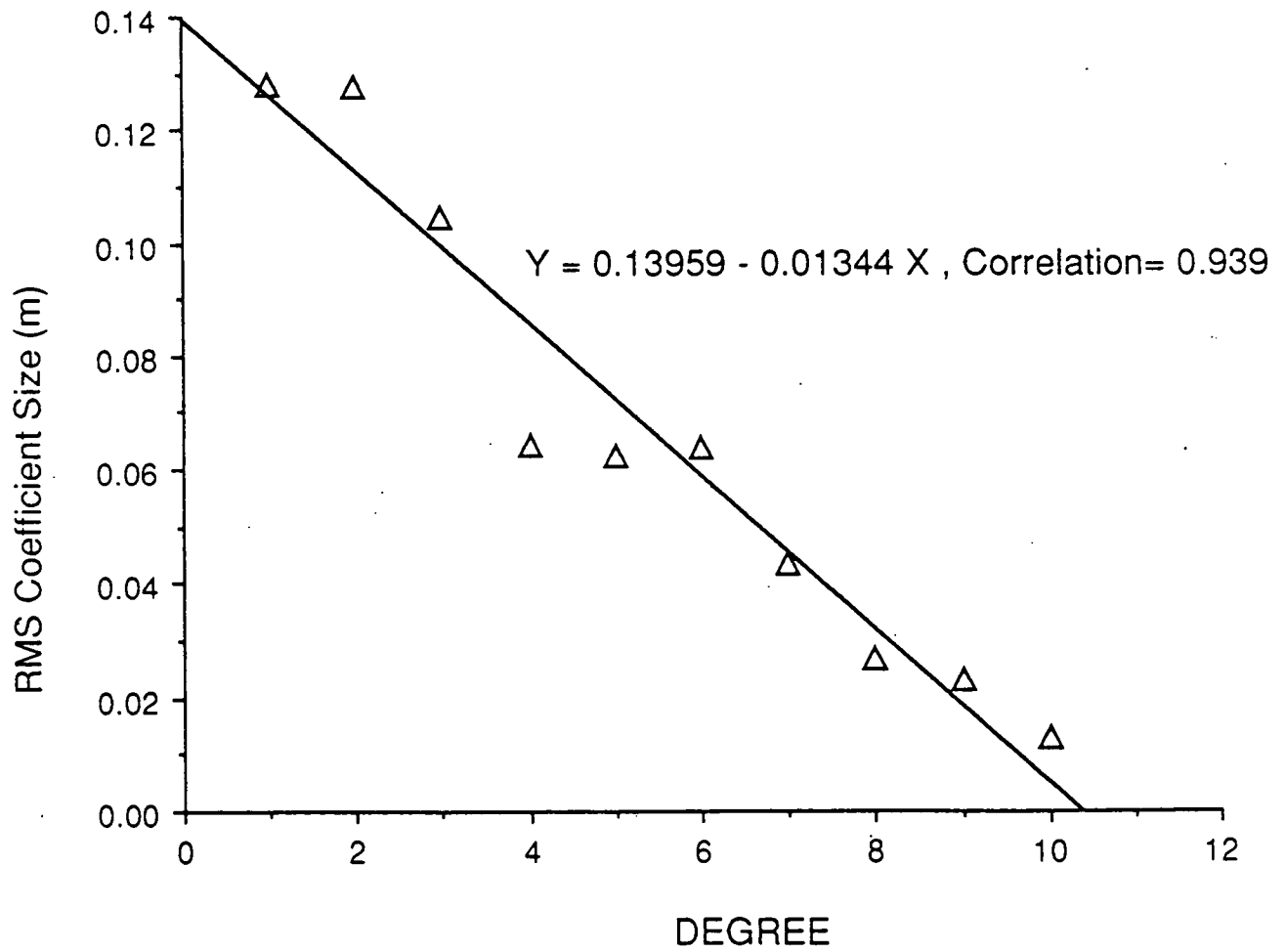


Figure 2. Fit to Engelis (1987) harmonics for $\bar{\eta}_\rho$ to form QSST power law.

2.3.1 Altimeter and Surface Gravity Data Weights

Since the model evolved from the GEM-T1 solution, all data weights and scale parameters used in GEM-T1 were retained for the PGS-3337 solution. Beyond adopting GEM-T1, PGS-3337 did require an experimental procedure to assess the optimal weights (w_j) for the SEASAT altimetry and surface gravimetry observations, as well as for the determination of ε_2 in the $\bar{\eta}_A$ constraint.

The surface gravimetric data were prepared by the Department of Geodetic Science and Surveying at the Ohio State University (OSU) (Pavlis, 1988). These data were in the form of surface gravity normal equations. The individual areal mean gravity anomalies were evaluated at OSU. They were given weights (containing downweighting effects) through regional comparisons with satellite derived gravity and covariance error models. Through testing procedures it was found that no further adjustments were necessary for ascribing weights to the surface gravity normals. Therefore the w_j applied to the surface gravimetry normal equation subset were equal to unity, since downweighting effects have already been applied. The net effect is the preservation of original OSU data weighting assessments that are described in Pavlis (1988).

All of the SEASAT altimeter data were given a uniform nominal data weight $\sigma_{0j} = 1$ m when the data were processed into normal equations. Many experimental gravitational/QSST solutions were produced; these solutions, along with the accuracy estimates, were sensitive to the overall weight given to the altimeter data. The weighting obtained for the altimetry in the PGS-3337 normal equations was

$$w_{jalt} \sim \frac{0.01}{RMS^2} \quad (23)$$

Where, as before, the *RMS* is the *a posteriori* rms value (0.35 m). Again, it was assumed that the altimetry would maintain a constant relative data weight with respect to the surface gravimetry. Altimetry and surface gravimetry were the only data types in PGS-3337 that partially or wholly provided discrete geographical information about the geoid.

$\varepsilon_2 = 1$ was chosen for PGS-3337 because the power law from $\bar{\eta}_\rho$ seemed reasonable. The altimeter data had good sensitivity for all of the adjusted $\bar{\eta}_{A_{annm}}$. Experiments altering ε_2 by a factor of three caused little change of significance in the adjusted $\bar{\eta}_{A_{annm}}$ values. Also of benefit, the σ_n power law effectively controlled the estimated uncertainty for this surface over land areas.

2.3.2 The Solution and Its Statistics

The solution is formed after summing each of the satellite, altimeter and surface gravimetry normal matrices N_j over the entire range of j observation subsets. The geopotential and QSST collocation constraints, scaled by ε_1 and ε_2 , respectively, are combined to form the diagonal signal matrix K^{-1} . The combined normal matrix for the entire solution is then given by

$$C = K^{-1} + \sum_j w_j N_j \quad (24)$$

The K^{-1} matrix has certain important properties. First, it is independent of any underlying field values and does not favor any specific gravity or $\bar{\eta}$ model, as the total power of the models

3 The Altimeter Observations

Many factors enter into the altimeter range measurement (h_{alt}) that can be sources of error in determining the long wavelength shape of the ocean surface. Included in these are a number of instrument corrections (Δh_{alt}) that must be applied (Chelton, 1988). Furthermore, the sea surface mapped by a satellite altimeter is complicated for it is an instantaneous measure of a surface in motion. The sea height changes over a wide range of wavenumbers and frequencies, and many signals of different physical origins combine to form the surface elevation at a given point. To extract $\bar{\eta}$ and the gravitational signal from altimetry, careful preprocessing and selection of the data are necessary to reduce aliasing in the recovery. The data selection, masking and preprocessing algorithms that were developed for PGS-3337 are discussed within this section.

3.1 SEASAT Data Selection Criteria

All of the available SEASAT altimeter data set (from July 27 to October 10, 1978) has been used in this investigation. The data utilized in the PGS-3337 solution were screened by a series of algorithms that were designed to eliminate data of limited usefulness. The major problem areas are:

- The elimination of data containing large short-wavelength signatures in h_N that would not be accommodated by the 50×50 harmonic limits of PGS-3337.
- The elimination of data taken in shallow seas, overland, or in regions where ocean tidal models are not well known.
- The elimination of data where tropospheric refraction errors might be large.
- To optimally select a one point per five second sample of the remaining one second data to reduce noise in the altimetric sample.

3.1.1 Overland Flagging

The SEASAT Geophysical Data Record (GDR) format contained a flag indicating whether the data were acquired over land or over water (Anonymous, 1980). All data accepted were flagged with an over water value.

3.1.2 AGC Acceptance Criteria

The problem of data taken over ice in the open sea had to be addressed using the Automatic Gain Control (AGC) value provided on the GDR. Ice, as opposed to the broad ocean surface, causes a return waveform that is sharply specular and one that has an AGC value greater than that normally obtained from the ocean surface. Therefore, to screen out sea ice returns, all observations where the AGC value exceeded 37 db were eliminated.

and not its adjustment from *a priori*, is minimized. It is however, biased towards zero for each individual coefficient. Applying K^{-1} is mathematically equivalent to introducing a set of additional observations into the system assigning zero to each of the $\bar{\eta}_A$ and gravitational parameter values (above some degree cutoff for the gravity constraint) with an uncertainty obtained from their expected degree variances. It is a mild type of constraint that has been well tested in earlier GEM evaluations.

The scaled error covariance for the solution is obtained as

$$\sigma_{parameters} = C^{-1} = (K^{-1} + \sum_j w_j N_j)^{-1} \quad (25)$$

The overall weighting found appropriate for GEM-T1, has been retained in PGS-3337. Calibration of our new model with GEM-T1 was found to yield reliable error assessments. These calibration results are found in Lerch, *et al.*(1988).

3.1.3 High Degree Geoidal Mask

The SEASAT altimeter was found to be capable of mapping the ocean surface down to wavelengths of 35 km or less (Brammer and Sailor, 1980). A 50×50 gravitational field is not capable of modeling h_N at wavelengths smaller than 300 km. Clearly, this mismatch between bandwidths of data content and gravitational modeling capabilities is one of the most difficult problems encountered when using direct altimetry in gravitational solutions. The altimeter data were used in complete normal matrices, that contained 3400 correlated parameters for PGS-3337.

Rapp and Cruz (1986) used a form of harmonic analysis that assumed no correlation between high-degree and order coefficients. This analysis produced a high degree gravity model from a combination of altimetry and surface gravity measurements that is complete to degree and order 360. This gravitational model should work especially well for correcting the SEASAT data since these data were evaluated when forming the model itself. This model was used and its geoidal undulation was calculated for a $\frac{1}{2}^\circ$ grid for all terms summed between ($51 \leq l \leq 300$). If $|h_{\Delta N}| \geq 2.5$ m in Equation (9) the observation was eliminated. This cutoff was established experimentally, but it is approximately in conformance with the global power law for geoid amplitudes as derived by Kaula (1966).

Since high-degree geoid aliasing is a problem of great significance, an additional mask was imposed on the data associated with these short wavelength gravitational effects. The Marsh *et al.* (1982) mean sea surface with $\frac{1}{8}^\circ$ resolution was used to calculate surface gradients by

$$|\nabla h_N| = \left(\left(\frac{\partial h_N}{\partial x} \right)^2 + \left(\frac{\partial h_N}{\partial y} \right)^2 \right)^{\frac{1}{2}} \quad (26)$$

Estimates of the sea surface gradients were calculated for a $\frac{1}{4}^\circ$ grid. Again, linear interpolation was used to obtain the estimated gradient at the subsatellite location. If $|\nabla h_N| \geq 5$ m/deg, the observation was deleted. Note, this second algorithm alone will not locate all sharp short wavelength features. As an example, the slope of h_N at the bottom of some of the deepest sea trenches is relatively flat. Yet, when combined with the previous test ocean areas with sizeable short wavelength geoidal signals were located and eliminated from the analysis.

3.1.4 Elimination of Data from Shallow Seas and from Continental Shelves

The climatological dynamic height model ($\bar{\eta}_\rho$) was geographically restricted to exclude data from regions of shallow seas and continental shelves. $\bar{\eta}_\rho$ was taken from a 1° grid (Levitus, 1982) and used for masking purposes. If altimetry measurements were made over an area that was not defined by $\bar{\eta}_\rho$, these observations were deleted from the present data set. See Figure 3 for a map of $\bar{\eta}_\rho$ indicating the resulting mask as shaded areas.

3.1.5 Elimination of Regions of Poorer Ocean Tidal Modeling

The GDR (Anonymous, 1980) provided two values for η_T , one from the series of models produced by Schwiderski (1981, 1982, 1983) and another from models developed by Parke (1982). The

DYNAMIC OCEAN TOPOGRAPHY RELATIVE TO A 2000 D-BAR REFERENCE SURFACE (LEVITUS, 1982)

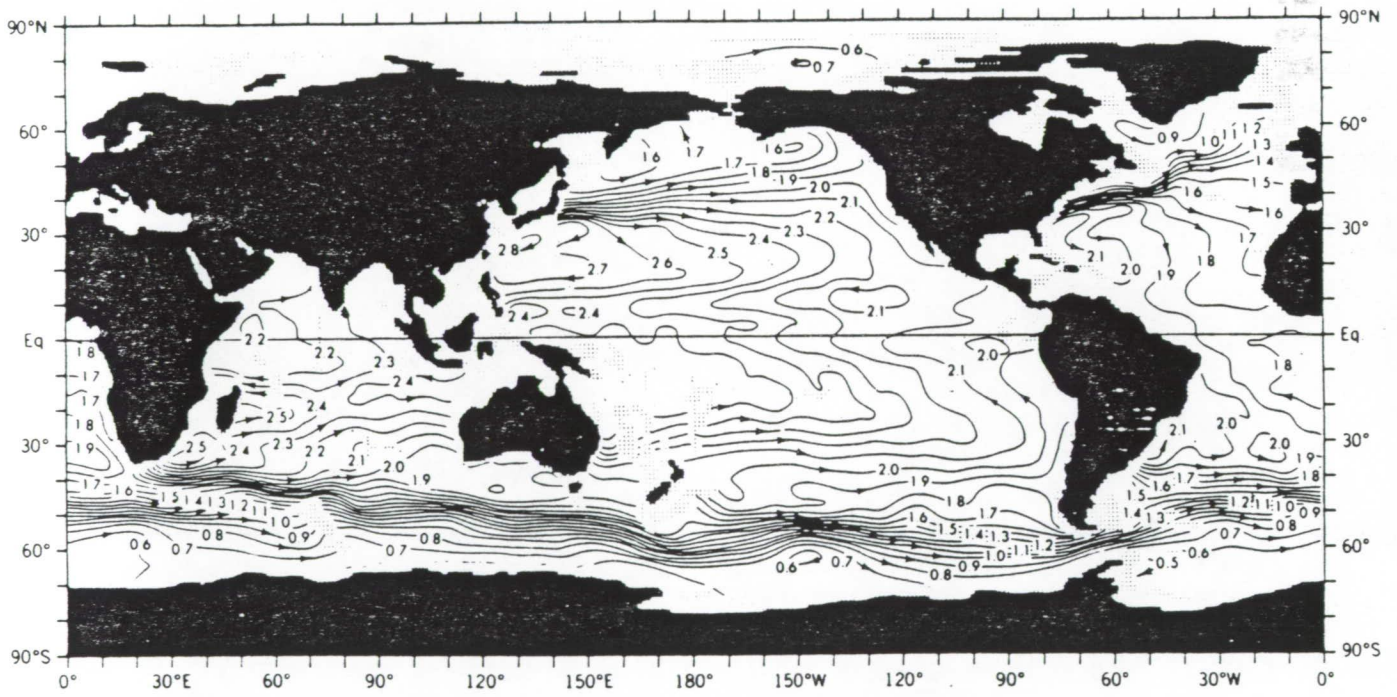


Figure 3. Dynamic ocean topography relative to a 2250 db reference surface - $\bar{\eta}_\rho$ (Levitus, 1982).

ORIGINAL PAGE
BLACK AND WHITE PHOTOGRAPH

Schwiderski correction was adopted in the analysis. However, if η_T given by Schwiderski differed by more than 1.5 m from that of Parke, the altimeter observation was eliminated from the analysis.

3.1.6 Wet Troposphere Range Correction

SEASAT flew a Scanning Multichannel Microwave Radiometer (SMMR) that gave a nadir looking estimate of water vapor content within the atmospheric column. This estimate is essential for proper computation of the wet tropospheric refraction term (Tapley *et al.*, 1982). Observations that lacked the corresponding SMMR estimate of water vapor were deleted from the analysis. The dry tropospheric refraction corrections, which rely on estimates of surface pressure and temperature (Tapley *et al.*, 1982), used values provided from hindcasts by the Fleet Numerical Weather Center.

3.1.7 Altimeter Data Noise

All of the observations that passed the tests in Sections 3.1.1 - 3.1.6 were at a greater data rate (one per second) than was practical for evaluation. These data were divided into 30 second bins that overlapped by 15 seconds. The values of h available on the GDR were evaluated by simple regression analysis using a quadratic polynomial. Stray points were edited if they departed by more than three standard deviations from this function. The analysis was repeated until editing ceased. If the total rms of fit for the 30 sec bin exceeded one meter, all of the data in the bin were eliminated. For the remaining observations, the residuals between h and the function were used to thin out the data. The altimeter measurement having the smallest residual in each of the first three 5 second bins was the point retained for orbital processing. The analysis was shifted ahead in time by 15 seconds and the regression analysis was repeated.

3.1.8 Data Selection Summary

The data selection algorithms produced a SEASAT altimeter data set of 313,000 observations. The $\bar{\eta}_p$ mask eliminated 16% of the data. Nine percent of the data were eliminated by the high-degree geoid sensitivity tests. All of the other tests caused another 6% of the data to be edited. Of the observations that remained, the 5:1 thinning produced the final data set. For the present, computation of normal equations for a full 50×50 gravity model from 313,000 observations is excessive. So even this "final" data set was further sampled to include every third point. This uniform selection produced the final 104,100 SEASAT altimeter observations used in PGS-3337 with 1-point-per-15-seconds sampling along the satellite ground track (~ 90 km).

3.2 SEASAT Data Correction Procedures

This section will describe the altimeter data corrections that were used in addition to the standard corrections available on the GDR and those already made to the data when producing the GDR. The standard GDR corrections (Anonymous, 1980) include:

- Tropospheric refraction
- Ionospheric refraction
- Instrument corrections accounting for tracker location and off-nadir attitude misalignments
- Satellite clock corrections
- Earth tides (h_T) updated to MERIT standards
- Ocean tides (η_T) from Schwiderski's model
- Atmospheric loading (η_a)

Three additional corrections were made to the information contained on the GDR. These corrections are described in the following paragraphs.

3.2.1 Correction for Sea-State Bias

The troughs of ocean surface waves reflect more electromagnetic radiation to a satellite altimeter than do the crests (*e.g.*, Walsh *et al.*, 1988). This causes an apparent lengthening of the altimeter range that increases with higher significant wave heights. Using a correction constant obtained by Douglas and Agreen (1983), the correction for the SEASAT altimeter range (usually referred to as either the sea-state or electromagnetic (EM) bias) is given by

$$h_{alt} = h'_{alt} - \Delta h_W \quad (27)$$

where $\Delta h_W = 0.07 * W_{\frac{1}{3}}$ and $W_{\frac{1}{3}}$ is a measure of significant wave height in meters. The analysis performed by Douglas and Agreen (1983) found a linear correction term performed satisfactorily over the range of sea states seen during the limited lifetime of the SEASAT Mission. It was noted that these effects may be slightly nonlinear over the largest ranges of $W_{\frac{1}{3}}$. The uncertainty assessed by them for this correction term is 20% of its value. In addition, Witter and Chelton (1988) have found time dependencies in the linear form of the correction. Plate 1a shows the mean value for the sea-state mapped over the limited SEASAT lifetime.

3.2.2 Correction for High Degree Geoid Contributions

As described in Section 3.1.3, a $\frac{1}{2}^\circ$ grid of the high degree geoid ($51 \leq l \leq 300$) was computed from a gravity model developed by Rapp and Cruz (1986) for the purpose of masking SEASAT data where $|h_{\Delta N}| \geq 2.5$ m. For data that passed all of the masking tests, this same set of gridded values was interpolated to the sub-satellite location and the resulting value added to the altimeter range to compensate for the truncations of the geopotential at degree 50.

3.2.3 Recalculation of the Observation Uncertainty

As previously described, all of the altimeter data used in PGS-3337 were given a uniform *a priori* weight of 1 m. However, for testing purposes, the range uncertainty was recalculated for each observation based upon the three major remaining unmodeled signals sensed by the data that are presently a source of aliasing within the analysis. The algorithm used was

$$\sigma_A = ((h_\epsilon)^2 + \langle \eta \rangle^2 + \langle \eta_T \rangle^2 + (\Delta h_W)^2)^{\frac{1}{2}} \quad (28)$$

where:

- $\langle h_\epsilon \rangle$ = 0.2 is an (pessimistic) assessment of measurement noise. It is also used here to reflect uncertainties in the higher order geoid corrections.
- $\langle \eta \rangle$ the rms estimate of sea surface variability at the observation location obtained from a model developed by Cheney *et al.*(1983).
- $\langle \eta_T \rangle$ the difference between the Parke and Schwiderski ocean tidal correction.
- $\langle \Delta h_W \rangle$ 20% of the sea-state correction applied to the observation, reflecting the uncertainty in the estimate of the linear relationship between the sea-state bias and significant wave height.

This new uncertainty estimate has been used for diagnostic purposes in the evaluation of the aliasing in the resulting geopotential model. It is statistically useful when performing post-model assessments of h_{sat} errors that employ crossover techniques, where these errors remain behind in the crossover altimeter residuals. This analysis will be discussed when the orbital performance of PGS-3337 on SEASAT is presented in Section 6.

3.3 Altimeter Bias Assessment

A consistency check was performed on the altimeter treatment through a separate solution of h_B within each of the 6-day arcs used to generate normal equations. However, the bias must also accommodate any implied bias of the measurements introduced through the assumption that $a_e = 6378137$ m for the semi-major axis of the Earth's ellipsoid. Recent results by Rapp (1987) obtained from an analysis of Doppler station orthometric heights concludes that this value of a_e is 75 cm too large. Given the bias convention (Residual = Observed - Calculated - Bias), Rapp's result would imply $h_B = 75$ cm.

Table 2 presents the rms of fit to the altimeter data (and the number of observations) when: (a) using GEM-T1 for the orbit computations; (b) the GEM-T1 geoid; and (c) the *a priori* estimate of $\bar{\eta}_p$ complete to 10×10 in harmonics (Engelis, 1987). These models represent the best information that was available when initiating the processing of the SEASAT altimeter data. The biases that are shown were obtained individually from the 6-day arc solutions used to create the normal equations. With a couple of exceptions, the individual bias values were quite stable from arc to arc.

Table 3 presents the biases recovered when testing the PGS-3337 model, where very stable biases were obtained. The overall average for the GEM-T1 solution was $h_B = 77$ cm. The overall average for the PGS-3337 solution was $h_B = 76$ cm. The SEASAT Project applied an 11 cm bias

Table 2: Rms Fit of SEASAT Altimeter Data Using: GEM-T1 for h_{sat} and h_{Nref} with $\bar{\eta}_p$

Epoch 1978	Number of Observations	Rms (meters)	h_B (cm)
July 27	10850	1.57	60
Aug. 2	11142	1.46	62
8	11306	1.51	57
15	4449	1.48	108
18	8920	1.51	80
23	5184	1.54	91
26	2732	1.56	46
Sept. 1	24	1.27	94
5	1603	1.58	119
10	4179	1.59	63
17	11401	1.47	62
23	11682	1.50	68
29	11496	1.51	85
Oct. 5	9168	1.50	
Average			77

to the data we used. This correction was found to be unnecessary; however, this bias was not removed in the processing. The bias values recovered in this analysis are in excellent agreement with the previously quoted results of Rapp for a 75 cm adjustment to the $a_e = 6378137$ m indicating 6378136.25 m is a better value. The value we obtained from SEASAT after the 11 cm correction is removed is $a_e = 6378136.14$ m. An independent calibration of the SEASAT altimeter using laser tracking as the satellite overflew Bermuda estimated that $h_B = 0 \pm 7$ cm (Kolenkiewicz and Martin, 1982).

This high level of bias stability indicated by the PGS-3337 SEASAT arcs is essential for TOPEX. With a repeating ground track, 10 cm accuracy in h_{sat} and averaging periods of 10 days or more, it is reasonable to predict that such tests on the TOPEX h_B stability would have a precision of a centimeter or better, that is needed for monitoring long term changes in global sea level.

3.4 Altimeter Correction Errors

3.4.1 Atmospheric Refraction

The estimation of the atmospheric refraction delay of the radar pulse requires knowledge of the atmospheric surface pressure (SLP) and water vapor content at each altimeter observation point (Chelton, 1988). SEASAT flew a SMMR that provided a nadir looking estimate of the water vapor content of the atmosphere. With this information the wet troposphere range correction can be modeled to an accuracy on the order of 5 cm (Tapley *et al.*, 1982). However, the dry troposphere range correction requires knowledge of SLP. SLP is not measured uniformly over the broad expanse

Table 3: Rms Fit of SEASAT Altimeter Data Using: PGS-3337 for h_{sat} and $h_{N_{ref}}$ with $\bar{\eta}_A$

Epoch 1978	Number of Observations		Rms		h_B (cm)
	Altimeter	Doppler	Altimeter (cm)	Doppler (cm · s ⁻¹)	
Jul 27	10690	8049	36	0.81	74
Aug 2	10985	7361	34	0.77	76
8	4569	10153	35	0.82	73
15	4369	3545	33	0.77	80
18	8762	4353	35	0.76	75
23	5070	3714	31	0.80	80
26	2667	7848	31	0.84	74
Sep 1	24	5663	20	0.85	75
5	1569	6390	33	0.93	72
10	4157	7427	31	0.81	76
17	11210	5377	31	0.77	73
23	11461	5317	31	0.76	72
29	11338	4764	34	0.77	76
Oct 5	9018	4784	33	0.76	82
Average			32	0.80	76

of the ocean (Chelton, 1988). The local pressure field is often subject to prediction errors that have a geographically non-uniform distribution that can cause errors in the refraction correction that exceed 5 cm (VanDam and Wahr, 1988). The characterization of this refraction error is difficult to make in terms of wavenumber, variability, and location without better knowledge of the pressure field itself.

3.4.2 Ionospheric Refraction

Ionospheric refraction effects at altimeter radio frequencies are also significant (Chelton, 1988). TOPEX will fly a dual frequency altimeter that will permit a direct correction for the first-order ionospheric refraction effects. SEASAT operated at a single frequency. Therefore, the ionospheric refraction corrections that have been applied to the SEASAT data are unrealistically smooth for they were computed from mean monthly ionospheric electron density models that lack much of the high-frequency structure and turbulence observed in the local ionosphere (Lorell *et al.*, 1982). These errors appear to be at large scales and somewhat hemispheric because larger errors are seen during daylight.

3.4.3 Geoid

The complexity of the gravitational field/geoid sensed by the altimeter is also a cause for concern in the model. The altimeter observes h_N with amplitudes as small as a few cm over spatial scales

approaching 10 to 20 km. The best GSFC global geoids are limited to a spatial resolution of about 3° . The accuracy of such models is a function of the wavelength, with the overall commission error for the PGS-3337 (50,50) model being about 60 cm, and the (10,10) portion of the model having an accuracy of about 10 cm (this is discussed further in Section 4.4). Models of h_N commensurate with the spatial resolution of the altimeter system are not available because of the lack of observational data.

4 Improved Gravity Field Model: PGS 3337

PGS-3337 is a gravitational model that has combined the satellite tracking data used in the GEM-T1 gravity model with SEASAT altimeter and surface gravimetric observations. It is complete to degree and order 50 in spherical harmonics. This model was developed to investigate the incorporation of altimetry data as tracking observations in gravitational solutions. To investigate the problem of separating gravitational and oceanographic signals, it was necessary to assess the recoverability and separability of $\bar{\eta}$, gravity, dynamic tidal and orbital parameters within a simultaneous least squares solution. This section will review the major elements of this solution and describe the improvement in model definition obtained from this optimal combination of available gravitational information as it pertains to the definition of $h_{N_{r,e},j}$. The spherical harmonic coefficients for the PGS-3337 gravitational potential are given in Appendix A.

4.1 GEM-T1 Overview

The GEM-T1 solution was developed using significantly more precise tracking data than in previous Goddard Earth Models. GEM-T1 is a general gravitational model (*i.e.*, not tailored for any specific orbit) that uses modern geodetic constants (the most recent International Astronomical Union (IAU)/J2000 Reference System). This model is described more fully in Marsh *et al.* (1987, 1988). Lerch *et al.* (1988) discuss the calibration of its error estimates.

The GEM-T1 solution used precise third generation laser tracking data taken on seven different geodetic satellites. Laser ranging to the LAGEOS and Starlette satellites were of particular importance to the field's definition. TRANET Doppler tracking data sets from SEASAT and OSCAR 14 were also used. Other less precise optical tracking observations were included to provide a more uniform distribution in the sampling of the orbital inclinations and helped to separate the individual spherical harmonic coefficients comprising the model. Table 4 summarizes the tracking data from the 17 satellites used in GEM-T1.

Critical analysis of GEM-T1 shows that above degree 15, few of the spherical harmonics, mostly associated with satellite resonances, are well determined. While there is significant sensitivity to the satellite perturbations arising out of higher degree terms, the stability of least squares estimation decreases rapidly with increasing degree, because of signal attenuation and incomplete global coverage. A high degree model is obtained despite the limitations in tracking data and satellite orbital distributions because of the least squares constraint technique.

Below degree 15, and especially below degree 10, the GEM-T1 model is well determined, and is nearly a factor of two improved over any earlier GEM model, even those containing altimetry. This is shown in Figure 4, that presents a comparison of the calibrated rms of coefficient errors by degree of GEM-T1 with its satellite-only predecessor, GEM-L2.

The near-global coverage at shorter wavelengths provided by satellite altimetry and surface gravimetry greatly improves the recovery of the higher degree terms. This is shown in Figure 5 where the satellite-only GEM-T1 error estimates are compared with those of a field determined from altimetric and gravimetric data alone. It is important to note that the satellite only models are, in

Table 4: Data Utilized in the GEM-T1 gravity model

Satellite	Data Type	Normal Matrices	Observations	
LAGEOS	Laser	58	144,527	
Starlette		46	57,356	
GEOS-1		48	71,287	
GEOS-2		28	26,613	
GEOS-3		36	42,407	
BE-C		39	64,240	
SEASAT		14	14,923	
DI-C		4	7,455	
DI-D		6	11,487	
PEOLE		6	4,113	
Sub-Total			285	444,408
SEASAT	Doppler	15	138,042	
OSCAR-14		13	63,098	
Sub-Total		28	201,140	
GEOS-1	Camera	43	60,750	
GEOS-2		46	61,403	
Anna		30	4,463	
Telstar		30	3,962	
BE-C		50	7,501	
BE-B		20	1,739	
Courier 1B		10	2,476	
Vanguard-2RB		10	686	
Vanguard-2		10	1,299	
DI-C		10	2,712	
DI-D		9	6,111	
PEOLE		6	38	
Sub-Total			273	153,140
Total			*580	798,688

*PEOLE arcs contained both laser and optical data.

RMS of Coefficient Error per Degree

Error $\times 10^{-9}$

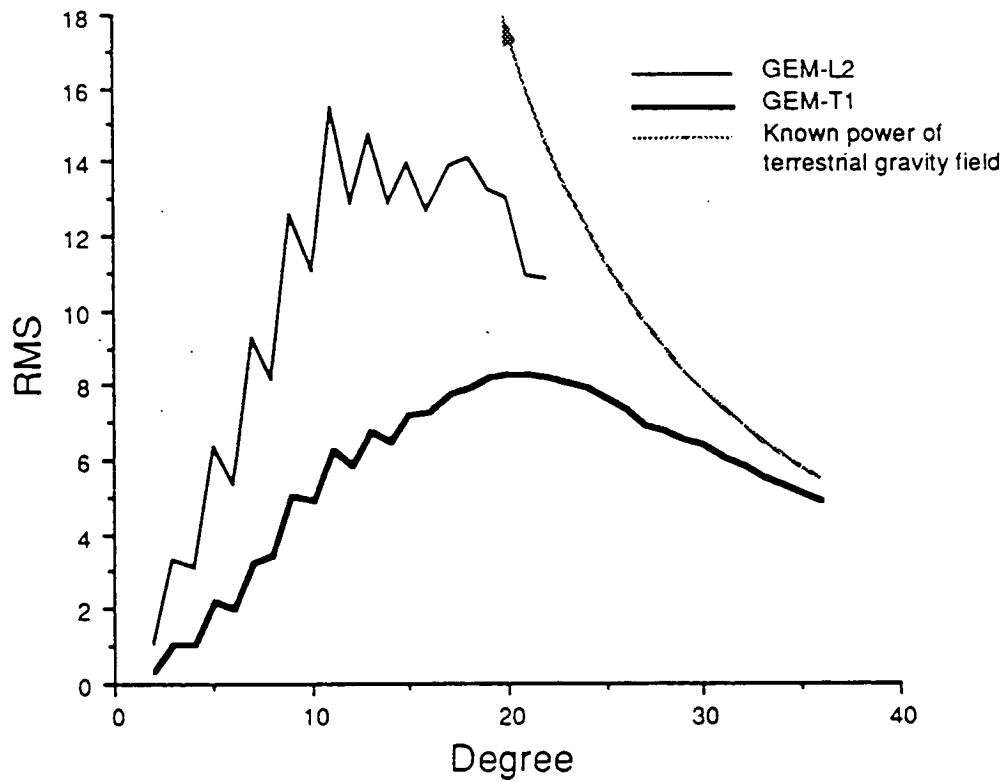


Figure 4. A comparison of GEM-T1 and GEM-L2 calibrated rms coefficient errors by degree.

general, significantly cross-correlated only within the geopotential orders. The largest correlations are found for terms of a given order with common odd/even degree parity. By improving the deconvolution of the higher degree terms, the inclusion of altimetric/gravimetric data also has a favorable impact on the lower degree and order satellite field. Separability of the individual harmonic terms extends into the long wavelength portions of the entire combined model. Figure 6 shows the reduced calibrated rms coefficient errors by degree for PGS-3337 compared with those of GEM-T1.

4.2 SEASAT Altimetry

In order to use altimetry observations without aliasing the gravity field and orbit computations with the oceanographic signal, $\bar{\eta}$ must be represented. $\bar{\eta}_p$ is the best nonaltimetric global model for $\bar{\eta}$ at long wavelengths. This climatological model cannot be expected to describe precisely the dynamic topography during the SEASAT timeframe. In our solution, $\bar{\eta}_p$ was used as *a priori* information in the orbital analyses. A spherical harmonic representation was selected for $\bar{\eta}_A$ and the coefficients of both gravity and $\bar{\eta}_A$ expansions were simultaneously recovered within the PGS-3337 model. This solution, which combined SEASAT altimetry with data sets very sensitive to long wavelength gravity signals like laser tracking observations, contains the elements by which $\bar{\eta}_A$ can be separated from that of the gravity field. In the absence of a dedicated geopotential research satellite mission, altimeter data and surface gravimetry remain the major sources of information for gravitational models that seek to represent the field accurately with a resolution beyond degree 30.

The effects of other nongeoidal signals contained in altimeter data (e.g. mesoscale structure and unmodeled tides) were ameliorated by significantly downweighting the altimetry observations when they were combined with GEM-T1. As shown in Equation (23), the altimeter data weight was reduced to approximately 3.1 m in σ . This can be contrasted with the σ given to a LAGEOS range normal point observation. For the definition of the low degree and order portion of the gravitational model where LAGEOS is most sensitive, LAGEOS information dominated. Each LAGEOS laser normal point has eight times more weight than a corresponding altimeter range in the PGS-3337 solution. This produces a long wavelength gravity model that strongly depends on the unambiguous signal sensed in perturbed orbital motion of satellites like LAGEOS.

The GEM-T1 solution is complete in spherical harmonics to degree and order 36. The laser and Doppler tracking observations in this model included evaluation of terms for many orders out to degree and order 50. When the gravity model was extended to degree and order 50, the tracking data normals made dynamic contributions to these additional terms. In the solution for 66 dynamic ocean tidal parameters, the altimeter data were restricted in their contribution to this recovery and they were only allowed to contribute as tracking measurements.

The η_T were modeled using the Schwiderski models in the initial orbit computations. The tidal adjustment was a "free" adjustment and thus the Schwiderski models played no direct part in the dynamic tidal recovery. To the contrary, the dynamic tides represent the tidally varying gravitational attraction sensed by near-Earth satellite perturbations.

Earth and ocean tides cannot be separated through the exclusive study of orbital motion, and

RMS OF COEFFICIENT ERROR PER DEGREE

ERROR X 10⁹

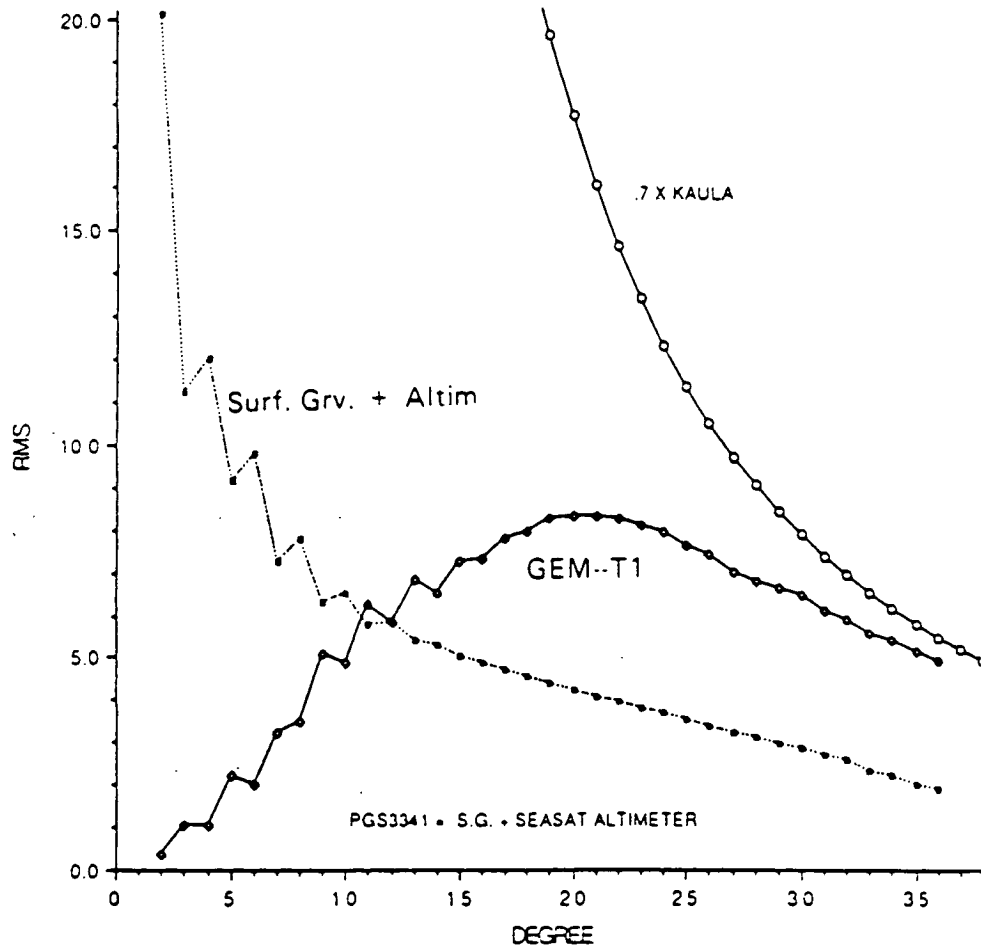


Figure 5. A comparison of GEM-T1 and PGS-3337 error estimates.

RMS OF COEFFICIENT ERRORS PER DEGREE

ERROR X 10⁹

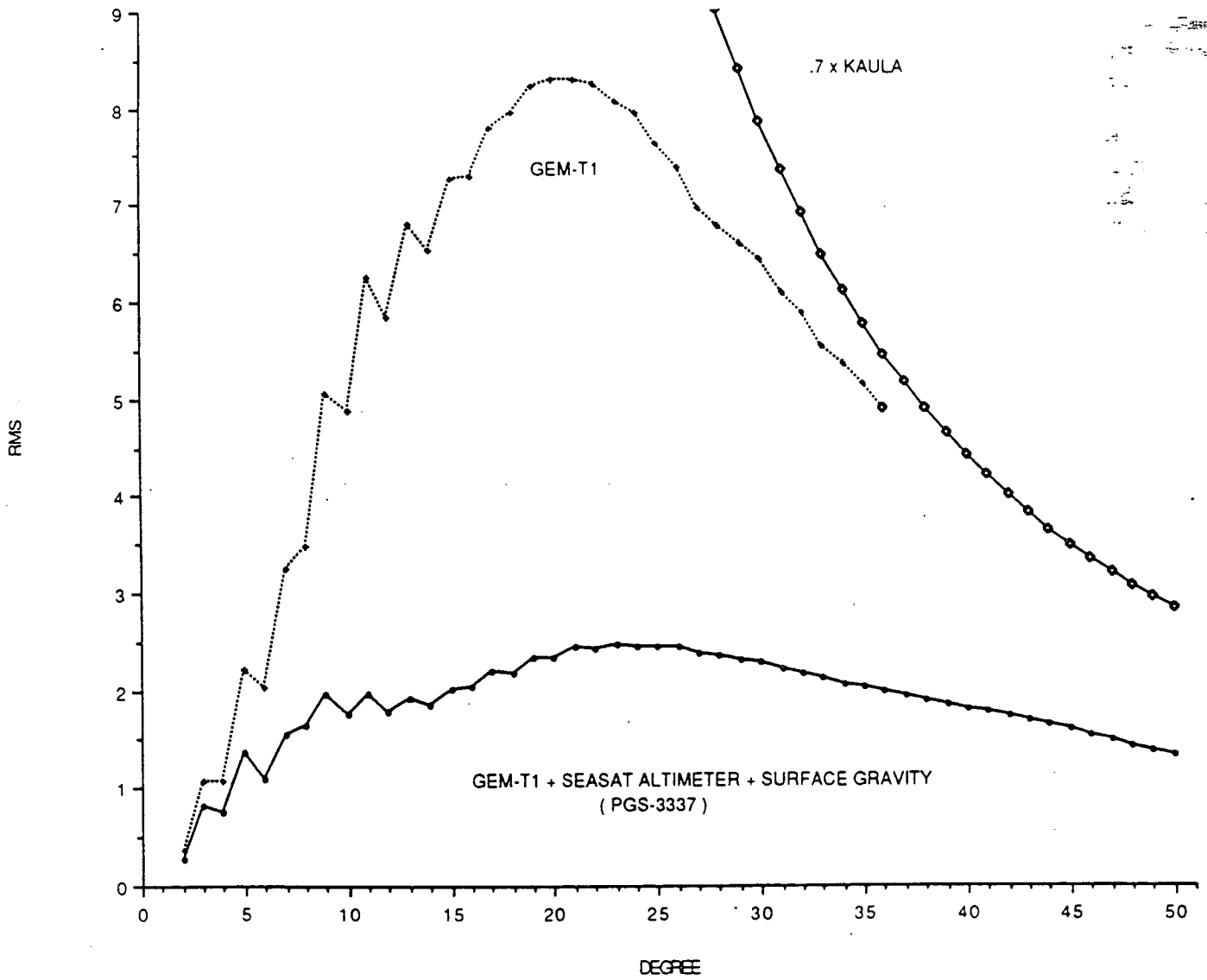


Figure 6. A comparison of PGS-3337 and GEM-T1 calibrated rms coefficient errors by degree.

the choice of making an adjustment in the space of ocean tidal harmonics rather than solid Earth Love numbers is one of convenience, and not necessity. The tidal solution therefore, is still strictly based on the observed evolution of satellite trajectories although altimetry is utilized. The tidal solution for PGS-3337 is quite similar to that published for GEM-T1 (Christodoulidis *et al.*, 1988; see Appendix B). Some changes occurred for third degree tidal terms that is expected since these terms have stronger sensitivity to the radial evolution of a satellite's orbit (*i.e.*, they have larger eccentricity perturbations). The even degree tides were largely unaffected by altimeter/surface gravity contributions.

The SEASAT altimeter data set has been previously described in Table 2. A map of the SEASAT observations utilized in PGS-3337 is given in Figures 7a,b. The data sampling strategy described in Section 3.1 of the entire mission was utilized. A post-solution re-analysis of these data is given in later sections of this report.

4.3 Surface Gravimetry

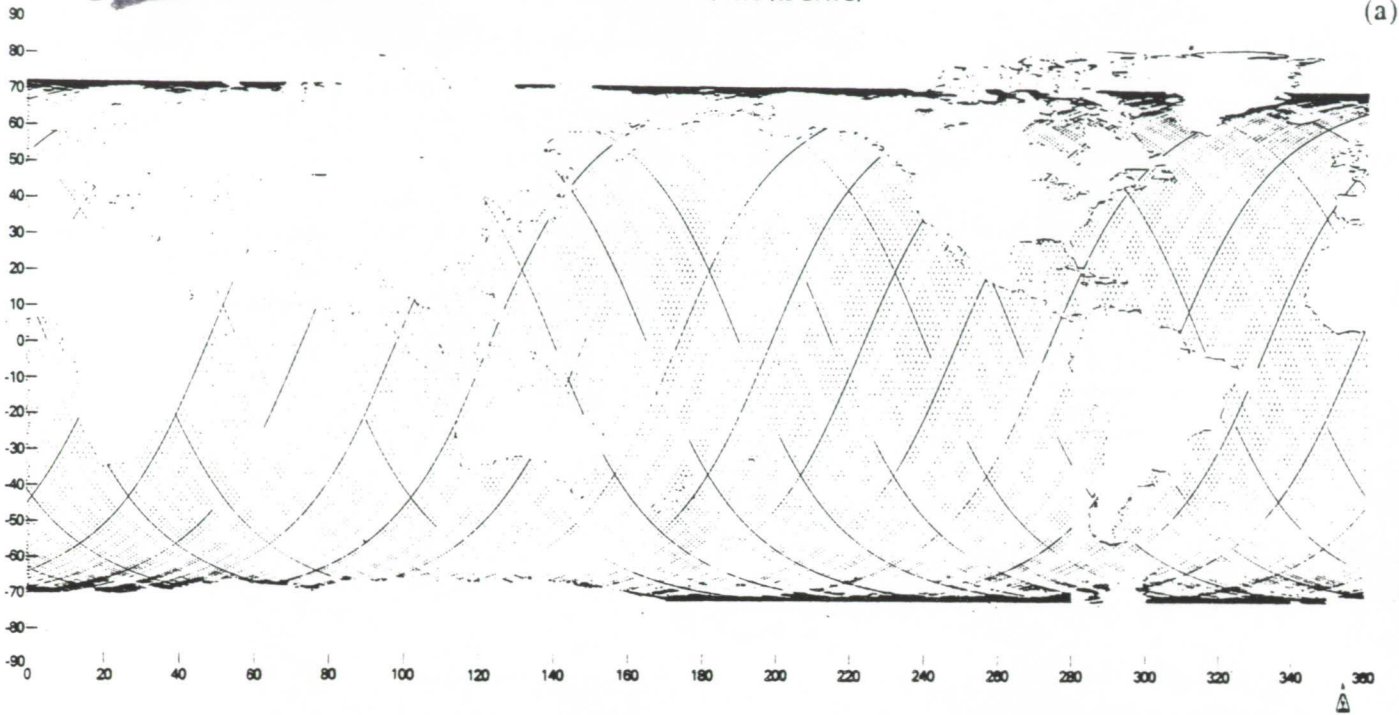
Pavlis (1988) gives a thorough description of the preparation, correction, validation, and verification efforts undertaken on the surface gravimetry utilized in PGS-3337. In total, 48,955 $1^\circ \times 1^\circ$ equi-angular mean anomalies were utilized. Their geographic location is shown in Figure 8a. Unfortunately, surface gravimetry comes from many sources, is poorly documented, and is of variable quality and accuracy. Variations among local datums and survey networks is a common problem complicating the optimal utilization of this source of information. We are fortunate that the Department of Geodetic Science at Ohio State University (OSU) has provided an extensive analysis. This analysis has permitted us to effectively utilize these observations in the form of normal equations provided by this group. When forming the surface gravity normal equations for our use, OSU corrected the observations for the gravity model contribution above degree 50. This parallels the processing we have performed on the satellite altimetry.

Terrestrial gravity information is included to gain important detail of the short wavelength gravity features that the satellite data cannot provide at the same accuracy or resolution. This is especially important over the continents in order to achieve comparable coverage with that provided over the oceans. These anomalies cover 61% of the land areas. However, the accuracy over many regions is quite poor. For example, only 11% of the the Earth's total area is covered by anomalies with an accuracy of 5 mgals or better for 1° averages. The land areas for which the coverage is weakest includes parts of South America, Greenland, Africa, Eastern Europe, Asia and the polar regions. In many of these places data exists but has not been released. Therefore, 5684 blocks contain gravity values that rely solely on geophysical prediction algorithms. These geophysically predicted anomalies are shown in Figure 8b. The predicted anomalies have been given large uncertainties (> 20 mgals) when forming the surface gravity normal equations used in PGS-3337.

~~ORIGINAL PAGE~~

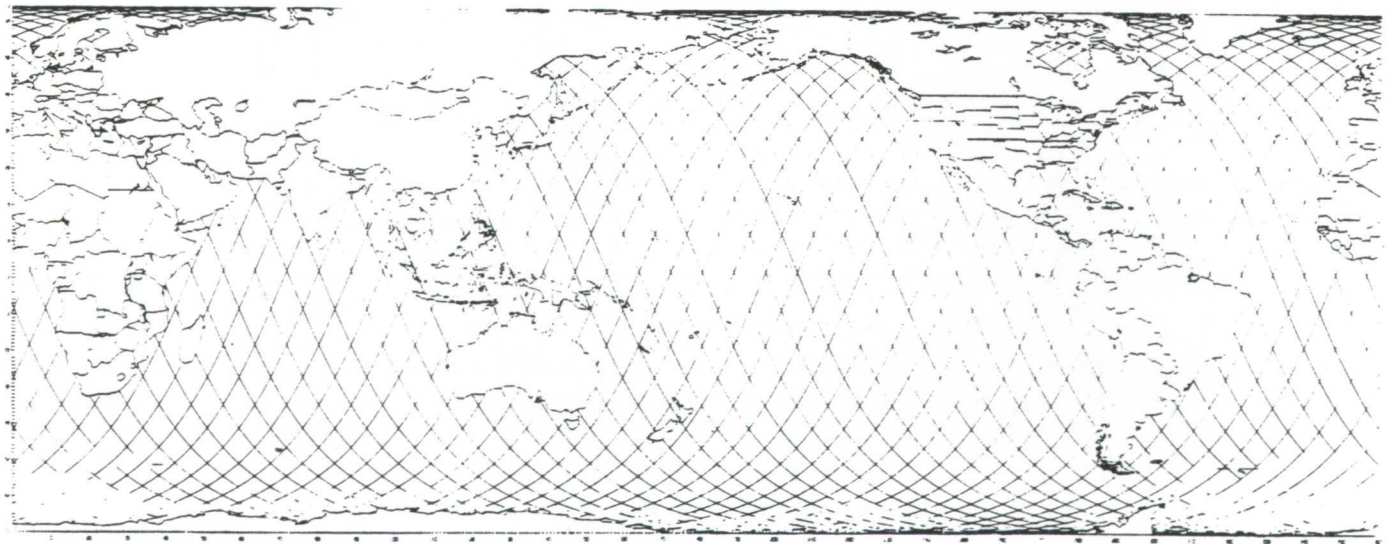
SEASAT ALTIMETER DATA
JULY 28-AUG. 15, 1978 (18 DAYS)

ORIGINAL PAGE IS
OF POOR QUALITY



(a)

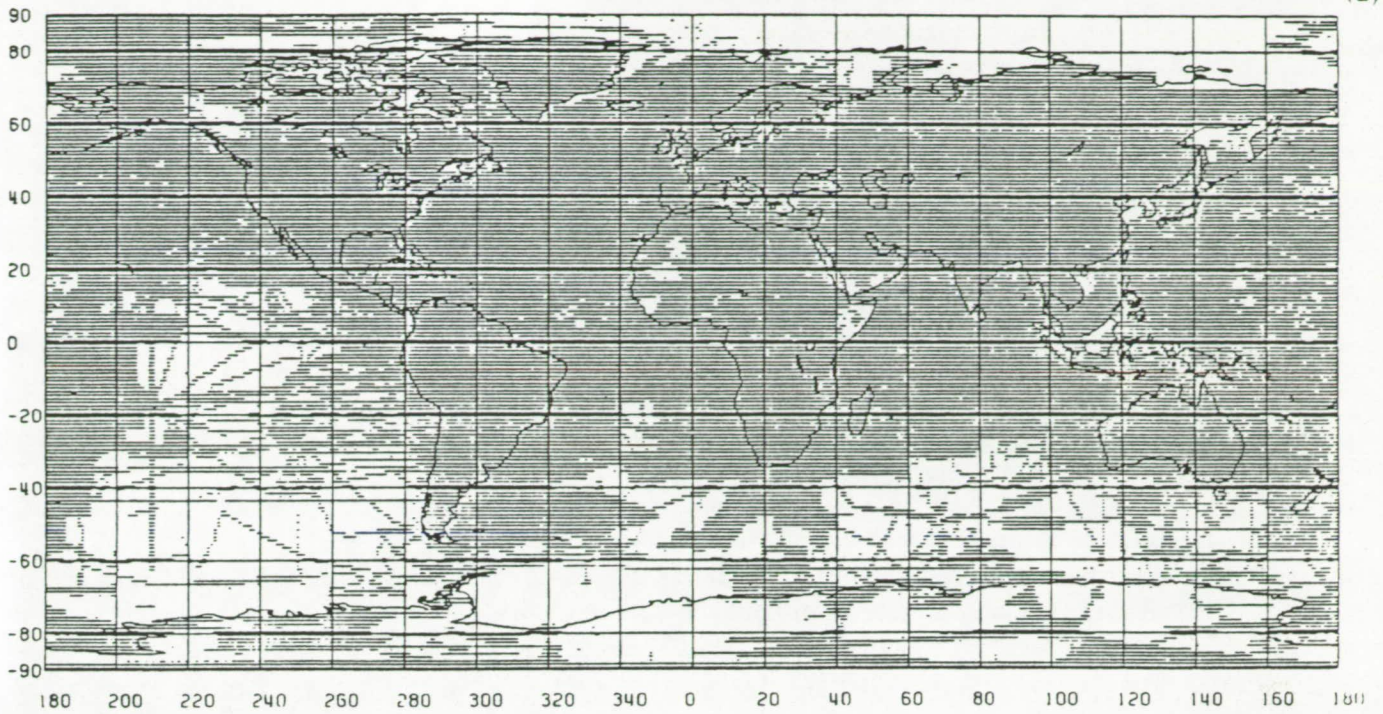
SEASAT GROUND TRACK DURING 3 DAY REPEAT CYCLE



(b)

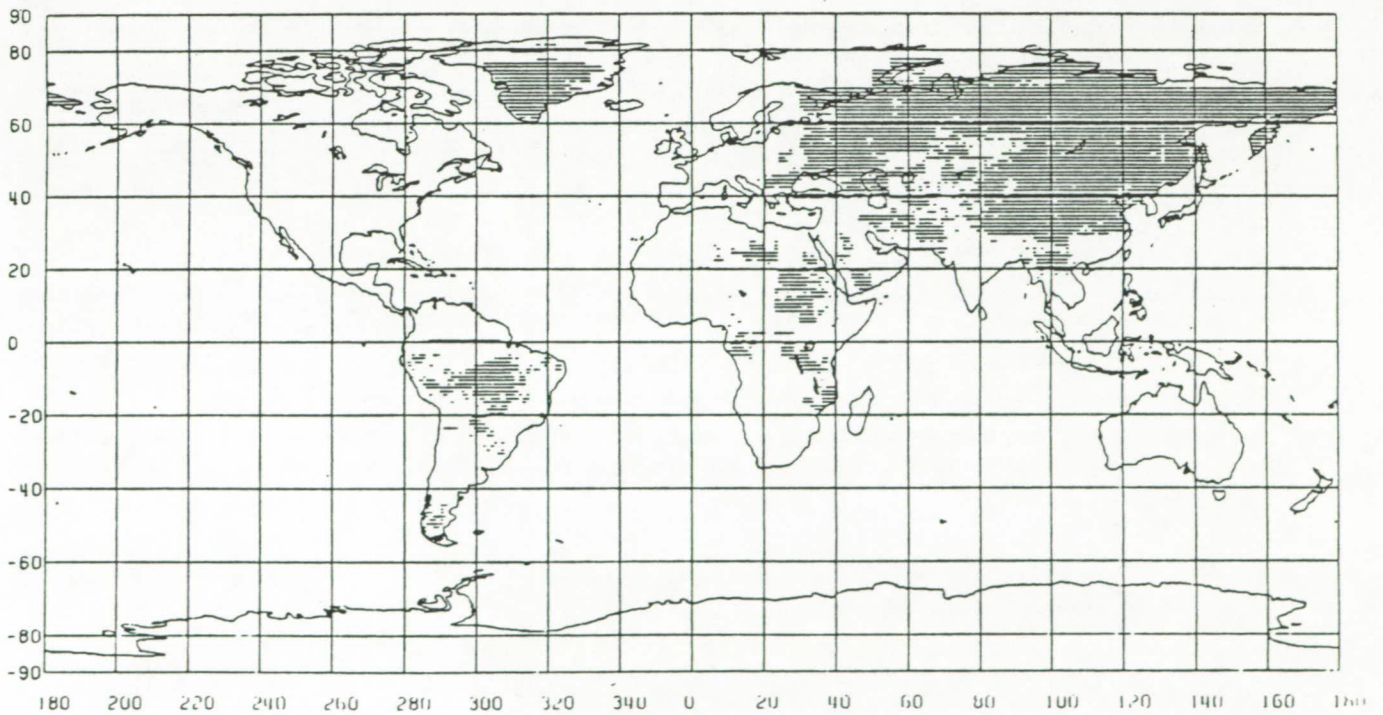
Figure 7. (a) A map of the SEASAT observations utilized in PGS-3337 from July 28 - August 15, 1978. (b) A map of the SEASAT observations utilized in PGS-3337 during the 3 day repeat orbit.

(a)



Location of the 48955 1°x1° Anomalies of the June 1986 Field.

(b)



Location of the 5684 Geophysical Anomalies of the June 1986 Field.

Figure 8. (a) The PGS-3337 data sample locations. In total, 48,955 1° X 1° equi-angular mean anomalies were used. (b) Geophysically predicted anomalies of the June 1986 field.

4.4 Improved Geoid Modeling

The satellite-only GEM-T1 rms coefficient error estimates (as calibrated in Lerch *et al.*, 1988) are compared with those obtained in the combination solution, PGS-3337 in Figure 6. While there is a great deal of improvement spanning all wavenumbers, the improvement in the intermediate and high degree terms is most significant. These models calibrate well with one another using the approach detailed in Lerch *et al.*(1988). Figures 9a,b give a coefficient by coefficient estimate of the uncertainties for both GEM-T1 and PGS-3337.

It is of interest to note that least squares *a priori* signal constraints bound the error obtained in a gravity solution to be no more than 100% of the expected power of the coefficient itself. The apparent improvement in GEM-T1 above degree 20 reflects the fact that the errors in the coefficients start to significantly approach 100% at these degrees. In PGS-3337, the coefficients do not display this severe behavior, even out to degree 50 (see Figure 6). Figures 10 and 11 compare the uncertainty in $h_{N_{ref}}$ for models complete to degree and order 36. These figures are obtained from the complete covariance propagation using: (a) GEM-T1 (Figure 10, top); (b) GEM-T1 plus surface gravimetry (Figure 10, bottom); (c) GEM-T1 plus SEASAT altimetry (Figure 11, top); and (d) PGS-3337 (GEM-T1 plus altimetry and surface gravimetry; Figure 11, bottom), respectively.

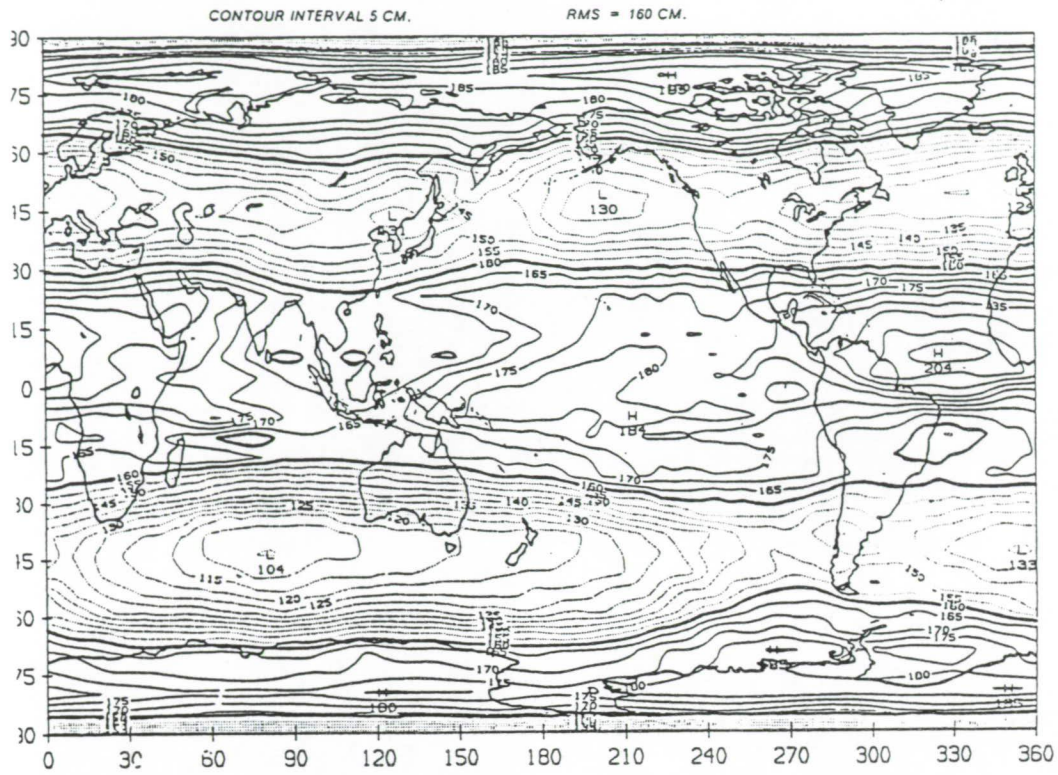
The geoid errors seen for GEM-T1 are banded. This pattern indicates that the C and S coefficients are equally well determined from the tracking data and little phase discrimination is sensed in the recovery. When data with local gravity discrimination are added to this solution, there is improvement in the geoid estimate in the sampled regions. This is especially true for the ocean areas that are homogeneously observed by the SEASAT altimeter.

Figures 12a,b present the geoid uncertainties for the 10×10 degree and order portions of the GEM-T1 and PGS-3337 models. There is still significant improvement, but both fields have significantly less error than the 65 cm rms signal expected for the QSST's contribution to the sea surface height. Therefore, $\bar{\eta}_A$ should be well defined. However, at about degree 8 to 10, the power in $\bar{\eta}_{A_{ann}}$ is equal to the error estimates for the gravitational (geoid) terms. This is shown more clearly in Figure 13. Our estimate that the geoid error is significantly larger than the global QSST signal beyond degree 10 led us to limit the QSST recovery to this degree and order. However, as shown later, our use of least squares *a priori* signal constraints minimize the impact of this cutoff.

4.5 Gravity Model Extension to Degree and Order 50: Impact on Error Assessment

Lerch *et al.*(1988) describe the extensive calibration activities that have been undertaken to test that the errors estimated for GEM-T1 are reliable and the optimum weighting and modeling needed for subsequently developed GEM/PGS models are understood. The three techniques that have been utilized in these calibration efforts are:

- (a) Calibrations comparing the differences in the coefficients between models with the expected values of these differences obtained using the respective solution error covariances. This



GEOID HEIGHT ERRORS USING PGS 3226 COVARIANCES
PGS 3226 = GEM-T1 + SURFACE GRAVIMETRY

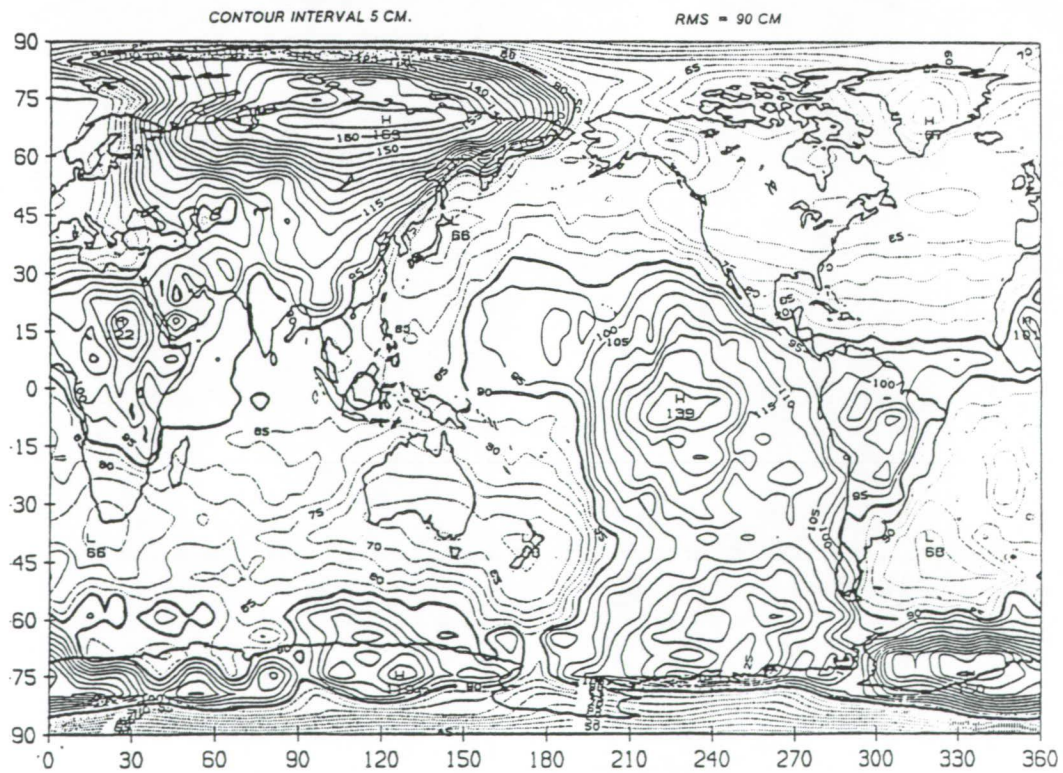
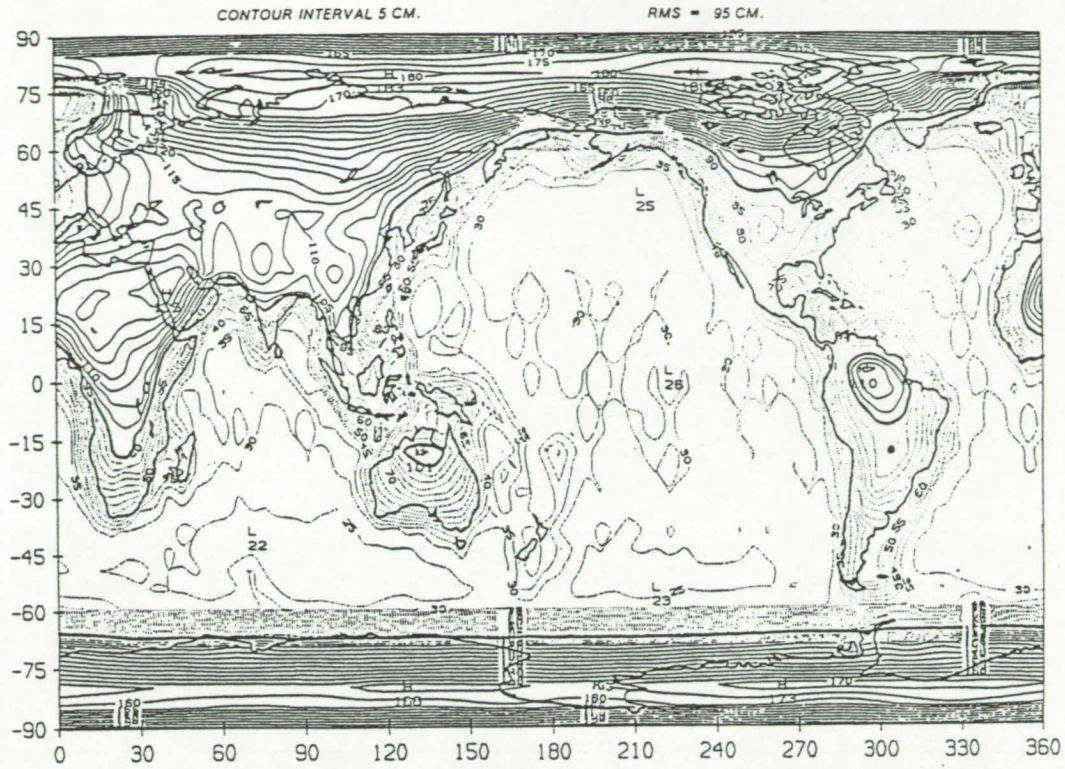
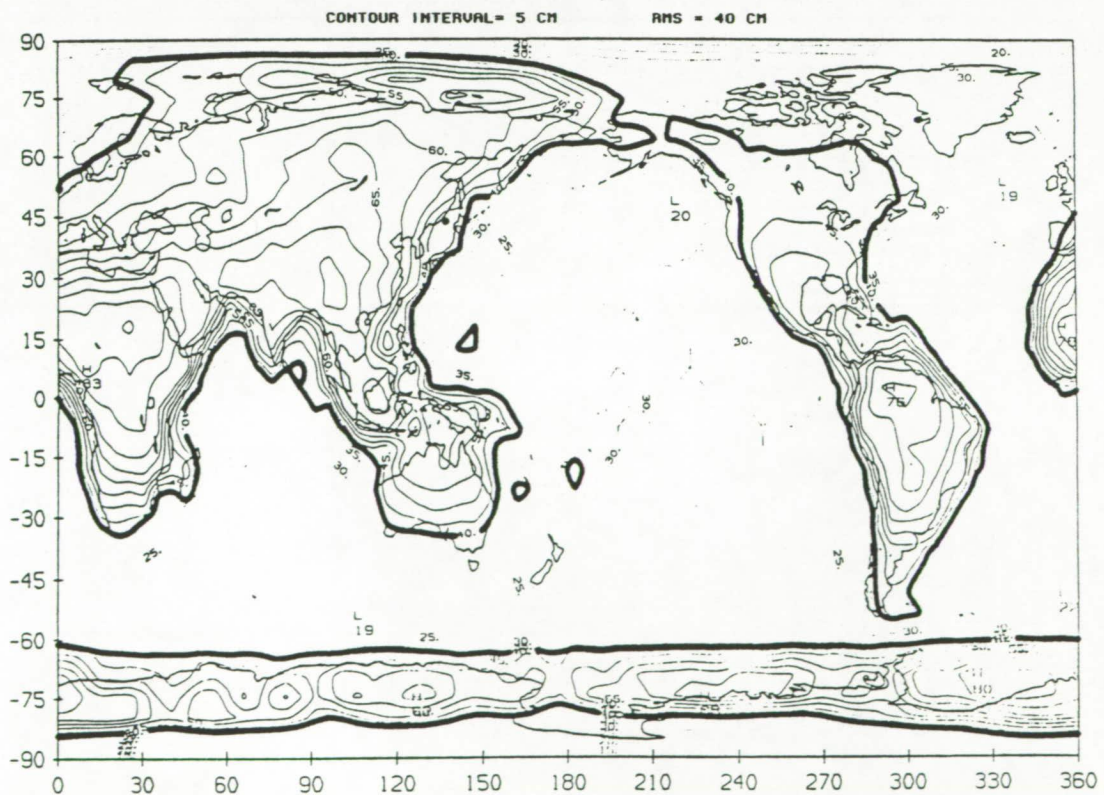


Figure 10. The uncertainty in global geoid height from the complete covariance propagation using GEM-T1 only (top) or GEM-T1 plus surface gravimetry (bottom).

GEOID HEIGHT ERRORS USING PGS 3299 COVARIANCES:
PGS 3229 = GEM-T1 + SEASAT ALTIMETRY



GEOID HEIGHT ERRORS USING PGS-3337 COVARIANCES:
PGS-3337 = GEM-T1 + SURFACE GRAVITY + ALTIMETRY



* TO DEGREE AND ORDER 36

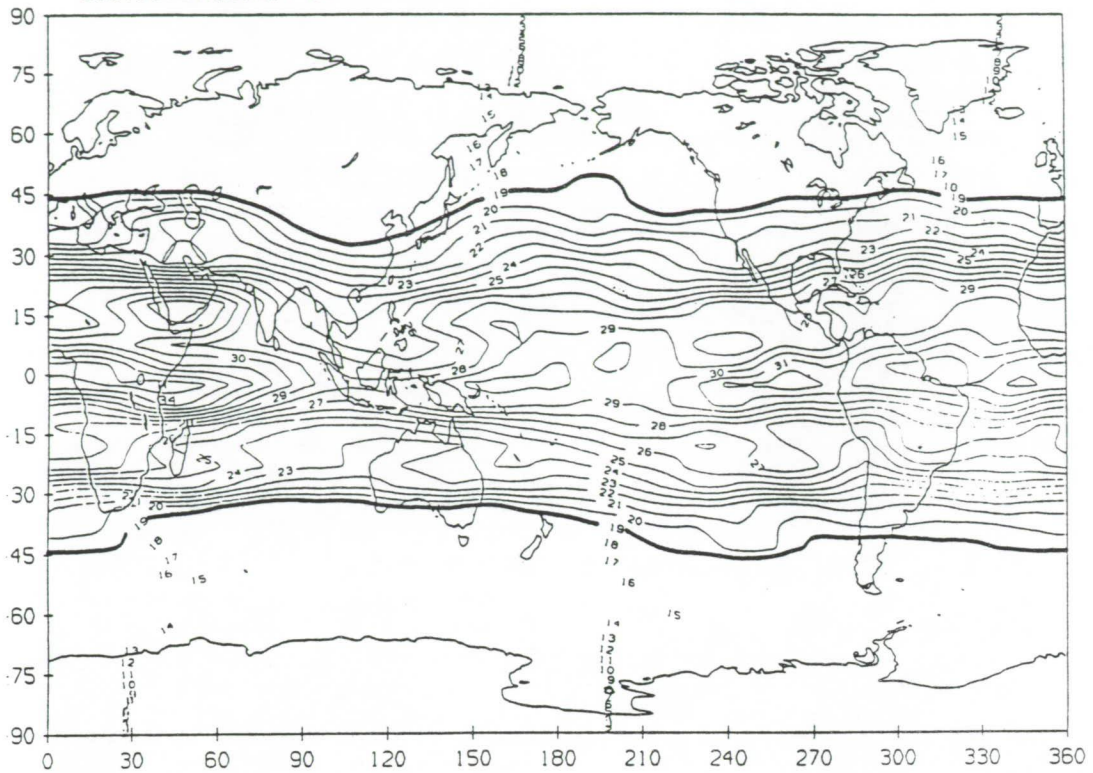
Figure 11. The uncertainty in global geoid height from the complete covariance propagation using GEM-T1 plus SEASAT altimetry (top) or PGS-3337 (bottom).

(a)

GEOID HEIGHT STANDARD DEVIATIONS USING GEM-T1 COVARIANCES TO 10 X 10

CONTOUR INTERVAL 1 CM.

RMS - 19 CM.



(b)

GEOID HEIGHT STANDARD DEVIATIONS USING PGS3337 COVARIANCES TO 10 X 10

CONTOUR INTERVAL 1 CM.

RMS - 9 CM.

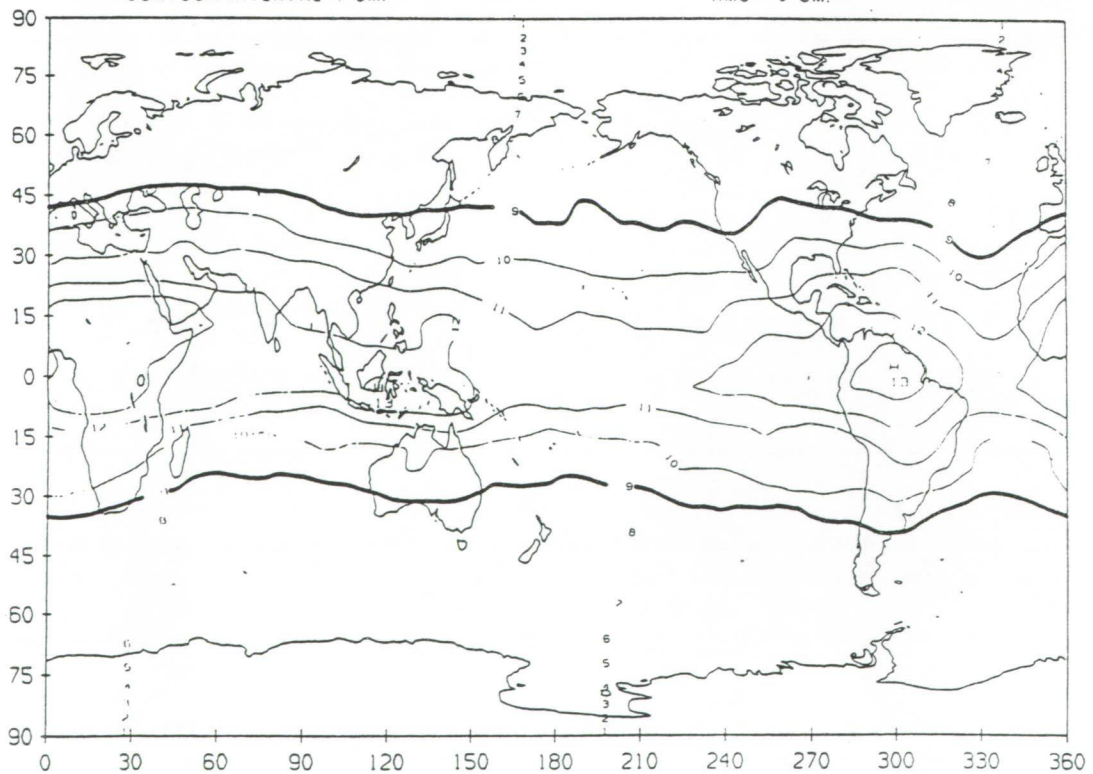


Figure 12. (a) The geoid uncertainties for the 10 X 10 degree and order portions of the GEM-T1 model. (b) The geoid uncertainties for the 10 X 10 degree and order portions of the PGS-3337 model.

Geoid Error and Dynamic Sea Surface Spectra

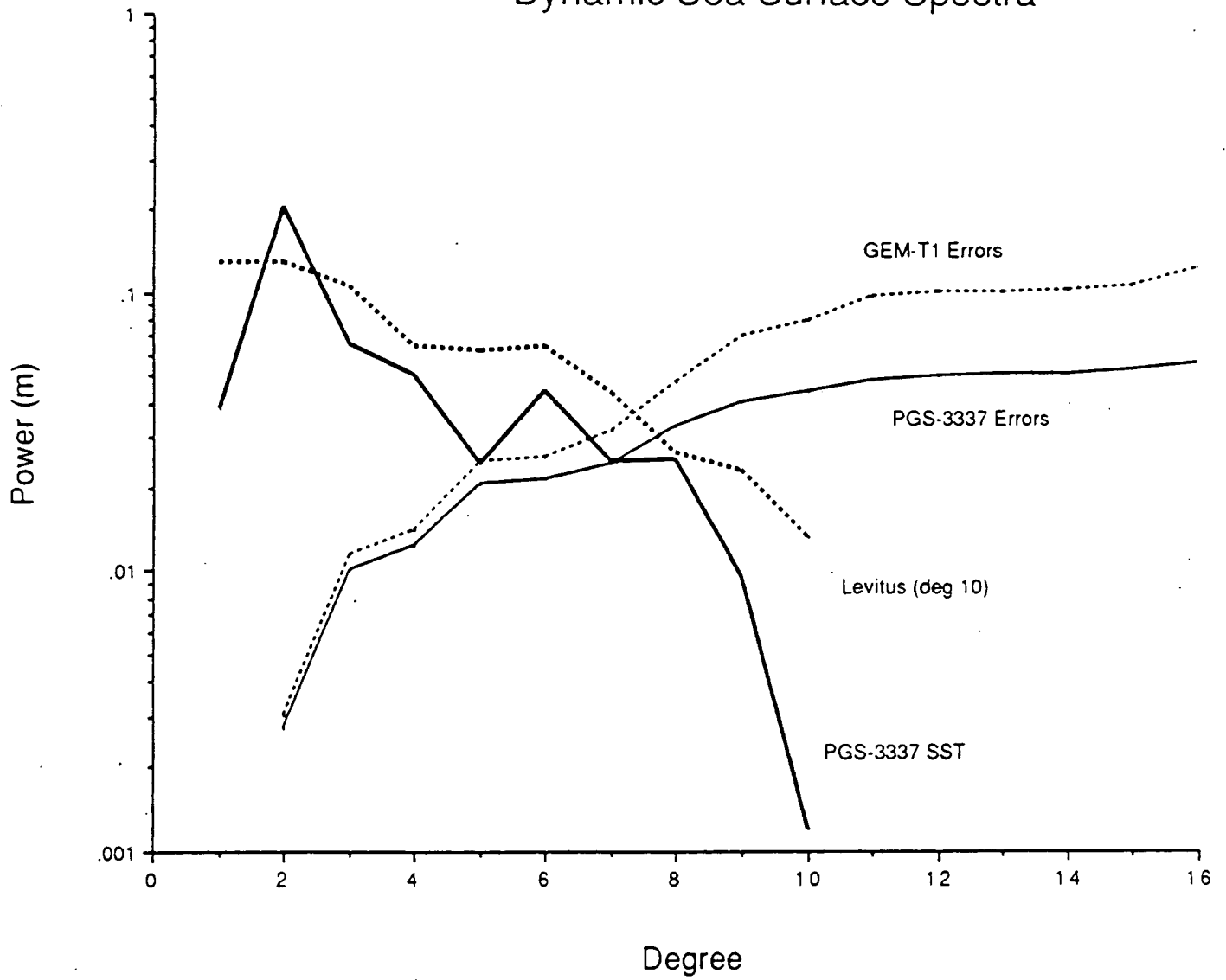


Figure 13. The power spectrum for $\bar{\eta}_A$ from PGS-3337 and $\bar{\eta}_\rho$.

method has been extensively utilized with complete fields as compared to their data subset solutions.

- (b) Calibrations using the eigenvectors of these subset solutions which parallels that of method (a), but now uses the off-diagonal information contained in the error covariances.
- (c) Calibrations using independent data sets, such as a comparison of GEM-T1 with the areal mean gravity anomalies independently derived from satellite altimetry.

Tests involving methods (a) and (b) attempt to locate data subsets of the solution in which a discrepancy exists between the change in the solved for solution parameters and the expectation of this change from the solution statistics when this data subset is incorporated into the solution at a given weight. This is of particular concern when the solution is made in the presence of unmodeled parameters and possible systematic errors. These tests are also useful for locating instances of aliasing in the models due to the truncation of the field recovery at specified limits. Hence, it is important to design solutions in such a way that the truncation of the gravity model has minimal effect on the calibration in order to avoid unnecessary downweighting of the data. We do not want the aliasing arising from a specific data set sensing information beyond the field limits to be confused with systematic errors existing within the data set itself. Clearly, if the subset data has sensitivity to higher degree and order terms, the model should be opened up to accommodate these effects. It is well known that the effects of truncation can be significant when the modeling is not complete to exhaust the signal in the data. However, this is not a problem properly accommodated through downweighting of the data, although having unmodeled signal due to truncation may give a false calibration reading that is similar to that arising from systematic errors. We have found that the presence of systematic error is a problem which requires redress through data downweighting.

All terms beyond the limits of the field recovery (*e.g.*, 36×36 for GEM-T1 and 50×50 for PGS-3337) are absolutely constrained to have zero value and are assumed to be perfectly determined because their direct effect is not present in the error covariances. However, any contributing signal to the satellite's motion or any surface geoidal feature mapped by the altimeter that is not represented by the recovered model's harmonic terms tends to be accommodated through leakage (aliasing) into the adjusted harmonic parameters. This is especially true in the case of gravitational effects on orbits where many different terms give rise to the same or similar orbital frequencies. The solution to this problem is to require the satellite model to exhaust the signal in the data while also controlling ill conditioning in the solution through the utilization of least squares constraints with an *a priori* power law. In this way, the field recovery is extended to higher degree and order (intentionally, to reduce the effects of aliasing and allow for satisfactory separation of the coefficients comprising the solution). The power in the recovered gravitational parameters are seen to taper off at high-degrees in models derived exclusively from tracking data; the signal is exhausted by the model parameters; and where signal is lacking the resulting coefficient uncertainties are constrained not to exceed 100% of their expected power as defined by the *a priori* power law with zero being the preferred *a priori* value.

The implicit assumption that the model is perfect beyond the limits of the field (although this is clearly erroneous since zero is the value for all of these harmonic terms) can lead to under-reported error estimates when the modeling is not complete enough to exhaust all data signal. This especially

applies to the case of altimeter data, for although we have corrected the observations for geoidal effects above degree 50 and masked out regions having steep geoidal gradients, errors in these corrections are surely present. Therefore, leakage from uncorrected high-degree geoidal signals are likely to have influenced models using these data. Furthermore, these high-degree errors are not well detected in methods (a) and (b) when GEM-T1 is the subset model. This "satellite-only" model cannot be used to calibrate the high-degree terms from comprehensive altimeter/surface gravity models due to the limited accuracy it has since most of these coefficients approach 100% error. The value in this test is that GEM-T1 serves to calibrate the low degree terms of the combination model and the combined model serves to calibrate the high-degree terms of GEM-T1. Unfortunately, the reverse is not true. Also, by including the surface gravimetry and satellite altimetry in the models, method (c) is made more difficult, because independent global data available for testing these fields are now lacking.

To demonstrate this point about aliasing error, we have solved the PGS-3337 normals both to degree and order 36 (denoted as PGS-3325) and 50. The resulting error covariances were calibrated by using the subset technique of method (a) and (b) above by using GEM-T1 plus surface gravity as the subset model (*i.e.*, the data in GEM-T1 plus surface gravity are wholly contained in either PGS-3325 or PGS-3337). The surface gravity normals were corrected for contributions above degree 36 in PGS-3325 and above degree 50 in PGS-3337. Figure 14 compares the resulting estimates of the rms coefficient errors by degree for these models. The same data should yield similar parameter uncertainties, if these parameters were uncorrelated and the data set is large. This situation should remain unchanged even in the presence of a greater number of adjusting parameters. Furthermore, since the altimeter data were corrected for geoid contributions above degree 50, PGS-3325 should suffer from much more spectral leakage arising from the signal remaining in the altimeter data from degree 37 to 50. However, Figure 14 indicates that the estimated errors for the smaller field are too optimistic or too conservative for the larger field. The calibration tests gave $k = 1.00$ with PGS-3325 and $k = 0.75$ with PGS-3337 and indicate that the errors are too conservative for PGS-3337 by as much as 25% for these high-degree terms. The reason for this calibration result is that the weight for the altimeter data was originally calibrated for the PGS-3325 model and then carried into the PGS-3337 model, where the weight should have been upgraded. On the basis of these two calibration tests the methods (a) and (b) can detect the aliasing effect of the truncation error, and hence the higher degree terms of 37 to 50 in PGS-3337 may likewise have conservative estimates.

RMS OF COEFFICIENT ERROR PER DEGREE

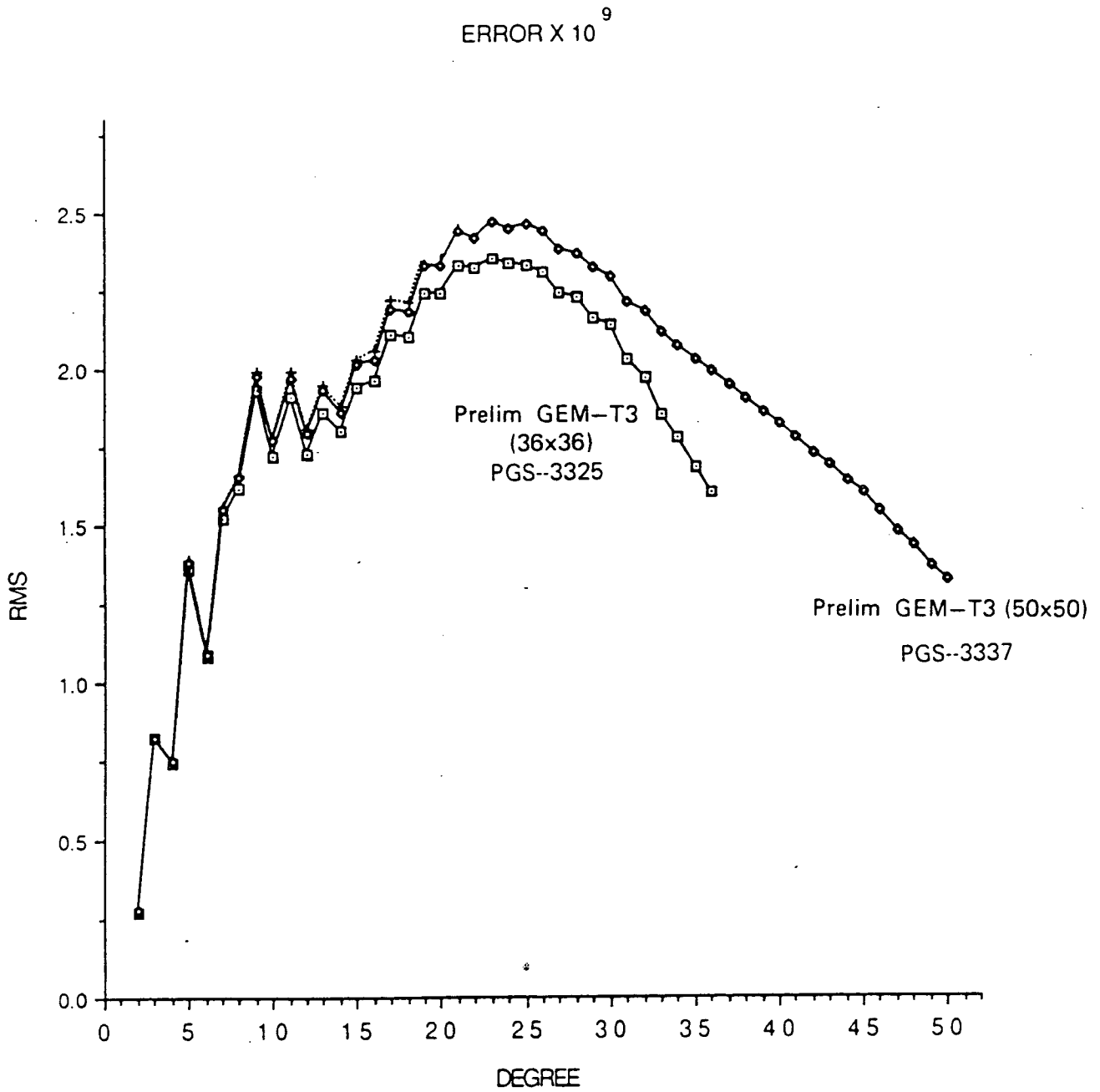


Figure 14. A comparison of the PGS-3325 and PGS-3337 rms coefficient errors by degree.

5 Dynamic Topography Solution

The measurement of QSST has undergone considerable evolution in the past decade. Traditional oceanographic solutions based on classical hydrodynamic principles have been obtained with variable success for several years. These solutions are primarily based on shipborne measurements of density (*i.e.*, temperature and salinity) along ship tracks. This approach suffers from the data distribution not being global and being generally scattered with respect to time. One can attempt to overcome the temporal problems by computing averaged solutions, but as noted by Engelis (1987), these results cannot strictly be considered a true measure of the long-term mean. The introduction of altimetry provides the observational means for recovering the global QSST signal with more accuracy.

In this paper, we have describe the philosophy, techniques and procedures for a simultaneous solution of gravity and sea surface topography from the combination of multi-satellite tracking data, surface gravimetry, and SEASAT altimetry. The solution takes its form as the coefficients of a normalized surface spherical harmonic expansion such as given in Equation (10). In the PGS-3337 gravitational model/QSST solution, the $\bar{\eta}_{A_{annm}}$ are solved completely to degree and order ten. This level of resolution was selected based on the work of Engelis (1987).

5.1 QSST from *in situ* Climatological Data ($\bar{\eta}_\rho$)

Engelis (1987) provided an analysis of the harmonic representation possible for $\bar{\eta}_\rho$. From the oceanographic data, Engelis found the results shown in Tables 5 and 6. Clearly, from Table 6, the Gibbs effect is a serious problem in the recovery of $\bar{\eta}_{\rho_{annm}}$ if the land areas are assigned zero values to achieve a global data distribution. While the harmonics in such a solution are virtually uncorrelated, contrary to solutions obtained from ocean-only data, the land-ocean interfaces and the flat land signal yield less acceptable behavior than over the ocean area both in terms of power and rms of fit to the original data. When the ocean area alone is sampled, a 36×36 solution for harmonics behaves poorly if unconstrained (*i.e.*, too much power is in the recovered harmonics, as shown in Table 6). This effect would require a strong application of the constraints that controls the numerical stability of the solution. Major problems also arise from the uncertainty in the geoid determination if a solution for $\bar{\eta}_{A_{annm}}$ to degree and order 36 is attempted. Therefore, the solution design of choice is a least squares approach employing constraints and estimating a QSST model complete to some degree and order as warranted by the estimated errors in the simultaneous gravitational model determination.

On the basis of Table 6, a 10×10 QSST model was expected to yield $\bar{\eta}_A$ with sub-decimeter resolution. The power spectra for $\bar{\eta}_A$ and $\bar{\eta}_\rho$ (Case 1 in Table 6) are shown in Figure 13. Also shown are the estimates of the geoid error found in GEM-T1 and PGS-3337, respectively. It is unwarranted to carry the solution for $\bar{\eta}_{A_{annm}}$ beyond the 10th degree given the size of geoid errors beyond this level of resolution.

Table 5: Spherical Harmonic Expansion of $\bar{\eta}_\rho$ by Engelis (1987)

Case	Mean Height (meters)	Rms Power (meters)
I. Levitus (1982)	2.02	0.80
II. Levitus w/Lisitzin (1974) for Med. Sea	2.02	0.79
III. Set II without Northernmost Latitudes	2.01	0.62

Table 6: Spherical Harmonics of $\bar{\eta}_\rho$ - Set III in Table 5

Max deg for expansion	Method	Residual to Fit (meters)	Rms Power (meters)
10	Least-squares (ocean-data only)	0.07	0.63
10	Harmonic Analysis (global; zero for land)	0.19	0.37
36	Least-squares (ocean-data only)	0.01	7.52

5.2 Definition of $\bar{\eta}_A$ with Respect to $\bar{\eta}_\rho$

The geoid errors prevent the computation of accurate higher wavelengths in the dynamic topography with the current tracking data used in GEM-T1/PGS-3337. However, the geoid over the oceans is well represented with the present data sampling. This can be seen in the estimated geoid errors for PGS-3337 shown in Figures 11 (bottom) and 12b. On this basis, QSST models extending to degree and order 16 warrant future consideration.

The $\bar{\eta}_{A_{ann}}$, in units of centimeters, for PGS-3337 are given in Table 7. These coefficients represent the displacement of the sea surface, temporally averaged over the lifetime of the SEASAT mission, with respect to the simultaneously determined PGS-3337 geoid.

As discussed in Section 2.2.3, both the direct and indirect effects (*i.e.*, the change in the geoid due to the tidally induced mass deformation of the solid Earth) caused by the zero-frequency tides are modeled separately from the geopotential coefficients. With the discussion restricted to the dominating contribution of the second degree potential, the total tidal effect on the potential on a point fixed in space is

$$\Delta U = (1 + k_2)U_2 \quad (29)$$

where the first term accounts for the direct luni-solar tidal potential and the second term is the induced effect due to the Earth's elastic response.

Equation (29) can be separated into a constant and time varying part as

$$\Delta U = (1 + k_s)U_{2c} + (1 + k_2)U_{2t} \quad (30)$$

where k_s is the secular Love number associated with the permanent deformation. The quantity

Table 7: Comparison of $\bar{\eta}_{A_{anm}}$ and $\bar{\eta}_{\rho_{anm}}$

n m		$\bar{\eta}_A$ (PGS-3337)		$\bar{\eta}_\rho$ (Engelis, 1987)		n m		$\bar{\eta}_A$ (PGS-3337)		$\bar{\eta}_\rho$ (Engelis, 1987)	
		\tilde{C}_{nm}	\tilde{S}_{nm}	\tilde{C}_{nm}	\tilde{S}_{nm}			\tilde{C}_{nm}	\tilde{S}_{nm}	\tilde{C}_{nm}	\tilde{S}_{nm}
1	0	-0.0497	0.0000	0.1297	0.0000	1	1	-0.0204	-0.0384	-0.1766	0.0360
2	0	-0.4384	0.0000	-0.2803	0.0000	2	0	*-0.3232			
2	1	-0.0920	0.0791	-0.0452	0.0099	2	2	-0.0041	0.0555	0.0261	0.0087
3	0	0.1558	0.0000	0.2663	0.0000	3	1	-0.0247	-0.0307	-0.0194	-0.0111
3	2	-0.0063	-0.0166	0.0507	-0.0141	3	3	-0.0392	-0.0403	-0.0391	0.0295
4	0	-0.0931	0.0000	0.1467	0.0000	4	1	-0.0008	0.0940	0.0123	0.1053
4	2	-0.0149	-0.0134	0.0201	0.0368	4	3	-0.0279	0.0212	0.0010	0.0239
4	4	-0.0238	-0.0576	-0.0432	-0.0005						
5	0	0.0084	0.0000	0.1242	0.0000	5	1	-0.0240	0.0009	0.0008	0.1494
5	2	-0.0100	0.0424	-0.0129	0.0470	5	3	-0.0154	0.0005	-0.0268	0.0221
5	4	-0.0595	0.0098	-0.0337	-0.0030	5	5	-0.0040	0.0030	-0.0114	-0.0029
6	0	0.1280	0.0000	0.1536	0.0000	6	1	-0.0512	0.0657	-0.0083	0.1252
6	2	-0.0058	-0.0017	-0.0824	0.0286	6	3	-0.0272	-0.0248	-0.0199	-0.0286
6	4	-0.0237	-0.0031	-0.0417	-0.0416	6	5	0.0066	0.0028	0.0283	-0.0143
6	6	0.0156	-0.0022	0.0012	0.0017						
7	0	-0.0504	0.0000	-0.0754	0.0000	7	1	0.0562	-0.0376	0.0094	0.1012
7	2	0.0219	0.0070	-0.0807	0.0223	7	3	0.0213	-0.0086	-0.0045	-0.0108
7	4	0.0063	-0.0240	-0.0366	-0.0472	7	5	-0.0012	-0.0099	0.0217	-0.0257
7	6	0.0073	-0.0025	0.0183	0.0138	7	7	0.0051	0.0051	-0.0037	0.0006
8	0	0.0439	0.0000	0.0057	0.0000	8	1	-0.0734	-0.0181	-0.0582	-0.0090
8	2	0.0057	-0.0081	-0.0756	0.0102	8	3	0.0046	-0.0043	0.0082	-0.0200
8	4	0.0326	-0.0095	0.0092	-0.0281	8	5	-0.0220	-0.0096	0.0174	-0.0210
8	6	-0.0038	-0.0160	0.0195	-0.0015	8	7	-0.0265	-0.0118	-0.0142	0.0034
8	8	-0.0047	0.0013	-0.0027	-0.0063						
9	0	-0.0202	0.0000	-0.0651	0.0000	9	1	0.0083	0.0050	0.0248	0.0084
9	2	-0.0174	-0.0008	-0.0326	-0.0399	9	3	0.0007	0.0149	-0.0103	-0.0144
9	4	0.0038	-0.0025	0.0151	-0.0237	9	5	-0.0177	-0.0066	0.0138	-0.0189
9	6	-0.0113	0.0010	0.0238	0.0021	9	7	-0.0068	0.0023	-0.0079	0.0026
9	8	0.0021	0.0041	-0.0080	0.0048	9	9	0.0013	0.0109	0.0017	-0.0050
10	0	-0.0015	0.0000	0.0112	0.0000	10	1	0.0024	-0.0016	0.0217	-0.0356
10	2	-0.0009	0.0011	-0.0064	-0.0154	10	3	-0.0008	0.0016	0.0018	-0.0154
10	4	0.0006	-0.0007	0.0225	-0.0140	10	5	0.0005	-0.0008	-0.0007	0.0006
10	6	-0.0010	0.0010	0.0205	0.0014	10	7	0.0009	0.0001	0.0029	0.0029
10	8	-0.0023	0.0008	-0.0046	-0.0000	10	9	-0.0009	0.0016	-0.0018	0.0080
10	10	0.0007	0.0001	-0.0018	-0.0017						

*PGS-3337 C_{20} coefficient after corrections for direct and indirect permanent tidal deformation.

k_s has been introduced and distinguished from k_2 in order to separate the permanent deformation effect from the temporally varying term. It is the first term in Equation (30) that needs to be considered if $\bar{\eta}_A$ from PGS-3337 is to be compared to $\bar{\eta}_\rho$ that is referenced to a "surface of no motion".

The effects of the permanent luni-solar tides (*i.e.*, the M_0 and S_0 constituents at frequency $f = 0$) need to be accounted for in our recovery of $\bar{\eta}$. This consideration is important because these permanent tides have not been included in the computation of the PGS-3337 geoid, whereas the ocean surface tracked by the altimeter contains this tidal signal. A correction for the permanent tides recommended by the Standard Earth Tide Committee at the 1983 International Union of Geodesy and Geophysics (IUGG) Assembly is

$$\bar{\eta} = \bar{\eta}_1 - (h_{N_s} + h_{N_m})\left(\frac{3}{2}\sin^2\phi - \frac{1}{2}\right) \quad (31)$$

where:

$\bar{\eta}_1$ the surface height point value computed from the $\bar{\eta}_{A_{annm}}$ given in Table 7.

h_{N_s} = -5.95 cm, which is employed to refer $\bar{\eta}_A$ to the so-called "zero-geoid" accounting for the Honkasalo term.

h_{N_m} = -19.8 cm, which refers the QSST surface to the "mean geoid" accounting for the direct permanent tidal effects (see Standard Earth Tide Committee Report, 1983).

Although there is some uncertainty in the value that should be used for the secular Love number in Equation (30), as Equation (16) has indicated, a value of $k_2 = 0.30$ was modeled for all background solid Earth tides including those of $f = 0$. The accepted value of the secular Love number is closer to 0.96. The PGS-3337 recovered value for C_{20} would absorb any observed discrepancy that is detected by the tracking data resulting from our implied modeling of $k_s = 0.30$.

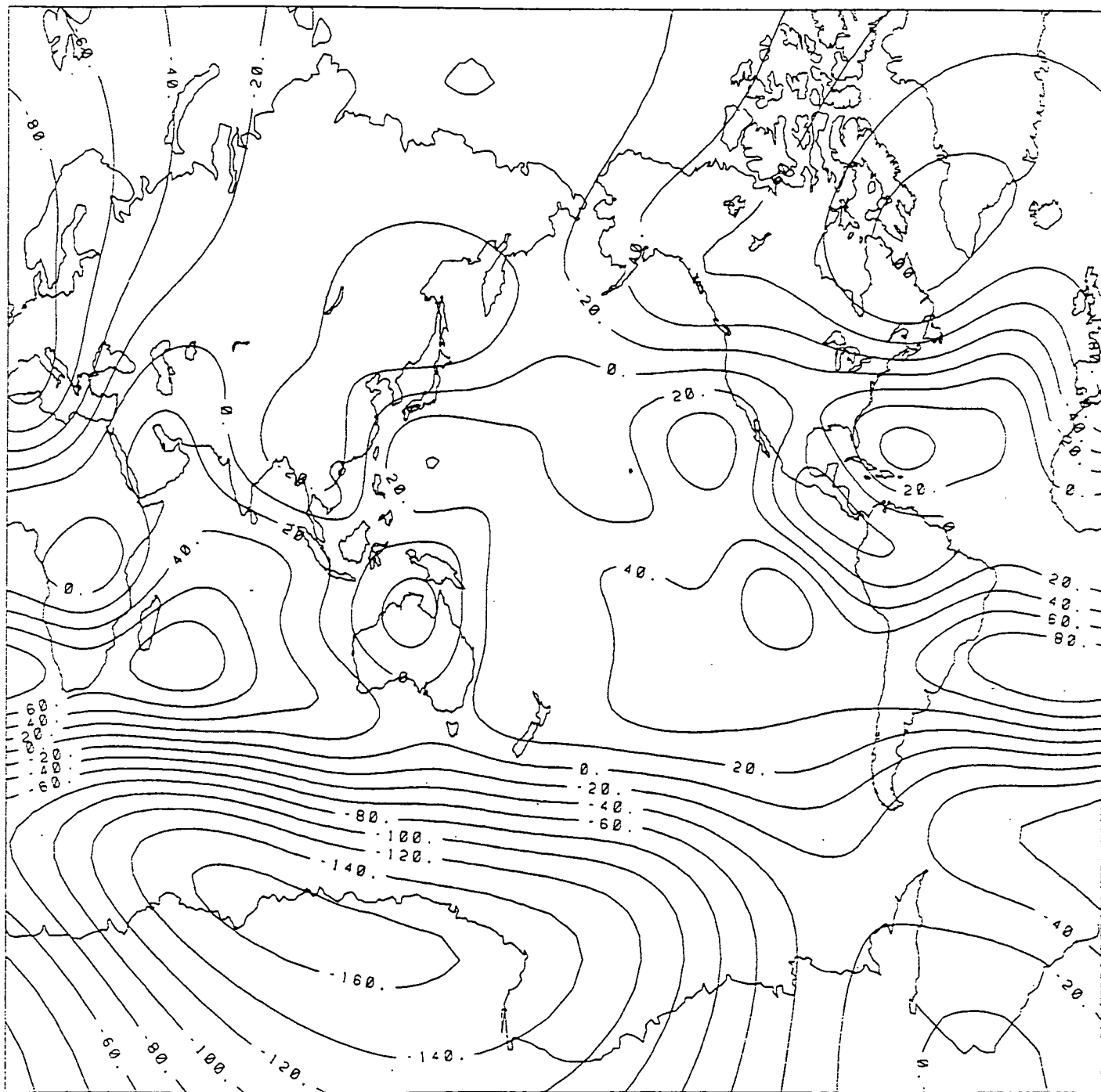
The combined use of Equation (31) and $h_{N_{r,s}}$, defined by the harmonics of PGS-3337 produces a reference surface for $\bar{\eta}_A$ that approximates that of the "surface of no motion" used for $\bar{\eta}_\rho$, thereby permitting a comparison of models. It is hoped that as long as a consistent reference surface is used, $\bar{\eta}_A$ can be understood within an oceanographic context.

5.3 The SEASAT Estimate of QSST ($\bar{\eta}_A$)

After the correction for the permanent tides were applied to $\bar{\eta}_A$, the QSST model from PGS-3337 was contoured and is shown in Figure 15. Similarly, a gridding of the 10×10 harmonic representation of $\bar{\eta}_\rho$ is shown in Figure 16. These models are further compared in Plate 2.

Several common features can be identified in Figures 15 and 16 and in Plate 2. For example, prominent topographic highs in the middle latitudes of both the North and South Atlantic are notable, as well as lesser highs in the Eastern Pacific. The North Atlantic subtropical gyre seems more defined in $\bar{\eta}_A$ than in $\bar{\eta}_\rho$, although the magnitudes are about the same (0.3 m versus 0.25 m). The South Atlantic subtropical gyre shows a stronger (0.8 m versus 0.5 m) and more defined high in $\bar{\eta}_A$ than $\bar{\eta}_\rho$. The high in the subtropical western Indian Ocean is seen in both maps with similar

PGS 3337 QSST SURFACE

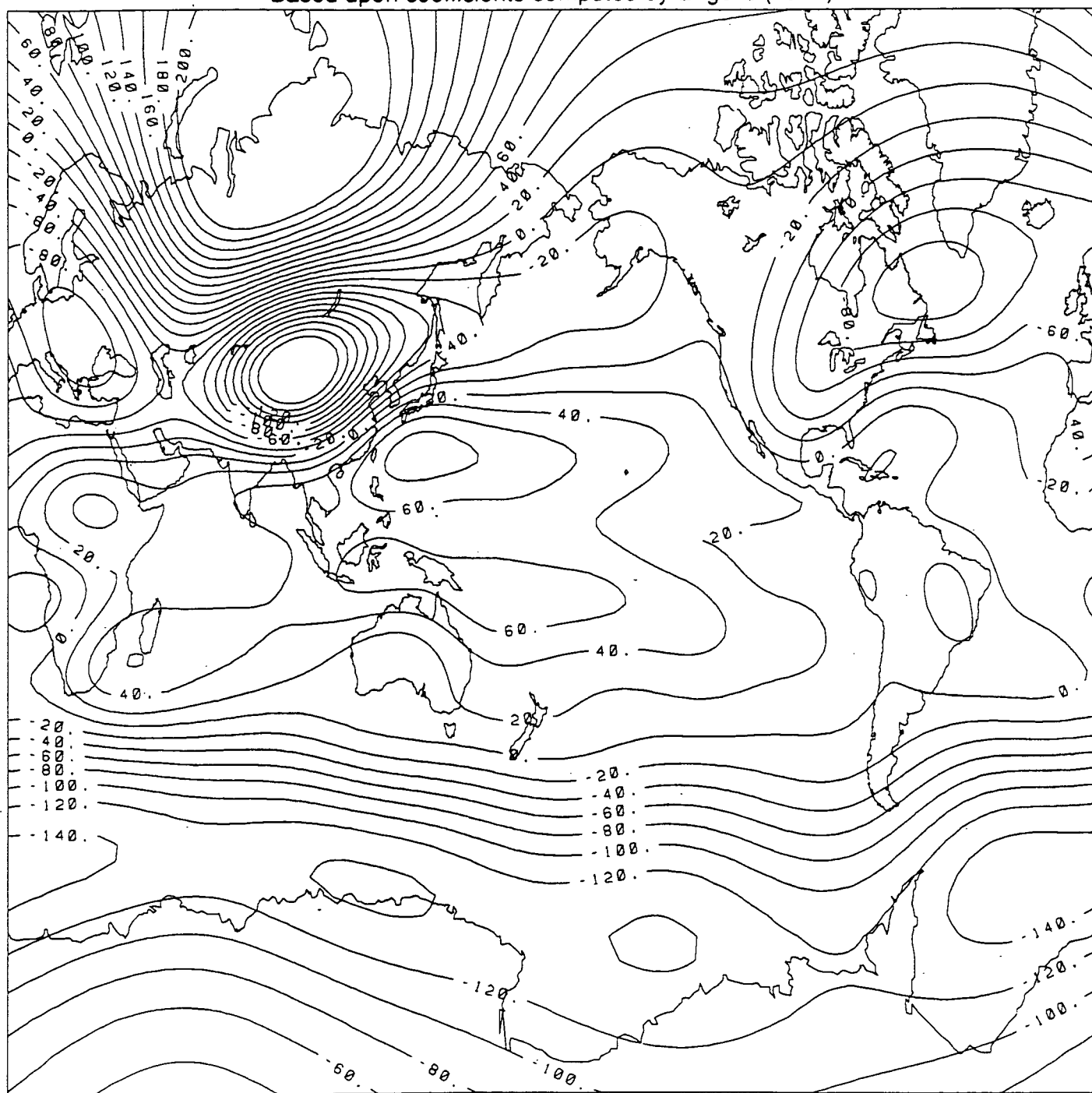


CONTOUR INTERVAL: 0.2 m

Figure 15. The QSST model from PGS-3337 after the correction for the permanent tides. The contour interval is 0.2 m.

LEVITUS QSST SURFACE

Based upon coefficients computed by Engelis (1986)



CONTOUR INTERVAL: 0.25 m

Figure 16. The 10 X 10 harmonic representation of $\bar{\eta}_\rho$. The contour interval is 0.25 m.

amplitude. The zero contour occurs at roughly the same location throughout the Southern Ocean and the strong north/south gradient between 40° S and 60° S is comparable.

The $\bar{\eta}_A$ and $\bar{\eta}_\rho$ fields are less similar in the Pacific. The North Pacific subtropical gyre is much weaker in $\bar{\eta}_A$ (0.3 m) than $\bar{\eta}_\rho$ (0.5 m). The subtropical eastern North Pacific is higher than the west in $\bar{\eta}_A$, unlike $\bar{\eta}_\rho$. Likewise, the east/west gradient across subtropical gyre in the South Pacific is reversed in $\bar{\eta}_A$ compared to $\bar{\eta}_\rho$. However, the magnitude in the western subtropical South Pacific is comparable.

The mean ocean current structures can be estimated by making use of the surface geostrophic current relationship described in Equation 4. The gyres implied from $\bar{\eta}_A$ are shown in Figure 17. The map is intended to provide a qualitative picture of the ocean current field. Again for comparison, the geostrophic currents implied from $\bar{\eta}_\rho$ are plotted in Figure 18. The same vector scaling has been used in both figures and immediately noticeable is the weaker strength in the currents obtained from $\bar{\eta}_\rho$.

The SEASAT derived $\bar{\eta}_A$ may contain longer period effects, such as seasonal variations because it is only a three month average. The data were collected in the late summer and early autumn months. During this period, the sea level is higher in the Northern Hemisphere and lower in the Southern Hemisphere than the annual mean, primarily because of upper ocean thermal expansion (Gill and Niiler, 1973). We have made a seasonal analysis of $\bar{\eta}_\rho$. Seasonal variations have an amplitude of order 10 cm (Koblinsky, 1988). These variations are smaller than the major discrepancies found between $\bar{\eta}_A$ and $\bar{\eta}_\rho$. Therefore, we discount seasonal effects as being the primary cause for the discrepancy between the altimeter and climatology solutions.

5.4 Error Estimates for $\bar{\eta}_A$

Least squares with *a priori* signal constraints influence the solution in two ways. First, it places bounds on the errors within the solution. The estimated errors will not exceed 100% of the expected power for a given signal. Second, this estimation technique constrains the error power in the adjusted harmonic coefficients. It prevents them from obtaining unreasonably large values. Both these aspects of the method can be observed when evaluating the error estimates for $\bar{\eta}_A$.

The effect of the least squares constraint on $\bar{\eta}_{A_{annm}}$ power can be seen by comparing $\bar{\eta}_\rho$ (Figure 18) with $\bar{\eta}_A$ (Figure 16). Only in $\bar{\eta}_A$ was the least squares constraint applied. Over the oceans, these models are quite similar. However, their behavior over land areas where altimeter coverage is lacking, especially over Asia, shows excess power when the simple least squares solution was used to estimate $\bar{\eta}_{\rho_{annm}}$. The utilization of the constraint in $\bar{\eta}_A$ exhibits more stable behavior over unrepresented areas. Of course, neither field has meaningful values over land. But based on the basis of these results, the values in nearshore areas are probably better behaved in a solution using signal constraints. Tapley *et al.* (1988) used downweighted zero values over land to achieve this same end in their estimate of $\bar{\eta}_A$. However, as described in the previous section, the Gibbs effect is a possible problem when adopting this approach, and the weighting of the land data may be critical.

PGS 3337 OCEANIC FLOW
IMPLIED BY QSST COEFFICIENTS

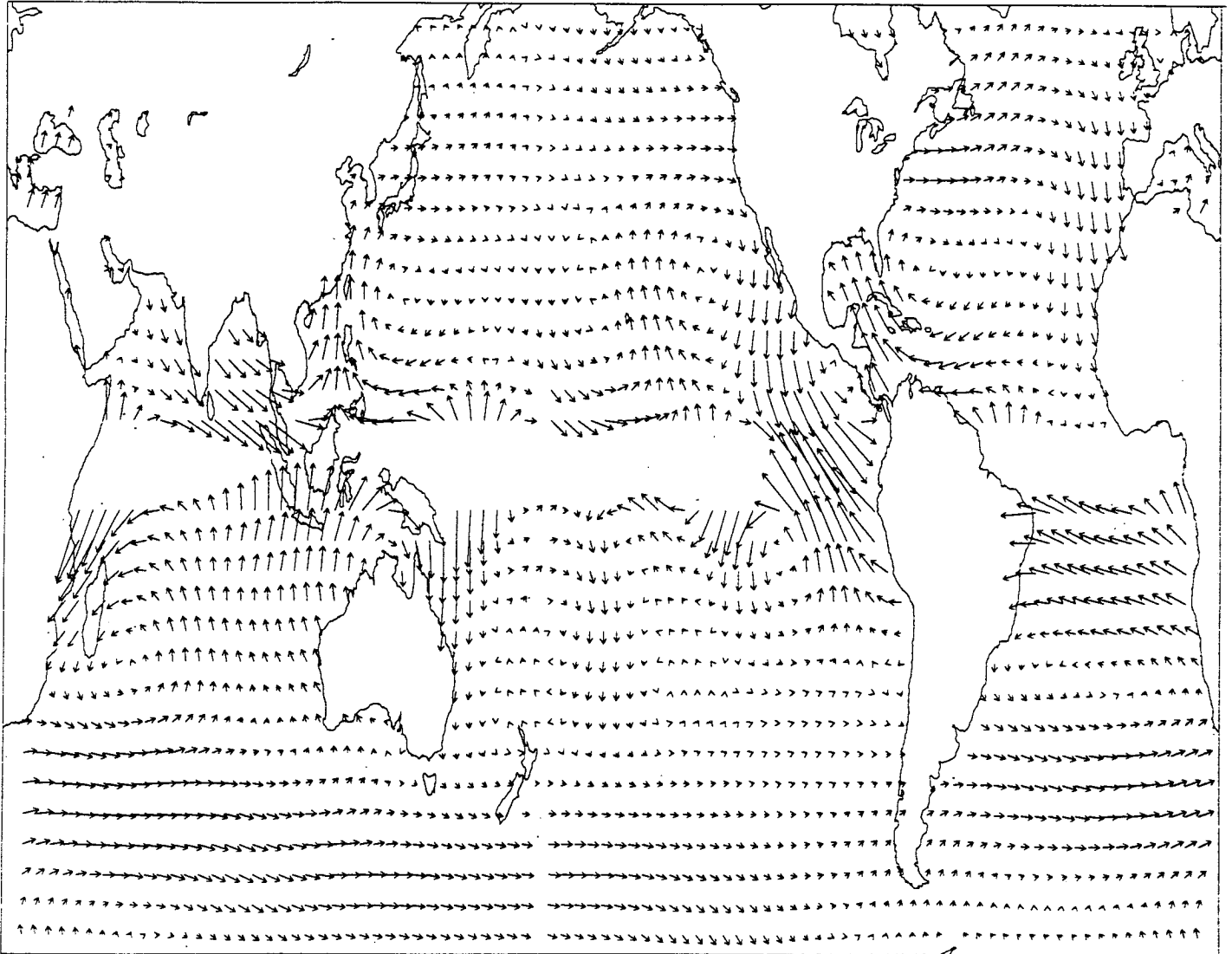


Figure 17. The geostrophic flow implied by $\bar{\eta}_{A\alpha nm}$ from PGS-3337.

LEVITUS OCEANIC FLOW
IMPLIED BY QSST COEFFICIENTS

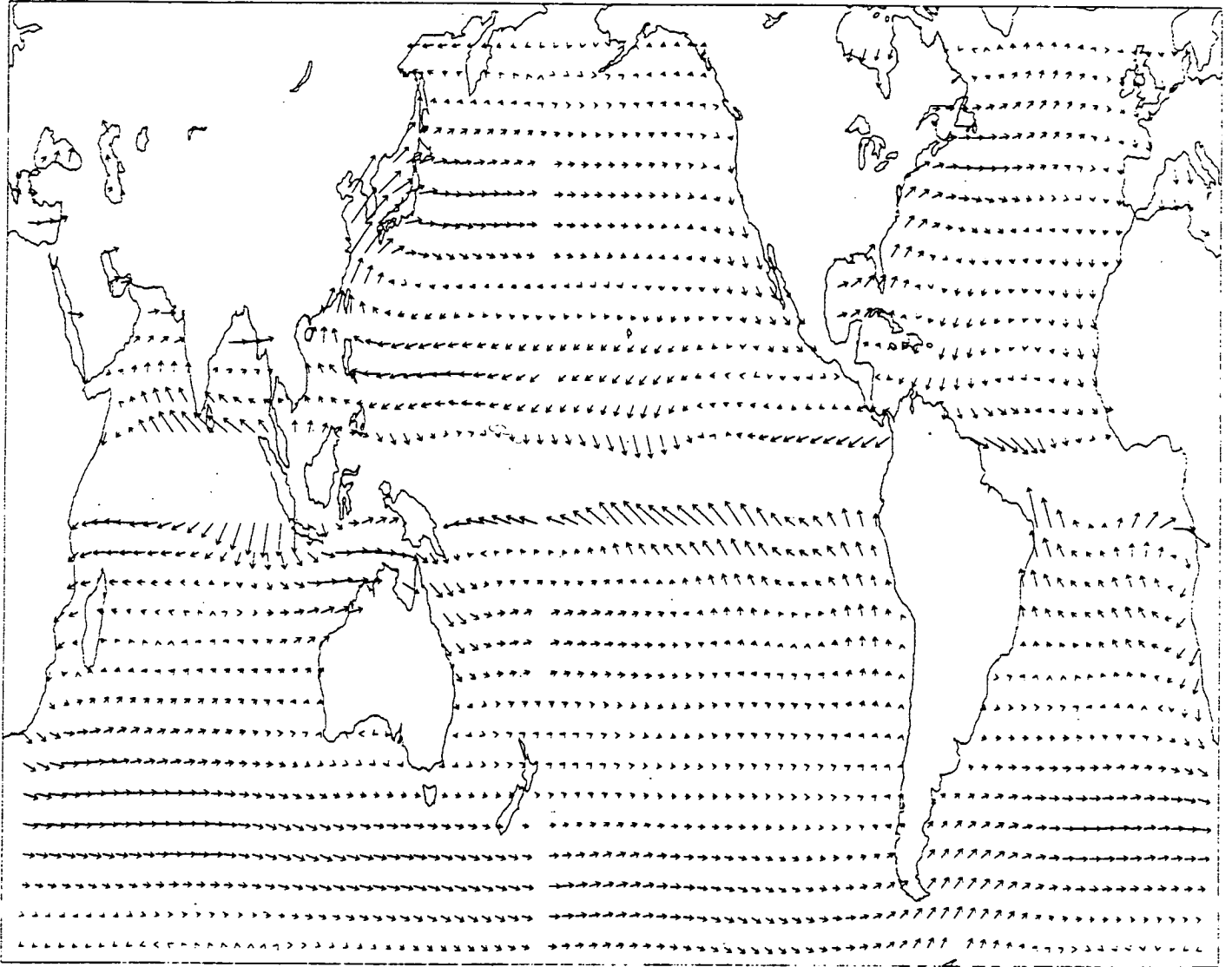


Figure 18. The geostrophic currents implied from $\bar{\eta}_{\rho\alpha nm}$.

The PGS-3337 error covariance matrix was calibrated for its gravitational model uncertainty (Lerch *et al.*, 1988). This matrix was also used to evaluate the uncertainties in $\bar{\eta}_A$. Figure 19 shows the covariance estimate of the geographical errors in $\bar{\eta}_A$ for the correlated coefficients. Note, where altimetry is not used, the estimated uncertainty in $\bar{\eta}_A$ reaches 64 cm, which is the expected global power for $\bar{\eta}_A$. This error magnitude is not exceeded, even in central Asia.

To highlight the error structure of $\bar{\eta}_A$, Figure 20 shows the standard deviations in $\bar{\eta}_A$ over the oceans. Very little structure is discernable in this estimate of the QSST errors. This suggests that our determination has achieved a high level of harmonic discrimination (*i.e.*, orthogonality) over the ocean regions, with very uniform overall resolution of $\bar{\eta}$.

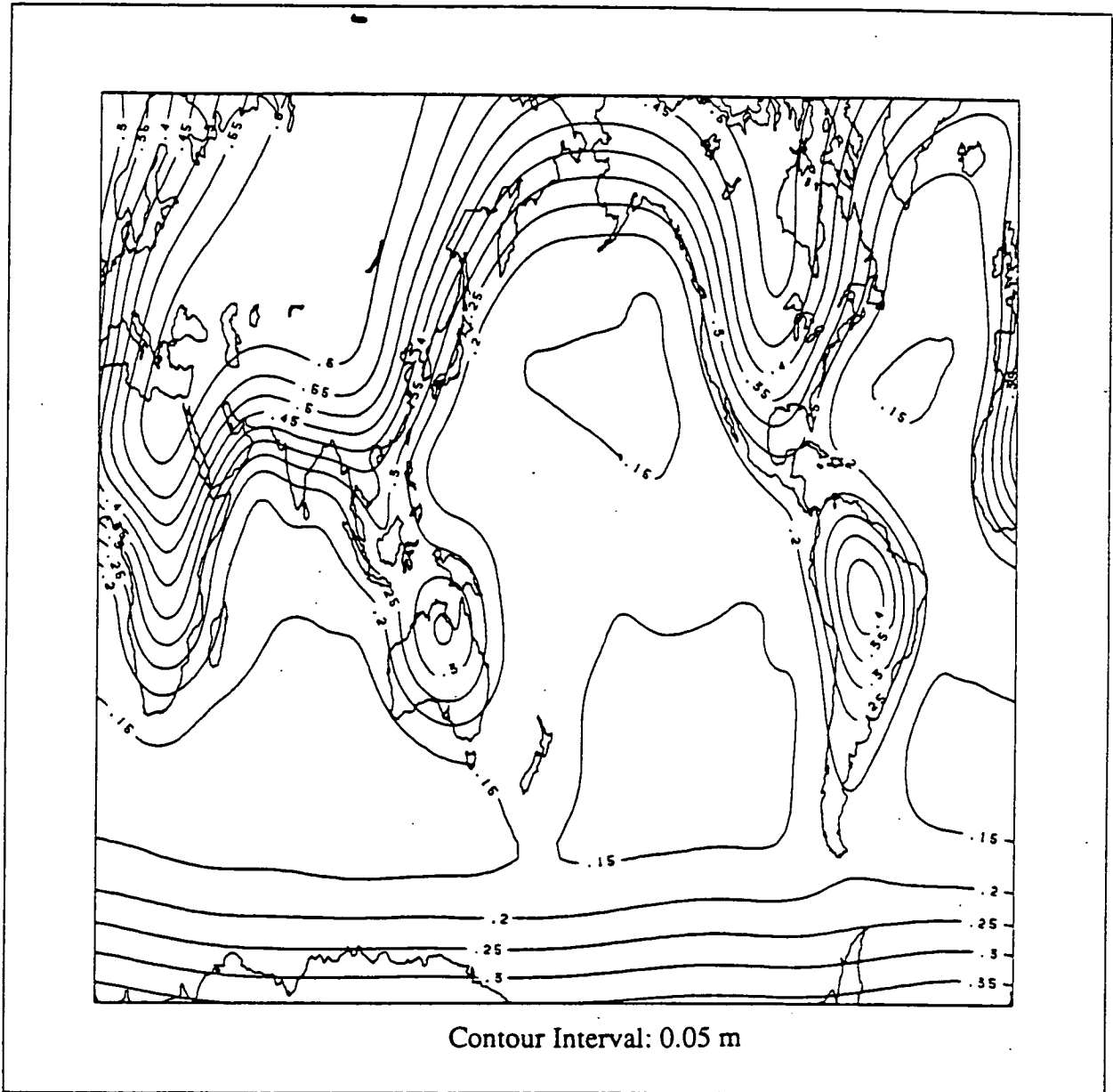
The 12 to 15 cm uncertainty obtained for $\bar{\eta}_A$ is consistent with the 10 cm error obtained for the geoidal errors at the same spatial wavenumbers (Figure 12b) with an additional contribution of altimeter data noise. We used ± 3.1 m per observation for the altimeter noise in PGS-3337. This value far exceeds the true noise in the SEASAT instrument, but it passed our calibration tests. This level of downweighting of the altimeter data is an effective strategy because the noise contribution is small compared to the geoidal reference uncertainty. This ensures very little aliasing of the geoid from non-gravity signals at the longest wavelengths within the satellite gravitational fields. The separation of oceanographic and geopotential signals is discussed in greater detail within the next section. Although the error for $\bar{\eta}_A$ is similar in magnitude to those shown for the h_N , there is little resemblance between the highly zonal characteristic of the geoid error compared to the flat uncertainty seen for $\bar{\eta}_A$ (Figure 12b).

5.5 Separation of Ocean and Gravity Signals

The separation of the oceanographic and gravitational signal within solutions containing satellite altimeter ranging data is of critical concern. Using altimeter data directly in gravity model solutions has been controversial, largely because many fear losing valid oceanographic information through subtle aliasing of the gravity coefficients. These fears are based on both the relative size of the $\bar{\eta}$ and h_N signals and the desire to keep the gravitational and dynamic height modeling problems separate by relying on geoidal models free of any direct altimetric data use. Altimeter crossover measurements, which eliminate stationary non-geoidal and geoidal signals, would seem to be a more acceptable compromise as a means of using altimetry in the gravity solutions. The crossover technique can be advanced for missions with highly controlled satellite repeating groundtracks to include data from each collinear pass.

Unfortunately, essential and otherwise recoverable geographic information is lost through the crossover differencing. This includes monitoring the geographically correlated orbital errors and especially in mapping the intermediate and short wavelength geoidal features over the ocean surface. It is our general view that the geoidal and oceanographic signals can be effectively separated through the proper solution design and parameterization. The direct use of altimetry as a set of range measurements to a surface that is properly characterized within the least squares process is the preferable method. This approach, demonstrated herein, uses the strongest gravitational signal and is the most direct means of obtaining improved models of h_N and $\bar{\eta}_A$. It is a strong, geographically uniform means of monitoring the satellite's radial evolution, without loss of sensitivity to all

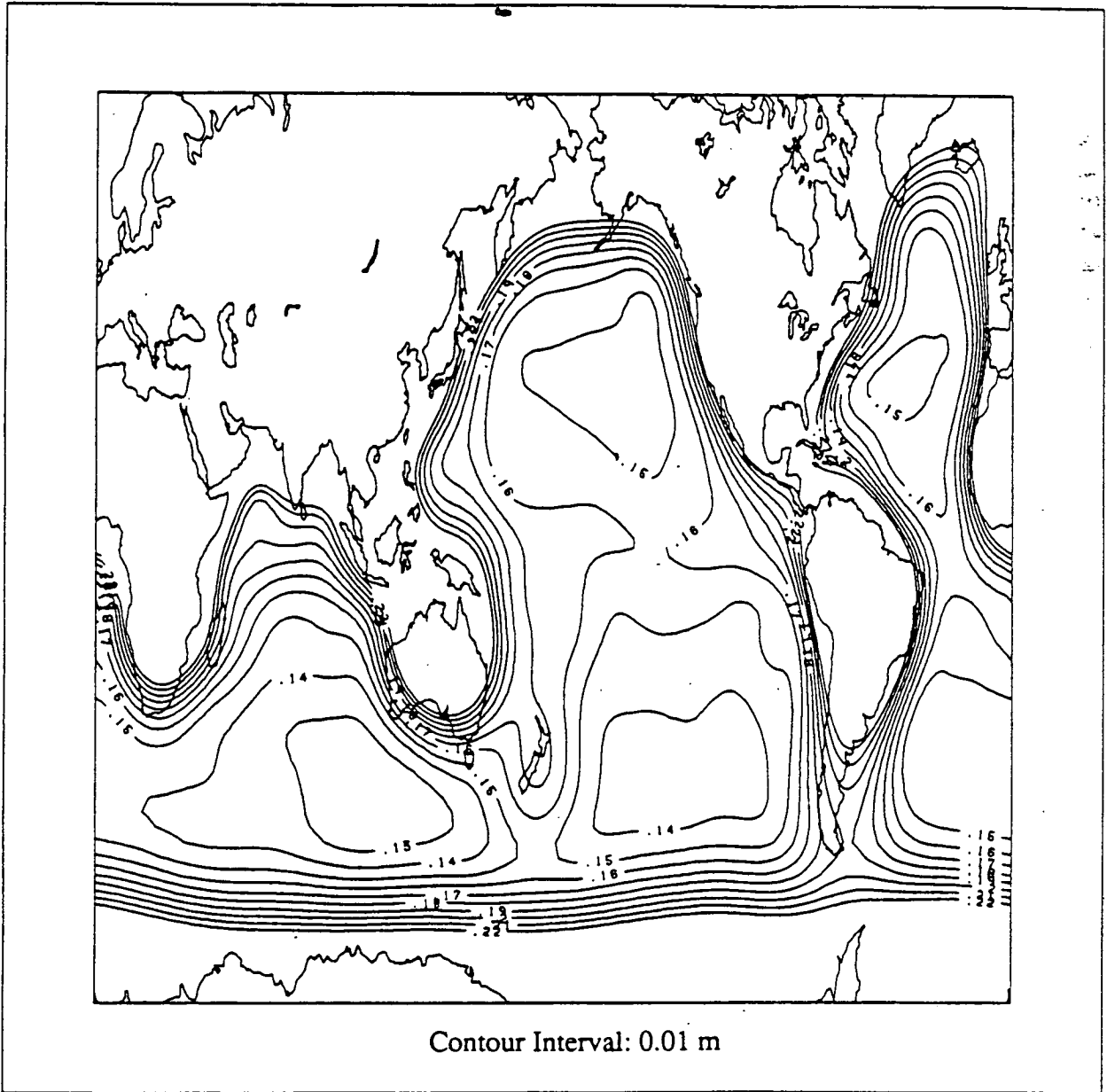
QSST Standard Deviations from PGS-3337 Model



NASA/GSFC 881128

Figure 19. The covariance estimate of the geographical PGS-3337 QSST errors for the correlated $\bar{\eta}_{A \cos m}$ using a contour interval of 5 cm.

Detailed Oceanic QSST
Standard Deviations from
PGS-3337 Model



NASA/GSFC 881128

Figure 20. PGS-3337 QSST error, where only the ocean area is presented and a 1.0 cm contouring interval is used.

geographically correlated orbit errors.

This section discusses the separation of these signals in our analysis. It includes results based on the solution covariances, calibration tests and comparisons between the PGS-3337 model and gravitational solutions where $\bar{\eta}$ is not represented, as well as other approaches that have been evaluated to assess the level of aliasing in the gravitational solution with the use of direct altimetry. This estimation strategy is shown to separate these signals well.

The calibration discussion involves comparison with alternative solutions PGS-3325 and PGS-3339. As described earlier, PGS-3325 was a gravitational model containing all the data used in PGS-3337 but was solved completely to degree and order 36. Like PGS-3337, PGS-3325 also solved for $\bar{\eta}_{A_{ann}}$ complete to degree and order 10. This model is particularly useful for calibration purposes, for it is the same size as that of GEM-T1 which is a satellite only model lacking any contribution of satellite altimetry and surface gravimetry.

PGS-3339, like PGS-3325, was solved completely to degree and order 36 from the same data set. However, PGS-3339 employed no model of $\bar{\eta}$ in the altimetry nor was $\bar{\eta}_A$ solved in this solution. The solution statistics from PGS-3339 reflect a situation (unfortunately unobtainable in reality) in which the altimetry had been perfectly corrected for the $\bar{\eta}$, and the resulting altimeter signal was ascribable to that of the geoid.

The aliasing effect in PGS-3325 versus PGS-3337, as measured by the earlier calibration tests with GEM-T1 plus surface gravity data, indicated that the low weighting for the altimeter data in PGS-3337 produced conservative error estimates. Hence, possibly by implication, we have conservative errors for the QSST signal in PGS-3337. It will be shown that our downweighting of the altimetry within all of these solutions enabled even PGS-3339 to recover a reasonably unaliased gravitational model.

Aliasing within a gravitational model can be assessed by using the method developed by Lerch (1985) and expanded upon in Lerch *et al.*(1988). These papers show that for gravitational solutions F and \hat{F} , where the data in \hat{F} is wholly contained with F , the expected deviation of the coefficients between the models is

$$e_{lm}^2 = \hat{\sigma}_{lm}^2 - \sigma_{lm}^2 \quad (32)$$

where, $\hat{\sigma}$ and σ are the estimated coefficient errors obtained from the covariances of fields \hat{F} and F , respectively.

The actual coefficient differences between the models (ΔC_{lm}) can be compared to this expected value, and a sample calibration factor per coefficient obtained as

$$k_{lm} = \left[\frac{\Delta C_{lm}}{e_{lm}} \right] \quad (33)$$

Both PGS-3325 and PGS-3339 have been calibrated with GEM-T1 to assess the level of aliasing arising from $\bar{\eta}$. The calibration factors so obtained are compared as histograms in Figure 21. As expected, PGS-3339 does exhibit higher calibration factors than does PGS-3325, although the difference, because of the low weight given to altimetry in our solutions, is not large.

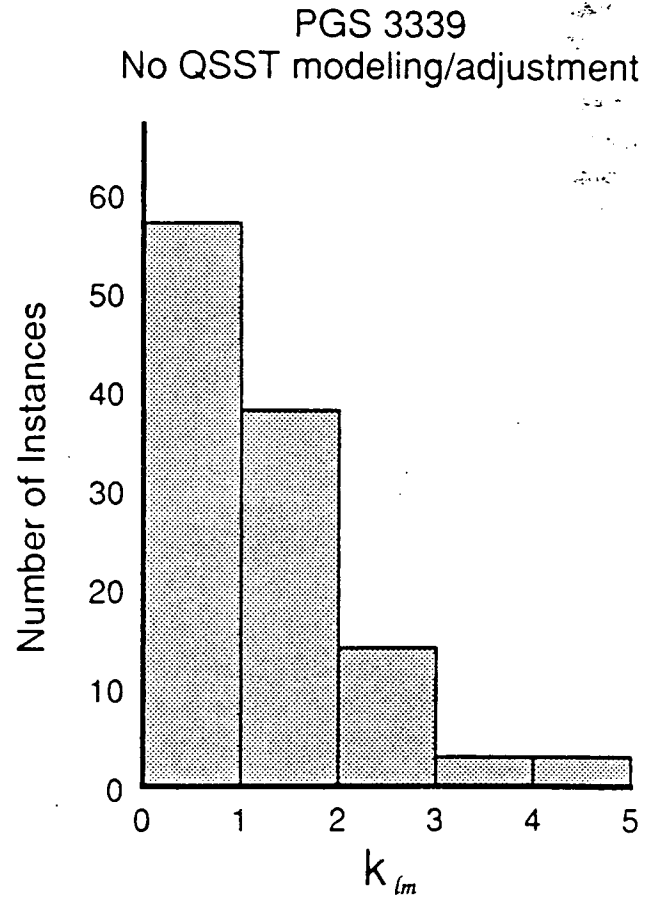
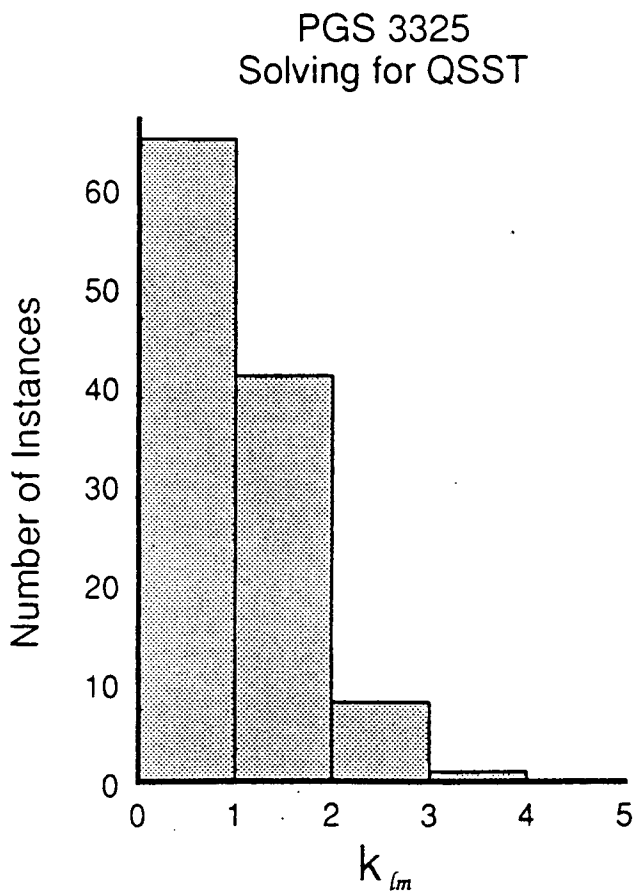


Figure 21. Histogram of the calibration factors k_{lm} for the combination gravity fields containing altimetry and surface gravimetry (PGS-3325 and PGS-3339).

Another good means for measuring the influence of the additional adjustment for QSST parameters on the gravitational solution is through evaluating the “condition numbers” of the respective harmonics when models with and without these parameters are compared. Here, the condition number C_i , first introduced into the GEM-1 model (Lerch *et al.*, 1972), is defined as

$$C_i = D_{ii}\sigma_{ii} \quad (34)$$

where D_{ii} is the diagonal of the normal matrix given in Equation (24) and σ_{ii} is the diagonal of the inverse of the normal matrix given in Equation (25).

It is shown in Marsh *et al.*(1987; Section 10.4) that the condition number reflects the loss of significant digits on the solution parameters in the reduction of the matrix. The condition number will increase from unity depending on the extent of correlation in the inverse matrix and according to Equation (34) σ_{ii} will increase as

$$\sigma_{ii} = \frac{C_i}{D_{ii}} = C_i\sigma_{ii}^{(0)} \quad (35)$$

where $\sigma_{ii}^{(0)}$ is the idealized error variance when no correlation is present. Thus

$$\sigma_{ii}^{(0)} = \frac{1}{D_{ii}} \quad (36)$$

If the C_i are significantly reduced in a solution, then the error variances and/or correlation are likewise reduced. In the case of PGS-3325 versus PGS-3339, the D_{ii} elements for the gravitational harmonics are identical. However, the earlier solution contains QSST parameters represented in a spherical harmonic form, and some correlation is known to exist between $\bar{\eta}_A$ and the gravitational terms. Therefore, the overall level of correlation between gravity and QSST parameters can be estimated from the ratio of the C_i (denoted C_{ri}) between these fields. The C_{ri} for the gravitational terms is

$$C_{ri} = \frac{C_{i3339}}{C_{i3325}} \quad (37)$$

This ratio provides some objective measure of the total influence that $\bar{\eta}_A$ has on the correlations and variances of the PGS-3325 gravitational solution.

Figure 22 presents the C_{ri} for the complete 36×36 gravitational solutions. Since the exponent (log) of the condition number roughly corresponds to the number of significant digits lost because of correlation in the solution, Figure 22 indicates that correlation within PGS-3325 is only a minor additional problem over PGS-3339. This result is expected because the largest magnitude for the correlation between gravitational harmonics and $\bar{\eta}_{A_{\alpha nm}}$ did not exceed 0.35.

The good separation of signals can be further demonstrated in Figure 23, in which the reduction of the error variances of PGS-3339 over PGS-3325 are presented. The adjustment of the QSST parameters caused a increase in the error variances of approximately 25%. The effect on the rms of the coefficient errors by degree in the PGS-3325 versus PGS-3339 solutions is shown in Figure 24. Quite clearly, the estimation of $\bar{\eta}_{A_{\alpha nm}}$ has not greatly reduced the accuracy of the long wavelength gravity model recovery, nor has it significantly changed the internal correlations of the geopotential solution. This confirms the validity of this solution strategy and indicates well separated signals.

RMS OF COEFFICIENT ERROR PER DEGREE

ERROR X 10⁹

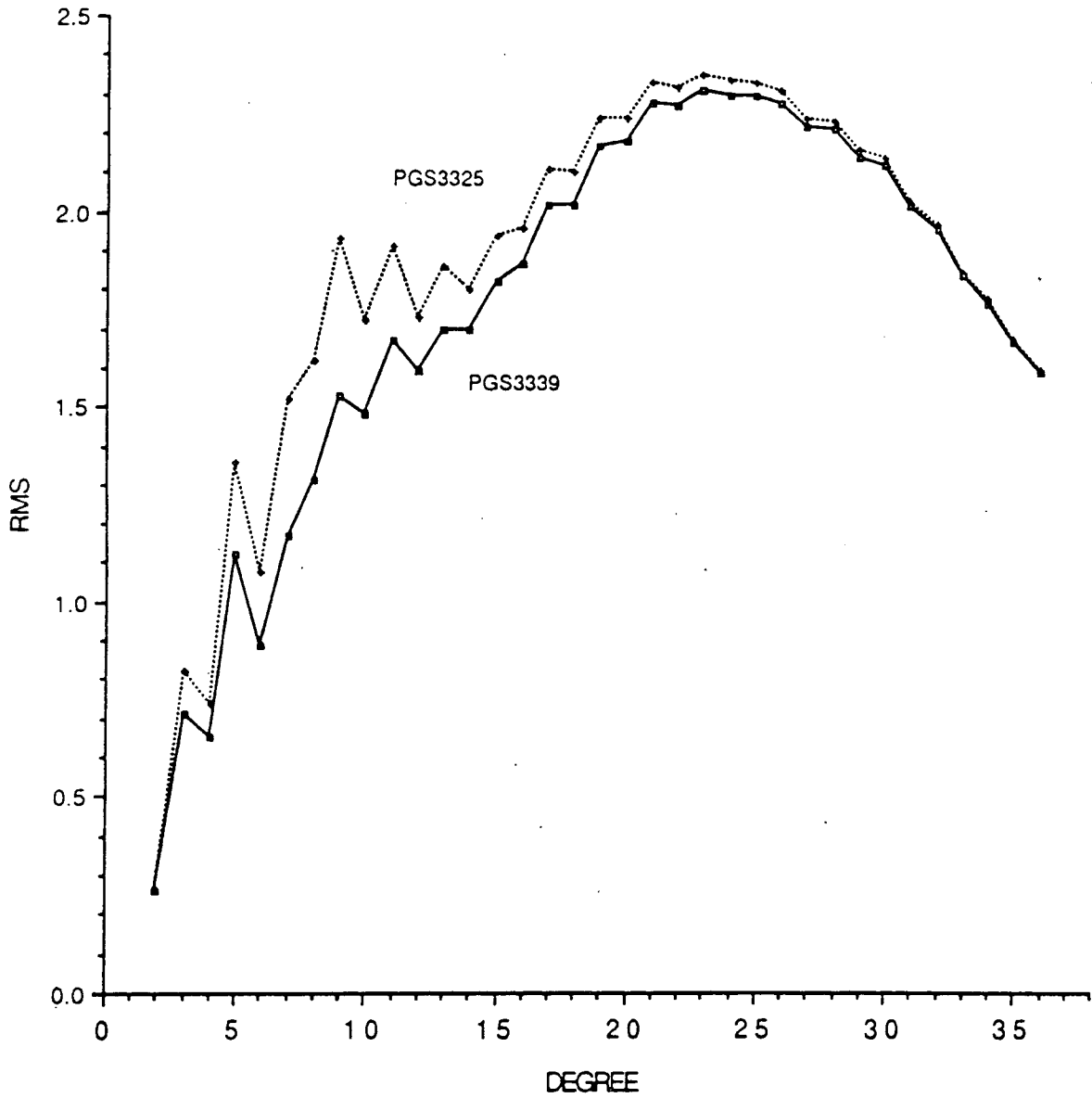


Figure 24. The effect on the rms coefficient errors by degree in the PGS-3325 versus PGS-3339 solutions.

5.6 Correlation Between Gravity and QSST Solutions

The PGS-3337 covariance matrix has been used to map the parametric correlation coefficient between the gravitational and QSST parts of the solution. The geographic errors from the gravity, $\bar{\eta}_A$ and combination of parameters have been calculated with use of the variance of the sum of two variables (e.g., Y_1, Y_2), which is

$$\sigma_{Y_1+Y_2}^2 = \sigma_{Y_1}^2 + \sigma_{Y_2}^2 + 2r_{12}\sigma_{Y_1}\sigma_{Y_2} \quad (38)$$

From these three error estimates, the correlation coefficient (r_{12}) has been calculated globally. This mapping indicates that over the ocean surface where SEASAT data are present, the areal correlation coefficient does not exceed -0.2 as shown in Figure 25 and Plate 3. A good separation of $\bar{\eta}$ and h_N signals is indicated.

The low level of correlation seen in Figure 25 compared to a much larger correlation found in Tapley *et al.* (1988) reflects the lower weight given to altimetry within our analysis. As a consequence, the dynamic information in the laser tracking data defines the long wavelength geoid, and the altimetry makes its largest contribution in the definition of the higher degree terms.

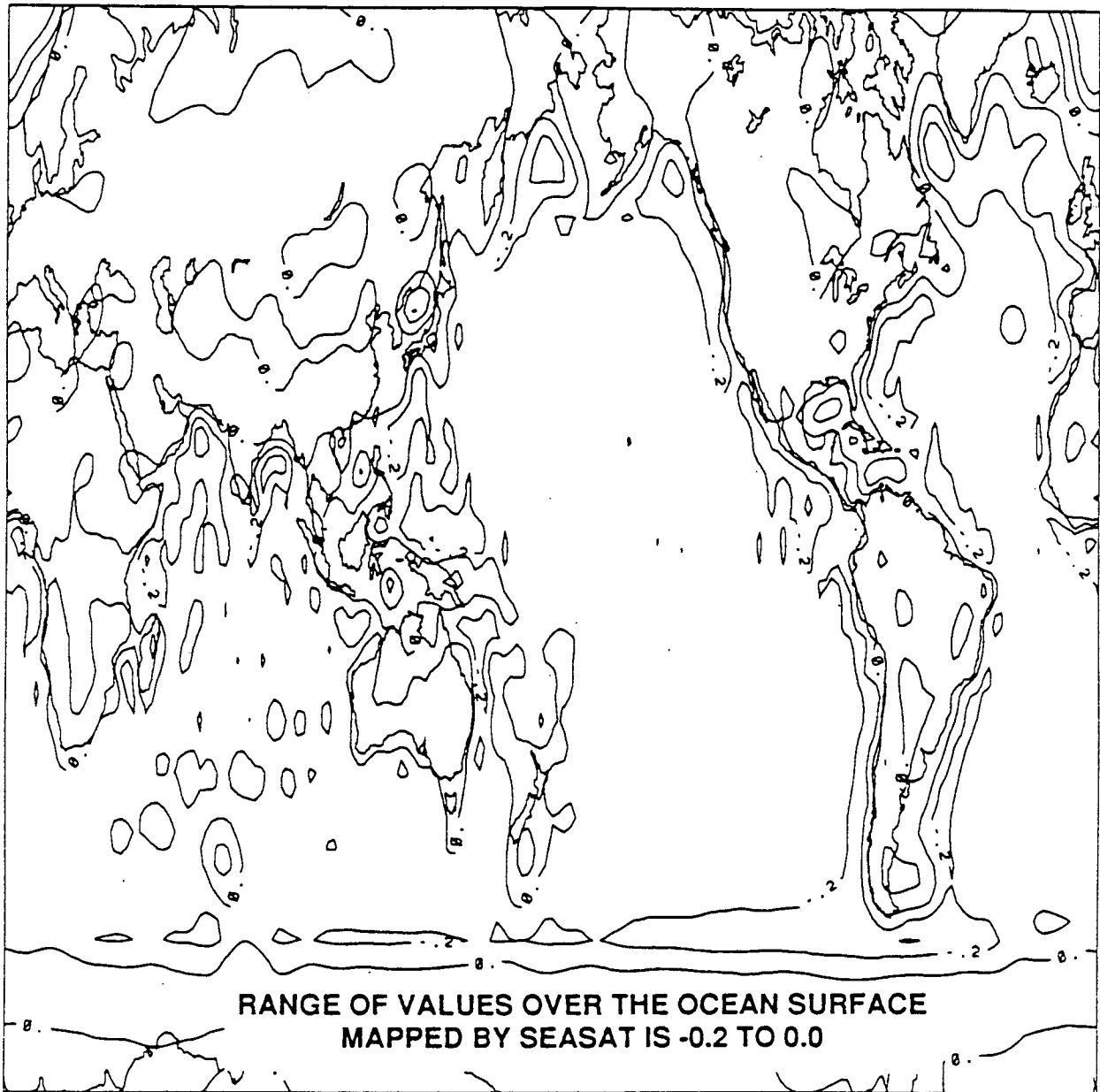
The improved definition of the higher degree terms within the gravitational model reduces leakage into the low-degree geoid, so somewhat indirectly, the long wavelength geoid is also improved. To achieve this balance, the altimetry requires only modest weight in the solution. However, by inference, if the altimeter data is substantially up-weighted, separation of the QSST and geoidal signals is degraded.

5.7 Importance of Signal Constraints

Finally, returning to Figure 13, one sees another important consequence of the solution strategy which has been used. Beyond the point in the solution where the estimated geoid errors overtake the *a priori* estimate of the power in $\bar{\eta}_{A_{annm}}$ (which for PGS-3337 is approximately degree 8), the signal constraints drive the adjusted $\bar{\eta}_{A_{annm}}$ toward zero. This is clearly seen in Figure 13 where the estimates of $\bar{\eta}_{A_{annm}}$ above degree 8 have much less power than that expected from the Levitus power law (as described in Figure 2). Thereby, the geoidal error does not significantly alias the oceanographic signal at these degrees, because the adjusting QSST coefficients are nearly zero.

This behavior can be explained by the presence of two power laws, one for the gravitational terms and one for $\bar{\eta}_{A_{annm}}$. Both laws favor zero for the adjusted coefficients, but the gravitational rule permits a much larger adjustment away from zero than does the QSST power law to yield the same weighted residual. Consequently, if there is a surface signal tracked by the altimeter, and the dynamic sensitivity to this effect on the collection of satellite orbits is weak, this signal can be attributed to either the geometric shape of the geoid or to the shape of the dynamic topographic surface when satisfying the altimeter observation equation. However, at degree 8, the expected size of $\bar{\eta}_{A_{annm}}$ is less than 3 cm from our evaluation of $\bar{\eta}_\rho$, whereas our modified Kaula's rule expects a geoidal signal of over 65 cm from the same degree and order harmonic. The least squares constraint comes strongly into play because this signal can be accommodated by either the h_N or the $\bar{\eta}_A$ harmonics to yield the same altimeter range residual.

PGS 3337 QSST AND GEOID CORRELATION



CONTOUR INTERVAL: 0.2

Figure 25. The correlation between $\bar{\eta}_\rho$ and $h_{N_{ref}}$ from PGS-3337.

The signal constraint introduces a set of observation equations specifying zero for all QSST and gravity terms with a standard deviation equal to the expected power of the respective terms. The solution favors a geoidal adjustment in its minimization of the observation residuals because a small departure of the geoid from zero gives rise to a much smaller "residual" when compared to its expected power versus a comparable adjustment to the QSST terms. Consequently, the possibility of geoid error leaking into dynamic topographic information is minimized, and $\bar{\eta}_{A_{ann}}$ yields virtually no power (*i.e.*, very small adjusted values for the QSST coefficients) when the h_N error overtakes the expected power of $\bar{\eta}_A$ for any harmonic term.

6 Gravity Model Performance

Orbital accuracies are a central concern of satellite altimetry and motivate the development of improved gravitational fields. A relevant method of assessing the performance of PGS-3337 is through tests using satellite tracking data. In light of the concern focused herein on the proper separation of gravitational and oceanographic signals (*i.e.*, given our use of satellite altimeter ranging in forming the gravitational model itself), it is hoped that such tests can examine the degree of aliasing present in the resulting field.

Satellite tracking data have been the major resource for deducing the long wavelength geopotential. The observed motion of a near-Earth satellite yields a largely unambiguous measure of the inhomogeneous gravitational attraction being exerted on a vehicle as it passes through the potential field. The dominant contribution to this perturbed motion comes from the longest spatial wavelength part of the geopotential (to degree 10), which is also the part of the model that has the same spatial dimensions as $\bar{\eta}$. However, unlike h_N , $\bar{\eta}$ gives rise to no discernable dynamic perturbation on a satellite's orbit. Therefore, while aliasing of the gravity field is possible through the direct utilization of satellite altimetry, gravity models so aliased would be expected to show diminished performance when tested on independent satellite orbital tracking.

6.1 Orbital Tests Using Independent Laser/Doppler Observations

The deployment of a worldwide network of laser stations has greatly improved the capabilities of satellite geodesy. Much of the progress attributable to recent GSFC gravitational models is a result of the superior accuracy now available from these tracking systems. While GEM-T1 made use of a large laser data subset, a lot of data has not been used in this solution.

The Ajisai satellite, launched by the Japanese in 1986, is equipped with laser retroreflectors. These data were not utilized in GEM-T1, although they will be incorporated in future models. Ajisai orbits in a nearly circular orbit at an altitude of 1500 km and inclination of 50.015°. Table 8 presents a comparison of the rms of fit to a global set of Ajisai laser data obtained using both GEM-T1 and PGS-3337. The results show that PGS-3337 performs in a superior fashion when tested with these data, a result which has been confirmed on many additional test arcs. There is very little evidence of aliasing in the PGS-3337 solution.

The NOVA Doppler satellite is in a polar orbit. It benefits from a drag-compensation system making it quite valuable for gravity field modeling. These data, like those of Ajisai, have not been used in GEM-T1 but are being reduced for inclusion in GEM-T2. Again, when used to test the models, the fit to the NOVA Doppler data indicates that PGS-3337 is a slight improvement over GEM-T1.

Also shown in Table 8 are additional results on several other laser satellites. In every case, these data have not been utilized in either the GEM-T1 or PGS-3337 solutions. In the cases of GEOS-1 and GEOS-3, the data used for these test arcs are superior to the data that were used from these satellites in the gravitational solutions. The satellite laser tracking data sets used in GEM-T1/PGS-3337 for GEOS-3 came from the 1975-76 timeframe; those from GEOS-1 were from the 1977-

Table 8: Gravity Model Testing Using Orbital Tracking Observations

Satellite	Arc Length <i>Days/Data type</i>	Rms of Fit	
		GEM-T1	PGS-3337
Ajisai	5/Laser	18.1 cm	17.1 cm
NOVA	6/Doppler	0.436 cm/s	0.402 cm/s
LAGEOS	30/Laser	6.9 cm	6.9 cm
Starlette	5/Laser	17.2 cm	15.1 cm
GEOS-1	5/Laser	38.7 cm	37.4 cm
GEOS-3	5/Laser	69.3 cm	42.5 cm

78 timeframe. The test arcs in Table 8 make use of data now available from 1980. It is important to note that: (a) all of the Smithsonian Astronomical Observatory laser systems were significantly upgraded in 1979 through the installation of pulse choppers and improved optics (These upgrades reduced the noise level in these systems by a factor of four); and (b) the third generation NASA mobile laser systems were first deployed in the fall of 1979. As shown in Table 8, PGS-3337 again has a superior performance on GEOS-1 and especially GEOS-3 when tested against these new data. While the GEOS-3 result is dramatic, it is also significantly affected by a high order orbital resonance which is now modeled in PGS-3337 with the extension of the model to degree and order 50.

Also of primary interest are two special laser satellites: LAGEOS and Starlette. By careful design, these satellites have a limited sensitivity to nonconservative forces and are therefore prime objects for gauging gravity modeling accuracies. These orbits, as described earlier in Table 4, are quite different. LAGEOS orbits the Earth in a circular fashion at an altitude of nearly an Earth's radius and thereby senses only the longest-wavelength portion of the gravity field. Starlette, on the other hand, is in a somewhat eccentric orbit with a perigee height of slightly more than 800 km. In this orbit, Starlette experiences a rich spectrum of gravitational effects. In GEM-T1/PGS-3337, the Starlette and LAGEOS data sets were restricted to observations acquired before 1985. The test arcs utilized here contain global laser data taken in 1986. Again, PGS-3337 performs in a superior or equal fashion compared to GEM-T1. On the basis of these results, the gravitational signal in the PGS-3337 model is uncontaminated by, and at all intermediate and shorter spatial wavelengths, vastly improved through the use of satellite altimeter and surface gravimetry data.

6.2 The Radial Accuracy of SEASAT

With SEASAT we have the ability to isolate the radial orbit modeling performance of different gravity fields through the use of altimeter data. This is accomplished by evaluating the difference in the altimeter measured sea surface height (h) at crossover locations. Since h is dominated by h_N , its value at a specific geographical location would be expected to be nearly time invariant. When h is measured by crossing altimeter passes, the difference in h is a reasonably strong measure of the nongeographically correlated error in h_{sat} . This assessment of h_{sat} error is incomplete, for there are correlated errors affecting both the ascending and descending orbits similarly. However,

Table 9: SEASAT Altimeter Crossover Analysis: Estimate of Nongeographically Correlated Radial Orbit Error From Recent GSFC Gravitational Models

Epoch (<i>yymmdd</i>)	Number of Crossovers	Doppler		Doppler/Altimetry
		GEM-T1 (<i>meters</i>)	PGS-3337 (<i>meters</i>)	PGS-3337 (<i>meters</i>)
780727	1234	0.932	0.691	0.336
780802	1299	0.688	0.439	0.249
780808	1407	0.695	0.422	0.283
780818	820	0.726	0.482	0.316
780917	1473	0.632	0.368	0.290
780923	1541	0.675	0.399	0.283
780929	1498	0.719	0.536	0.355
781005	939	0.697	0.421	0.333
Average ($\div\sqrt{2}$)		0.509	0.332	0.216

there remains a large time dependent radial orbit error signal which can be detected in these tests and further evaluated.

Table 9 compares the rms crossover misclosure found by using orbits computed with GEM-T1 and PGS-3337. In Marsh *et al.*(1988) it is shown that GEM-T1 was a significant improvement over all earlier gravitational fields for modeling h_{sat} on SEASAT. Table 9 compares orbits calculated solely from the TRANET Doppler range-rate tracking data acquired on SEASAT, as well as giving results using PGS-3337 when altimeter data is included in the orbital adjustment. Clearly, PGS-3337 is a major improvement over GEM-T1. Furthermore, the inclusion of the altimeter data drives the component of the radial error being measured to the 20 cm level.

At the 20-cm rms level, there are many other effects that do not properly cancel when forming the crossover difference. Tide errors and errors due to the mislocation of the mean sea level at times of high sea-state (*e.g.*, the EM bias) can make significant contributions to the crossover residuals. Figure 26 shows the geographical distribution of the crossover misclosures when using PGS-3337 and the Doppler/altimeter data sets. The largest crossover residuals are found in places like the Gulf of Alaska where large tidal errors are known to exist, and in the Southern Ocean where there is a high sea state. For example, during the SEASAT Mission time interval, for the region bounded by latitudes 50°S to 75°S and longitudes 330°E to 90°E (where Figure 25 reveals 28 and 27 cm rms crossover residuals) the average $W_{\frac{1}{3}}$ was in excess of 7 m (Chelton *et al.*, 1981). In this region in particular, the 20% uncertainty estimated by Douglas and Agreen (1983) for the EM bias correction yields a modeling error of more than 9 cm.

The altimeter residuals from the PGS-3337 reference orbits (computed using both the Doppler and altimeter data in the orbital reduction process) have been studied. Plate 4 shows a graphical presentation of these residuals binned within 5 degree blocks. The first image shows the number of altimeter observations utilized in the PGS-3337 solution present in each of the 5° blocks. The second, third, and fourth images on Plate 4 give various statistical quantities computed using the

Estimated Non-Geographically Correlated Radial Orbit Errors from SEASAT Altimeter Crossover Analysis (in cm)

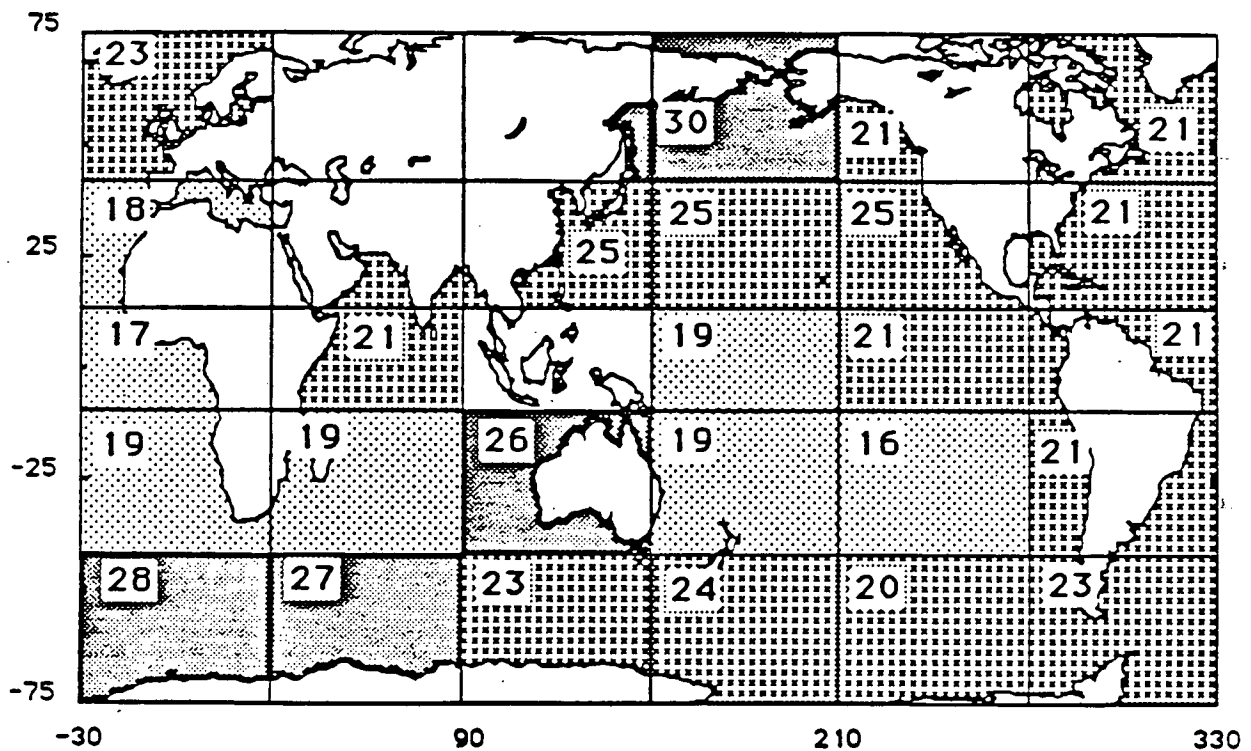


Figure 26. The geographical distribution of the crossover misclosures that result when using PGS-3337 and the Doppler/altimeter data sets.

data present in each block. The second image gives the rms of the residuals, the third shows the mean of the residuals, and the fourth presents the mean of the absolute values of the residuals.

One of the benefits of improved orbit definition is that oceanographic signals are detected by using altimeter ranging directly without requiring further empirical corrections to the orbital definition. This is the motivation for the 10 cm accuracy requirement for h_{sat} on TOPEX. Referring back to Plate 1, we can see that the correspondence between the rms of the altimeter residuals obtained herein and the estimates of $\langle \eta \rangle$ previously obtained using SEASAT data is good. Residual energy is also present when models of η_T are suspect. There are significant unmodeled effects where sea state is large. However, in regions where $W_{\frac{1}{3}}$ and $\langle \eta \rangle$ are small and η_T is well modeled, we find less than 15 cm rms in the altimeter residuals. This is the case in the eastern Pacific and the southern portion of the Indian Oceans. This confirms our estimate that approximately 15 cm accuracy is now being achieved for the modeling of h_{sat} on SEASAT when using PGS-3337 and the altimeter data within the orbital solution.

A comparison of the third and fourth images on Plate 4 gives a direct indication of the temporal averaging which occurs in the PGS-3337 solution. Although the mean of the altimeter residuals is small nearly everywhere, there is a significant amount of signal averaged. Most of this signal is attributable to $\langle \eta \rangle$. As expected, this signal has largely remained behind as an unmodeled effect when $\bar{\eta}_A$ is defined within the PGS-3337 solution. This suggests that we have produced a mean sea surface with respect to these temporally varying effects. In conclusion, it has been shown that a direct analysis of the altimeter residuals obtained from PGS-3337 yields a reliable estimate of altimeter sensed ocean processes without requiring further empirical orbit corrections.

The SEASAT orbits computed using GEM-T1 and PGS-3337 are available to those investigators seeking improved orbit accuracy.

7 Conclusions

A new geopotential model, PGS-3337, has been computed at GSFC that incorporates SEASAT satellite altimeter data as a dynamic observation of the satellite's height above the sea surface. This model, complete to degree and order 50, represents a major improvement in gravitational field modeling, especially at intermediate and shorter spatial wavenumbers.

Spherical harmonic coefficients representing the dynamic sea surface topography were recovered in a simultaneous solution with the gravitational coefficients. The solution for these dynamic topography terms has permitted altimetry to significantly improve the gravitational solution at all wavelengths while preventing aliasing from non-geoidal sources. The recovered dynamic topography maps clearly reveal the global basin-wide circulation of the oceans with a resolution of approximately 1500 km. The magnitudes and locations of the dynamic topography features are much closer to the observed ocean climatology than previous estimates made using satellite altimetry.

Satellite altimeter data processed in this manner have permitted a significant improvement in the gravitational modeling of the radial trajectory of altimeter satellites. SEASAT orbits, have improved dramatically in their radial component to the level of about 20 cm rms radial accuracy with the use of this new field. Furthermore, PGS-3337 improves the orbital accuracies of many laser and Doppler satellites. This model confirms improved long wavelength general gravity modeling. It supports a conclusion that the gravitational and oceanic signals have been effectively decoupled using this solution methodology.

8 Acknowledgements

The authors wish to thank Ken Rachlin, Neader Chandler, and Lena Braatz of ST Systems Corp. for their help with the altimeter data analysis. Barbara Putney of GSFC, Dave Rowlands of EG&G/WASC and Bill Eddy, also of ST Systems, Inc., provided excellent support for the introduction of the altimeter models into the GEODYN Program. Color graphics support were provided by Karen Settle of the General Science Corp. and Janet Ressler from the University of Maryland. We wish to acknowledge the valuable comments on a draft of this document provided by Steve Nerem from the Center for Space Research at the University of Texas, as well as Dick Brown and Theo Engelis of ST Systems Corp.

References

- Anonymous, SEASAT: Geophysical data record (GDR) users handbook(Altimeter), JPL Report 622-97, Rev A, September 1980.
- Born, G.H., P. Ailer, and A. Pino, Orbit analysis for the GEOSAT-ERM, *Journal of Astronautical Science*, 36, 425-446, 1988.
- Brammer, R.F., and R.V. Sailor, Preliminary estimates of the resolution capability of the SEASAT radar altimeter, *Geophysical Research Letters*, 7, 193-196, 1980.
- Brown, W., W. Munk, F. Snodgrass, B. Zetler, and H. Mofjeld, MODE bottom pressure experiment, *Journal of Physical Oceanography*, 5,, 75-85, 1975.
- Chelton, D.B., WOCE/NASA Altimeter Algorithm Workshop, *U.S. WOCE Technical Report No. 2*, 70pp, U.S. Planning Office for the World Ocean Circulation Experiment (WOCE), College Station, Texas, 1988.
- Chelton, D.B., K.J. Hussey, and M.E. Parke, Global satellite measurements of water vapor, wind speed, and wave height, *Nature*, 294, 529-532, 1981.
- Cheney, R.E., and J.G. Marsh, Global ocean circulation from satellite altimetry, *EOS*, 63, 997, 1982.
- Cheney, R.E., J.G. Marsh, and B.D. Beckley, Global mesoscale variability from collinear tracks of SEASAT altimeter data, *Journal of Geophysical Research*, 88, 4343-4354, 1983.
- Christodoulidis, D.C., D.E. Smith, R.G. Williamson, and S.M. Klosko, Observed tidal braking in the Earth/Moon/Sun system, *Journal of Geophysical Research*, 93, 6216-6236, 1988.
- Christodoulidis, D.C., R. Williamson, D. Chinn and R. Estes, On the prediction of ocean tides for minor constituents, in *Proceedings of the Tenth International Symposium on Earth Tides*, edited by R. Vieira, p. 659, Consejo Superior de Investigaciones Cientificas, Madrid, 1986.
- Colombo, O.L., Altimetry, orbits and tides, NASA TM-86180, Goddard Space Flight Center, Greenbelt, Md., 1984.
- Douglas, B.C. and R. W. Agreen, The sea state correction for GEOS-3 and SEASAT satellite altimeter data, *Journal of Geophysical Research*, 88, 1655-1663, 1983.
- Engelis, T., Global circulation from SEASAT altimeter data, *Marine Geodesy*, 9, 1, 1985.
- Engelis, T., Spherical harmonic expansion of Levitus sea surface topography, *The Ohio State University Department of Geodetic Science and Surveying, Report No. 385*, Columbus, 1987.
- Engelis, T., On the simultaneous improvement of a satellite orbit and determination of sea surface topography using altimeter data, *Manuscripta Geodaetica*, 13, 180-190, 1988.
- Engelis, T., and P. Knudsen, Orbit improvement and determination of the ocean geoid and topography from 17 days of SEASAT data, *Manuscripta Geodaetica*, in press, 1989.

- Fu, L.L. and D.B. Chelton, Temporal variability of the Antarctic circumpolar current observed from satellite altimetry, *Science*, 226, 343-346, 1984.
- Gilbert, F., and A.M. Dziewonski, An Application of normal mode theory to the retrieval of structural parameters and source mechanisms from seismic spectra, *Philosophical Transactions of the Royal Society of London*, 278A, 187-269, 1975.
- Gill, A.E., and P.P. Niiler, The theory of seasonal variability in the ocean, *Deep-Sea Research*, 20, 141-177, 1973.
- Hallock, Z.R., J.L. Mitchell, and J.D. Thompson, Sea surface topographic variability near the New England Seamounts Chain: An intercomparison among *in situ* observations, numerical simulations and GEOSAT altimetry, from the Regional Energetics Experiment, *Journal of Geophysical Research*, in press, 1989.
- Kaula, W., *Theory of Satellite Geodesy*, Blaisdell, Waltham, Massachusetts, 1966
- Koblinsky, C.J., Observations of the global annual cycle of sea level from the GEOSAT altimeter, *EOS*, 69, 1268, 1988.
- Kolenkiewicz, R. and C.F. Martin, SEASAT height calibration, *Journal of Geophysical Research*, 87, 3189-3199, 1982.
- Lerch, F.J., C.A. Wagner, D.E. Smith, M. Sandson, J. Brown, and J. Richardson, Gravitational fields for the Earth (GEM 1 and 2), NASA TM 65970, Goddard Space Flight Center, Greenbelt, Maryland, 1972
- Lerch, F.J., S.M. Klosko, R.E. Laubscher, and C.A. Wagner, Gravity model improvement using GEOS-3 (GEM 9 and 10), GSFC Document X-921-77-246, Goddard Space Flight Center, Greenbelt, Maryland, 1977.
- Lerch, F.J., S.M. Klosko, and G.B. Patel, Gravity model development from LAGEOS, *Geophysical Research Letters*, 87, 1263-1266, 1982a.
- Lerch, F.J., J.G. Marsh, S.M. Klosko, and R.G. Williamson, Gravity improvement for SEASAT, *Journal of Geophysical Research*, 87, 3281-3296, 1982b
- Lerch, F.J., Error spectrum of Goddard satellite models for the gravity field, NASA TM 86223, Goddard Space Flight Center, Greenbelt, Maryland, 1985.
- Lerch, F.J., S.M. Klosko, C.A. Wagner, and G.B. Patel, On the accuracy of recent Goddard gravity models, *Journal of Geophysical Research*, 90, 9312-9334, 1985.
- Lerch, F.J., J.G. Marsh, S.M. Klosko, E.C. Pavlis, G.B. Patel, D.S. Chinn and C.A. Wagner, An improved error assessment for the GEM-T1 gravitational model, NASA TM in press, Goddard Space Flight Center, Greenbelt, Maryland, 1988.
- Levitus, S., Climatological atlas of the world ocean. NOAA Professional Paper 13, 173pp, 1982.
- Lisitzin, E., *Sea Level Changes*, Elsevier, Amsterdam, 1974.

- Lorell, J., E. Colquitt, and R.J. Anderle, Ionospheric correction for SEASAT altimeter height measurements, *Journal of Geophysical Research*, 87, 3207-3212, 1982.
- Marsh, J.G., R.E. Cheney, T.V. Martin, and J.J. McCarthy, Computation of a precise mean sea surface in the eastern North Pacific using SEASAT altimetry, *EOS*, 63, 178-179, 1982.
- Marsh, J.G., F.J. Lerch, B.H. Putney, D.C. Christodoulidis, D.E. Smith, T.L. Felsentreger, B.V. Sanchez, S.M. Klosko, E.C. Pavlis, T.V. Martin, J.W. Robbins, R.G. Williamson, O.L. Colombo, D.D. Rowlands, W.F. Eddy, N.L. Chandler, K.E. Rachlin, G.B. Patel, S. Bhati, and D.S. Chinn, An improved model of the Earth's gravitational field: GEM-T1, NASA TM-4019, Goddard Space Flight Center, Greenbelt, Maryland, 1987.
- Marsh, J.G., F.J. Lerch, B.H. Putney, D.C. Christodoulidis, D.E. Smith, T.L. Felsentreger, B.V. Sanchez, S.M. Klosko, E.C. Pavlis, T.V. Martin, J.W. Robbins, R.G. Williamson, O.L. Colombo, D.D. Rowlands, W.F. Eddy, N.L. Chandler, K.E. Rachlin, G.B. Patel, S. Bhati, and D.S. Chinn, A new gravitational model for the Earth from satellite tracking data: GEM-T1, *Journal of Geophysical Research*, 93, 6169-6215, 1988.
- Martin, T.V., W.F. Eddy, D.D. Rowlands, and D.E. Pavlis, GEODYN System Description, *E.G.&G. Contractor Report*, E.G.&G./WASC, Lanham, Maryland, 1985.
- Mather, R.S., F.J. Lerch, C. Rizos, E.G. Masters and B. Hirsch, Determination of some dominant parameters of the global dynamic sea surface topography from GEOS-3 altimetry, NASA TM-79558, Goddard Space Flight Center, Greenbelt, Maryland, 1978.
- Melbourne, W. *et al.*, Project MERIT standards, USNO Circular, no. 167, 1983.
- Moritz, H., *Advanced Physical Geodesy*, Abacus, Tunbridge Wells Kent, Kent, England, 1980.
- Parke, M.E., O_1, P_1, N_2 Models of the global ocean tide on an elastic Earth plus surface potential and spherical harmonic decompositions for M_2, S_2 , and K_1 , *Marine Geodesy*, 6, 35-81, 1982.
- Pavlis, N.K., Modeling and estimation of a low degree geopotential model from terrestrial gravity data, *The Ohio State University Department of Geodetic Science and Surveying, Report No. 386*, Columbus, 1988.
- Rapp, R., A global atlas of sea surface heights based on the adjusted SEASAT altimeter data, *The Ohio State University Department of Geodetic Science and Surveying, Report No. 333*, Columbus, 1982.
- Rapp, R., Report of special study group No. 5.39 of IAG: Fundamental geodetic constants, *XVIII General Assembly of the IUGG*, Hamburg, Federal Republic of Germany, 1983a.
- Rapp, R., Tidal gravity computations based on recommendations of the Standard Earth Tide Committee, *XVIII General Assembly of IUGG*, Hamburg, Federal Republic of Germany, 1983b.
- Rapp, R., Detailed gravity anomalies and sea surface heights derived from GEOS-3/SEASAT altimeter data, *The Ohio State University Department of Geodetic Science and Surveying, Report No. 365*, Columbus, 1985.

- Rapp, R., An estimate of equatorial gravity from terrestrial and satellite data, *Geophysical Research Letters*, 14, 730-732, 1987.
- Rapp, R.H. and J.Y. Cruz, Spherical harmonic expansion of the Earth's gravitational potential to degree 360 Using 30' mean anomalies, *The Ohio State University Department of Geodetic Science and Surveying, Report No. 376*, Columbus, 1986.
- Rizos, C., An efficient computer technique for the evaluation of geopotential from spherical harmonic models, *Aust. J. Geod. Photo. Surv.*, 31, 161-169, 1979.
- Schwiderski, E.W., On charting global ocean tides, *Reviews of Geophysics and Space Physics*, 18, 243-268, 1980.
- Schwiderski, E.W., Global ocean tides, part V: The diurnal principal lunar tide (O1), *Atlas of Tidal Charts and Maps*, 1981.
- Schwiderski, E.W., Atlas of ocean tidal charts and maps, part I: The semi-diurnal principal lunar tide M2, *Marine Geodesy*, 6, 219-265, 1983.
- Sverdrup, H.U., M.W. Johnson, and R.H. Fleming, *The Oceans, Their Physics, Chemistry, and General Biology*, Prentice-Hall, Inc., New York, 1946.
- Tabata, S., B. Thomas, and D. Ramsden, Annual and interannual variability of steric sea level along line P in the Northeast Pacific Ocean, *Journal of Physical Oceanography*, 16, 1378-1398, 1986.
- Tai, C.K., On estimating the basin-scale ocean circulation from satellite altimetry, *Journal of Geophysical Research*, in press, 1988.
- Tai, C.K. and L.L. Fu, On crossover adjustment in satellite altimetry and its oceanographic implications, *Journal of Geophysical Research*, 91, 2549-2554, 1986.
- Tai, C.K. and C. Wunsch, Absolute measurement of the dynamic topography of the Pacific Ocean by satellite altimetry, *Nature*, 301, 408-410, 1983.
- Tai, C.K. and C. Wunsch, An estimate of global absolute dynamic topography, *Journal of Physical Oceanography*, 14, 457-463, 1984.
- Tapley, B.D., J.B. Lundberg, and G.H. Born, The SEASAT altimeter wet tropospheric range correction, *Journal of Geophysical Research*, 87, 3179-3188, 1982.
- Tapley, B.D., R.S. Nerem, C.K. Shum, J.C. Ries, and D.N. Yuan, Determination of the general ocean circulation from a joint gravity field solution, *Geophysical Research Letters*, 15, 1109-1112, 1988.
- Tapley, B.D., and G.W. Rosborough, Geographically correlated orbit error and its effect on satellite altimeter missions, *Journal of Geophysical Research*, 90, 11,817-11,831, 1985.
- VanDam, T.M., and J.M. Wahr, A comparison of NMC and FNOC sea level pressure values, In: Chelton, D.B., WOCE/NASA Altimeter Algorithm Workshop, *U.S. WOCE Technical Report No. 2, Appendix*, U.S. Planning Office for WOCE, College Station, Texas, 1988.

- Wagner, C.A., Radial variations of a satellite due to gravitational errors: Implications for satellite altimetry, *Journal of Geophysical Research*, 90, 3027-3036, 1985.
- Wahr, J.M., The tidal motions of a rotating, elliptical, elastic, and oceanless Earth. Ph.D. Dissertation, University of Colorado, Boulder, 1979.
- Wahr, J.M., Body tides on an elliptical, rotating, elastic, and oceanless Earth, *Geophysical Journal of the Royal Astronomy Society*, 64, 674-703, 1981.
- Walsh, E.J., F.C. Jackson, E.A. Uliana, and R.N. Swift, Observations on electromagnetic bias in radar surface measurements, *Journal of Geophysical Research*, in press, 1988.
- Witter, D.L., and D.B. Chelton, Estimation of temporal variability of sea-state bias in altimeter height measurements, *Journal of Geophysical Research*, in press, 1988.
- Wunsch, C., Bermuda sea level in relation to tides, weather and baroclinic fluctuations, *Reviews of Geophysics and Space Physics*, 10, 1-50, 1972.
- Wunsch, C., and E.M. Gaposchkin, On using satellite altimetry to determine the general circulation of the oceans with application to geoid improvement. *Reviews of Geophysics and Space Physics*, 18, 725-745, 1980.
- Zschau, J., Tidal friction in the solid Earth: Constraints from the Chandler wobble period. in *Space Geodesy and Geodynamics*, edited by A. Anderson and A. Cazenave, Academic Press, Orlando, Florida, 1986.

Appendix A
Normalized Harmonic Coefficients
for Gravitational Model PGS-3337

Table A1: Zonal Coefficients*

Index n n	Value	Index n n	Value	Index n n	Value	Index n n	Value
2 0	-484.1656500	3 0	0.9571820	4 0	0.5405444	5 0	0.0684625
6 0	-0.1503586	7 0	0.0908761	8 0	0.0494638	9 0	0.0278850
10 0	0.0543076	11 0	-0.0511112	12 0	0.0351432	13 0	0.0425713
14 0	-0.0207358	15 0	0.0010854	16 0	-0.0064530	17 0	0.0207709
18 0	0.0096273	19 0	-0.0028790	20 0	0.0207688	21 0	0.0078195
22 0	-0.0081746	23 0	-0.0215996	24 0	0.0011656	25 0	0.0066210
26 0	0.0051031	27 0	0.0018909	28 0	-0.0130095	29 0	-0.0009816
30 0	0.0065626	31 0	0.0067909	32 0	-0.0077843	33 0	-0.0006345
34 0	-0.0034395	35 0	0.0063067	36 0	-0.0021447	37 0	-0.0056314
38 0	0.0029144	39 0	0.0000275	40 0	-0.0041834	41 0	-0.0014789
42 0	-0.0011013	43 0	0.0053794	44 0	-0.0027156	45 0	-0.0013740
46 0	-0.0044919	47 0	0.0015699	48 0	0.0001373	49 0	0.0008193
50 0	-0.0008198						

*Units: Normalized spherical harmonic coefficients $\times 10^6$

Table A2: Sectorial and Tesseral Coefficients*

Index		Value		Index		Value		Index		Value	
n	m	\check{C}_{nm}	\check{S}_{nm}	n	m	\check{C}_{nm}	\check{S}_{nm}	n	m	\check{C}_{nm}	\check{S}_{nm}
2	2	2.4384570	-1.3996477								
3	1	2.0297232	0.2497581	3	2	0.9040244	-0.6212002	3	3	0.7211468	1.4149545
4	1	-0.5350120	-0.4757175	4	2	0.3495536	0.6620689	4	3	0.9916968	-0.2011676
4	4	-0.1897973	0.3079724								
5	1	-0.0590659	-0.0964453	5	2	0.6521775	-0.3224412	5	3	-0.4505260	-0.2131386
5	4	-0.2961543	0.0505913	5	5	0.1732092	-0.6670911				
6	1	-0.0793195	0.0258578	6	2	0.0472462	-0.3709653	6	3	0.0609706	0.0085775
6	4	-0.0900998	-0.4730292	6	5	-0.2663577	-0.5372075	6	6	0.0092345	-0.2364160
7	1	0.2740262	0.0978940	7	2	0.3224936	0.0897224	7	3	0.2530117	-0.2141704
7	4	-0.2772617	-0.1226989	7	5	0.0005335	0.0169355	7	6	-0.3585086	0.1513635
7	7	0.0028341	0.0236784								
8	1	0.0249885	0.0545856	8	2	0.0767725	0.0634442	8	3	-0.0152216	-0.0890810
8	4	-0.2493460	0.0702894	8	5	-0.0233892	0.0871480	8	6	-0.0655223	0.3112655
8	7	0.0692611	0.0742690	8	8	-0.1221461	0.1203348				
9	1	0.1474132	0.0188289	9	2	0.0258474	-0.0322596	9	3	-0.1576455	-0.0786196
9	4	-0.0093889	0.0189401	9	5	-0.0151787	-0.0562751	9	6	0.0663980	0.2201541
9	7	-0.1158350	-0.0973971	9	8	0.1856398	-0.0025585	9	9	-0.0490972	0.0970432
10	1	0.0807568	-0.1345729	10	2	-0.0874570	-0.0476341	10	3	-0.0043457	-0.1570532
10	4	-0.0866512	-0.0784927	10	5	-0.0502397	-0.0514392	10	6	-0.0374000	-0.0777640
10	7	0.0079523	-0.0028456	10	8	0.0418040	-0.0905354	10	9	0.1234468	-0.0396614
10	10	0.0994579	-0.0237717								
11	1	0.0101885	-0.0243460	11	2	0.0164912	-0.0994680	11	3	-0.0266008	-0.1408438
11	4	-0.0402278	-0.0631952	11	5	0.0373221	0.0504256	11	6	0.0013059	0.0347338
11	7	0.0073431	-0.0892183	11	8	-0.0075161	0.0258960	11	9	-0.0330495	0.0417990
11	10	-0.0499940	-0.0168993	11	11	0.0487726	-0.0661239				
12	1	-0.0555233	-0.0465787	12	2	0.0112457	0.0309247	12	3	0.0458629	0.0244329
12	4	-0.0725607	0.0087398	12	5	0.0322399	0.0067284	12	6	0.0045644	0.0433937
12	7	-0.0179661	0.0373275	12	8	-0.0249375	0.0167999	12	9	0.0387240	0.0232196
12	10	-0.0055911	0.0313788	12	11	0.0106416	-0.0061368	12	12	-0.0034619	-0.0101942
13	1	-0.0532121	0.0372845	13	2	0.0491199	-0.0641797	13	3	-0.0173923	0.0964409
13	4	-0.0058617	-0.0087293	13	5	0.0588535	0.0650835	13	6	-0.0316677	-0.0075315
13	7	0.0044026	-0.0062222	13	8	-0.0126548	-0.0089940	13	9	0.0219687	0.0431854
13	10	0.0419293	-0.0357458	13	11	-0.0438858	-0.0020091	13	12	-0.0311963	0.0882460
13	13	-0.0616205	0.0674476								
14	1	-0.0159384	0.0262560	14	2	-0.0367398	-0.0012708	14	3	0.0333131	0.0156274
14	4	-0.0039518	-0.0138027	14	5	0.0251517	-0.0157391	14	6	-0.0175544	0.0048590
14	7	0.0356104	-0.0073149	14	8	-0.0372273	-0.0145805	14	9	0.0288378	0.0267289
14	10	0.0393247	-0.0010323	14	11	0.0142064	-0.0380862	14	12	0.0080382	-0.0308770
14	13	0.0314550	0.0450383	14	14	-0.0520686	-0.0053675				

*Units: Normalized spherical harmonic coefficients $\times 10^6$

Table A2 (Cont.)

Index		Value		Index		Value		Index		Value	
n	m	\hat{C}_{nm}	\hat{S}_{nm}	n	m	\hat{C}_{nm}	\hat{S}_{nm}	n	m	\hat{C}_{nm}	\hat{S}_{nm}
15	1	0.0116124	0.0113477	15	2	-0.0187710	-0.0281485	15	3	0.0506067	0.0188997
15	4	-0.0435616	0.0072251	15	5	0.0099448	0.0082018	15	6	0.0345689	-0.0389455
15	7	0.0589244	0.0022536	15	8	-0.0334193	0.0226521	15	9	0.0096318	0.0338673
15	10	0.0122156	0.0155250	15	11	-0.0008985	0.0197894	15	12	-0.0330952	0.0146920
15	13	-0.0279657	-0.0049887	15	14	0.0055563	-0.0254936	15	15	-0.0184062	-0.0060841
16	1	0.0232121	0.0267768	16	2	-0.0189925	0.0285239	16	3	-0.0294152	-0.0231824
16	4	0.0312151	0.0528219	16	5	-0.0115249	-0.0032751	16	6	0.0176320	-0.0305456
16	7	-0.0065322	-0.0073260	16	8	-0.0218456	0.0058808	16	9	-0.0251334	-0.0398066
16	10	-0.0100151	0.0122564	16	11	0.0186485	-0.0024403	16	12	0.0186308	0.0063272
16	13	0.0135104	0.0005987	16	14	-0.0197406	-0.0384888	16	15	-0.0132951	-0.0338681
16	16	-0.0355845	0.0034875								
17	1	-0.0317941	-0.0297425	17	2	-0.0235808	0.0088814	17	3	0.0107801	0.0125267
17	4	-0.0002868	0.0232190	17	5	-0.0126973	0.0003070	17	6	-0.0071378	-0.0344929
17	7	0.0285302	-0.0044582	17	8	0.0374499	0.0041037	17	9	0.0009458	-0.0303421
17	10	0.0018485	0.0195325	17	11	-0.0174222	0.0109267	17	12	0.0282533	0.0196346
17	13	0.0169694	0.0198780	17	14	-0.0140988	0.0116009	17	15	0.0050871	0.0050651
17	16	-0.0284275	0.0027099	17	17	-0.0330494	-0.0188981				
18	1	-0.0005558	-0.0410868	18	2	0.0069349	0.0118244	18	3	0.0038900	-0.0079428
18	4	0.0411995	0.0089301	18	5	0.0011350	0.0215964	18	6	0.0140625	-0.0113927
18	7	0.0088658	0.0026874	18	8	0.0314000	0.0042563	18	9	-0.0189690	0.0329777
18	10	0.0085544	-0.0045773	18	11	-0.0087237	0.0036823	18	12	-0.0286115	-0.0170258
18	13	-0.0063298	-0.0350286	18	14	-0.0092304	-0.0119446	18	15	-0.0395597	-0.0213357
18	16	0.0126186	0.0068064	18	17	0.0043096	0.0057919	18	18	0.0018849	-0.0091305
19	1	-0.0124700	0.0015173	19	2	0.0236071	-0.0029895	19	3	-0.0076709	-0.0043472
19	4	0.0142705	-0.0021546	19	5	0.0177141	0.0158947	19	6	-0.0042112	0.0172009
19	7	0.0077884	-0.0043914	19	8	0.0283796	-0.0064579	19	9	-0.0000659	0.0036696
19	10	-0.0284459	-0.0085109	19	11	0.0147770	0.0107568	19	12	-0.0041886	0.0065548
19	13	-0.0065890	-0.0287349	19	14	-0.0052352	-0.0126664	19	15	-0.0187752	-0.0142180
19	16	-0.0197368	-0.0091242	19	17	0.0309428	-0.0134408	19	18	0.0335477	-0.0083386
19	19	-0.0028322	0.0070624								
20	1	0.0071033	-0.0049611	20	2	0.0163019	0.0135437	20	3	0.0001068	0.0231955
20	4	0.0004342	-0.0164203	20	5	-0.0094023	-0.0109890	20	6	0.0147371	0.0044899
20	7	-0.0180190	-0.0010710	20	8	0.0031475	0.0080620	20	9	0.0177625	-0.0006512
20	10	-0.0270448	-0.0038595	20	11	0.0140364	-0.0189409	20	12	-0.0082402	0.0171179
20	13	0.0279658	0.0064038	20	14	0.0106888	-0.0133137	20	15	-0.0250273	-0.0011295
20	16	-0.0090232	-0.0015141	20	17	0.0043520	-0.0127514	20	18	0.0143716	0.0004202
20	19	-0.0043821	0.0107550	20	20	0.0037585	-0.0098325				

Table A2 (Cont.)

Index		Value		Index		Value		Index		Value	
n	m	\hat{C}_{nm}	\hat{S}_{nm}	n	m	\hat{C}_{nm}	\hat{S}_{nm}	n	m	\hat{C}_{nm}	\hat{S}_{nm}
21	1	-0.0192512	0.0254296	21	2	0.0014286	0.0041035	21	3	0.0196252	0.0180480
21	4	-0.0066965	0.0130312	21	5	0.0082475	-0.0081842	21	6	-0.0058985	-0.0008146
21	7	-0.0088360	0.0046374	21	8	-0.0146759	0.0044946	21	9	0.0133162	0.0096379
21	10	-0.0066193	0.0006566	21	11	0.0099835	-0.0340038	21	12	-0.0029253	0.0127369
21	13	-0.0176365	0.0129264	21	14	0.0200320	0.0085101	21	15	0.0163026	0.0111187
21	16	0.0097410	-0.0083932	21	17	-0.0048201	-0.0052835	21	18	0.0235995	-0.0089581
21	19	-0.0282125	0.0165645	21	20	-0.0276594	0.0172521	21	21	0.0051080	-0.0007132
22	1	0.0091469	-0.0089155	22	2	-0.0128659	-0.0094603	22	3	0.0166929	0.0047722
22	4	-0.0014925	0.0214173	22	5	-0.0078069	0.0004808	22	6	0.0175540	0.0007891
22	7	0.0130651	0.0050588	22	8	-0.0263183	0.0028798	22	9	0.0073895	0.0089912
22	10	0.0051069	0.0247673	22	11	-0.0057688	-0.0180809	22	12	0.0058936	-0.0089804
22	13	-0.0168220	0.0192046	22	14	0.0098122	0.0094007	22	15	0.0256075	0.0037095
22	16	0.0020675	-0.0077905	22	17	0.0107559	-0.0136371	22	18	0.0086796	-0.0138048
22	19	0.0108293	-0.0027261	22	20	-0.0178454	0.0200787	22	21	-0.0300375	0.0227186
22	22	-0.0141302	0.0005404								
23	1	0.0043670	0.0172342	23	2	-0.0024637	-0.0097237	23	3	-0.0145453	-0.0151899
23	4	-0.0159576	0.0050861	23	5	0.0054845	-0.0040551	23	6	-0.0114720	0.0196064
23	7	-0.0045116	0.0041084	23	8	0.0036794	-0.0030859	23	9	-0.0039035	-0.0176805
23	10	0.0154404	-0.0020850	23	11	0.0047924	0.0136328	23	12	0.0148932	-0.0156936
23	13	-0.0092427	-0.0055774	23	14	0.0060158	-0.0015489	23	15	0.0176424	-0.0039893
23	16	0.0077656	0.0093697	23	17	-0.0027079	-0.0118380	23	18	0.0075118	-0.0110897
23	19	-0.0079452	0.0102588	23	20	0.0081034	-0.0071687	23	21	0.0158030	0.0119512
23	22	-0.0185130	0.0033097	23	23	0.0017658	-0.0127841				
24	1	-0.0004696	-0.0085109	24	2	-0.0027576	0.0086734	24	3	0.0029145	-0.0101675
24	4	0.0079801	0.0100926	24	5	-0.0105777	-0.0117702	24	6	0.0066700	0.0043849
24	7	-0.0041725	0.0019035	24	8	0.0160408	-0.0029408	24	9	-0.0103387	-0.0165226
24	10	0.0109150	0.0179745	24	11	0.0087360	0.0192878	24	12	0.0111952	-0.0067891
24	13	-0.0010719	0.0019853	24	14	-0.0198960	-0.0004356	24	15	0.0060664	-0.0146466
24	16	0.0098660	0.0008285	24	17	-0.0114726	-0.0044906	24	18	-0.0007542	-0.0089183
24	19	-0.0055087	-0.0077306	24	20	-0.0069453	0.0059256	24	21	0.0067275	0.0107402
24	22	0.0039722	-0.0034609	24	23	-0.0073000	-0.0090084	24	24	0.0086518	-0.0033677
25	1	0.0095096	-0.0065503	25	2	0.0249063	0.0138027	25	3	-0.0128976	-0.0082625
25	4	0.0075963	0.0027866	25	5	-0.0082377	-0.0017005	25	6	0.0105650	0.0067270
25	7	0.0034643	-0.0107341	25	8	0.0091662	-0.0016885	25	9	-0.0320892	0.0115912
25	10	0.0086007	-0.0074088	25	11	0.0046767	0.0080022	25	12	-0.0085846	0.0105495
25	13	0.0091663	-0.0130649	25	14	-0.0193783	0.0103056	25	15	-0.0066203	-0.0056828
25	16	0.0024850	-0.0151162	25	17	-0.0112815	-0.0019437	25	18	0.0009068	-0.0102946
25	19	0.0066907	0.0089978	25	20	-0.0064345	-0.0021631	25	21	0.0100724	0.0059817
25	22	-0.0119880	0.0035526	25	23	0.0081233	-0.0109665	25	24	0.0048573	-0.0100043
25	25	0.0083645	0.0017158								

Table A2 (Cont.)

Index		Value		Index		Value		Index		Value	
n	m	\hat{C}_{nm}	\hat{S}_{nm}	n	m	\hat{C}_{nm}	\hat{S}_{nm}	n	m	\hat{C}_{nm}	\hat{S}_{nm}
26	1	0.0030019	-0.0117506	26	2	-0.0035814	0.0081342	26	3	0.0099405	-0.0021139
26	4	0.0165528	-0.0070643	26	5	0.0028367	0.0093962	26	6	0.0157196	-0.0029575
26	7	-0.0034590	-0.0001812	26	8	0.0050364	0.0006736	26	9	-0.0077200	0.0045272
26	10	-0.0141536	-0.0060978	26	11	-0.0023025	-0.0002385	26	12	-0.0161927	0.0015932
26	13	0.0007477	0.0014675	26	14	0.0069424	0.0079369	26	15	-0.0143425	0.0074629
26	16	0.0036108	-0.0089653	26	17	-0.0081196	0.0064669	26	18	-0.0123896	0.0079717
26	19	-0.0002662	0.0051182	26	20	0.0060273	-0.0125158	26	21	-0.0063575	0.0004412
26	22	0.0109934	0.0081949	26	23	0.0004272	0.0132559	26	24	0.0044076	0.0132831
26	25	0.0022570	-0.0009001	26	26	0.0015921	0.0018733				
27	1	0.0088423	-0.0002753	27	2	0.0096834	0.0041669	27	3	-0.0033344	0.0060591
27	4	-0.0004915	0.0039518	27	5	0.0125121	0.0117153	27	6	0.0015908	0.0016261
27	7	-0.0108002	-0.0057679	27	8	0.0015169	-0.0139078	27	9	0.0000055	0.0105107
27	10	-0.0107810	0.0006424	27	11	0.0025283	-0.0087665	27	12	-0.0070685	-0.0010254
27	13	-0.0037410	-0.0030932	27	14	0.0138563	0.0120588	27	15	-0.0050362	0.0009445
27	16	0.0036417	-0.0009229	27	17	0.0047040	0.0011607	27	18	-0.0033514	0.0113172
27	19	-0.0004843	-0.0043194	27	20	0.0014266	0.0012122	27	21	0.0064945	-0.0056510
27	22	-0.0042642	0.0024385	27	23	-0.0041268	-0.0090180	27	24	-0.0012325	-0.0007562
27	25	0.0095805	0.0046197	27	26	-0.0073973	-0.0038020	27	27	0.0065287	0.0011284
28	1	-0.0052930	0.0064480	28	2	-0.0159019	-0.0106964	28	3	0.0012919	0.0079521
28	4	0.0015120	0.0050102	28	5	0.0034809	-0.0061607	28	6	0.0022920	0.0054860
28	7	0.0022904	0.0011477	28	8	0.0028023	-0.0037919	28	9	0.0122701	-0.0027978
28	10	-0.0073381	0.0093021	28	11	-0.0025814	0.0010810	28	12	0.0018479	0.0111432
28	13	0.0024976	0.0051659	28	14	-0.0074107	-0.0091686	28	15	-0.0138245	-0.0009444
28	16	-0.0036740	-0.0137897	28	17	0.0126464	-0.0024649	28	18	0.0032074	-0.0032418
28	19	0.0024131	0.0208553	28	20	-0.0012536	0.0037051	28	21	0.0078252	0.0051142
28	22	0.0002328	-0.0053691	28	23	0.0040197	0.0030962	28	24	0.0097168	-0.0137641
28	25	0.0051804	-0.0180963	28	26	0.0086539	0.0040306	28	27	-0.0072826	0.0023712
28	28	0.0065692	0.0047376								
29	1	0.0047544	-0.0086552	29	2	0.0038977	0.0016927	29	3	-0.0001177	-0.0068315
29	4	-0.0219494	-0.0053607	29	5	-0.0006901	0.0058282	29	6	0.0069358	0.0069131
29	7	-0.0036988	-0.0054774	29	8	-0.0094025	0.0070995	29	9	-0.0057161	0.0008377
29	10	0.0084473	0.0027070	29	11	-0.0035320	0.0049963	29	12	-0.0014273	-0.0047587
29	13	-0.0011958	-0.0013168	29	14	-0.0047890	-0.0031645	29	15	-0.0105894	-0.0064774
29	16	0.0004586	-0.0176289	29	17	0.0017889	-0.0030820	29	18	-0.0063539	-0.0020186
29	19	-0.0070300	0.0051882	29	20	-0.0061538	0.0017612	29	21	-0.0062716	-0.0034092
29	22	0.0117100	0.0021630	29	23	-0.0011636	0.0014451	29	24	-0.0009394	-0.0019586
29	25	0.0036539	0.0058047	29	26	0.0089047	-0.0097453	29	27	-0.0065858	-0.0009247
29	28	0.0068660	-0.0041730	29	29	0.0109883	-0.0066971				

Table A2 (Cont.)

Index		Value		Index		Value		Index		Value	
n	m	\hat{C}_{nm}	\hat{S}_{nm}	n	m	\hat{C}_{nm}	\hat{S}_{nm}	n	m	\hat{C}_{nm}	\hat{S}_{nm}
30	1	-0.0019517	0.0044554	30	2	-0.0158165	-0.0026440	30	3	0.0046248	-0.0125008
30	4	-0.0010948	-0.0009031	30	5	0.0035076	-0.0127858	30	6	0.0053594	0.0059257
30	7	0.0089083	0.0044444	30	8	0.0032380	0.0073297	30	9	-0.0044368	-0.0012839
30	10	0.0012959	-0.0020553	30	11	-0.0129708	0.0079889	30	12	0.0158767	-0.0083183
30	13	0.0125951	0.0025197	30	14	0.0054802	0.0055548	30	15	-0.0019350	-0.0006487
30	16	-0.0094676	-0.0010710	30	17	-0.0046319	-0.0058023	30	18	-0.0096440	-0.0072801
30	19	-0.0106436	-0.0004667	30	20	-0.0044492	0.0081580	30	21	-0.0063122	-0.0053534
30	22	-0.0013765	-0.0037487	30	23	0.0031987	-0.0065320	30	24	-0.0023974	-0.0029113
30	25	0.0035636	-0.0137546	30	26	0.0004645	0.0088991	30	27	-0.0062259	0.0100270
30	28	-0.0058958	-0.0056417	30	29	0.0022004	0.0024606	30	30	0.0000369	0.0054104
31	1	0.0123966	-0.0133920	31	2	0.0062312	0.0073478	31	3	-0.0098929	-0.0086094
31	4	0.0082555	-0.0059797	31	5	-0.0056228	0.0041428	31	6	-0.0022529	0.0015104
31	7	0.0007597	-0.0034036	31	8	0.0027932	0.0011164	31	9	-0.0049545	0.0026202
31	10	0.0017236	-0.0056054	31	11	0.0014235	0.0184336	31	12	0.0044608	0.0019740
31	13	0.0082076	0.0049045	31	14	-0.0075685	0.0044954	31	15	0.0018512	-0.0015486
31	16	-0.0076382	0.0032155	31	17	-0.0017664	0.0058887	31	18	-0.0027338	0.0008151
31	19	0.0022421	0.0014449	31	20	-0.0023965	0.0031552	31	21	-0.0046666	0.0039554
31	22	-0.0053576	-0.0084673	31	23	0.0090894	0.0069073	31	24	-0.0022912	-0.0009191
31	25	-0.0150768	-0.0007802	31	26	-0.0116717	0.0005852	31	27	0.0018359	0.0102100
31	28	0.0081443	0.0037476	31	29	-0.0030838	-0.0039159	31	30	-0.0015562	-0.0056560
31	31	-0.0095662	-0.0019151								
32	1	-0.0039150	0.0038645	32	2	0.0062054	-0.0013949	32	3	-0.0034991	0.0011708
32	4	0.0023375	-0.0090753	32	5	0.0060996	-0.0052047	32	6	-0.0031160	-0.0026790
32	7	0.0003478	0.0011010	32	8	0.0131772	0.0089077	32	9	0.0037204	0.0019251
32	10	-0.0000303	-0.0094268	32	11	-0.0064033	0.0042553	32	12	-0.0115231	0.0131114
32	13	0.0062567	0.0037410	32	14	-0.0016992	0.0038074	32	15	0.0043633	-0.0068677
32	16	-0.0007112	0.0007098	32	17	-0.0022202	0.0093064	32	18	0.0086587	-0.0002886
32	19	0.0022833	-0.0007834	32	20	0.0026235	0.0005804	32	21	-0.0019873	0.0079082
32	22	-0.0090984	-0.0024658	32	23	0.0077281	-0.0009744	32	24	-0.0048648	0.0025622
32	25	-0.0164710	-0.0036198	32	26	0.0039838	-0.0018336	32	27	-0.0036434	-0.0073124
32	28	0.0020392	-0.0016840	32	29	-0.0003822	0.0040324	32	30	-0.0057494	-0.0001395
32	31	-0.0064992	-0.0006561	32	32	0.0037483	0.0008196				

Table A2 (Cont.)

Index		Value		Index		Value		Index		Value	
n	m	\bar{C}_{nm}	\bar{S}_{nm}	n	m	\bar{C}_{nm}	\bar{S}_{nm}	n	m	\bar{C}_{nm}	\bar{S}_{nm}
33	1	-0.0018275	-0.0034699	33	2	-0.0030200	0.0034050	33	3	-0.0049003	0.0025674
33	4	-0.0035443	-0.0030385	33	5	-0.0022081	0.0060028	33	6	0.0021330	-0.0028503
33	7	-0.0080898	0.0012042	33	8	0.0035803	0.0090523	33	9	-0.0014055	0.0062150
33	10	-0.0079085	-0.0025510	33	11	0.0014964	-0.0086573	33	12	-0.0018620	0.0078886
33	13	0.0051816	0.0043989	33	14	0.0025495	0.0014549	33	15	-0.0050593	-0.0029964
33	16	0.0015799	0.0020821	33	17	-0.0022586	0.0084516	33	18	-0.0081275	-0.0034829
33	19	0.0105797	0.0006831	33	20	0.0000449	-0.0050733	33	21	0.0016450	0.0051414
33	22	-0.0067226	-0.0132874	33	23	-0.0011960	-0.0086393	33	24	0.0082599	-0.0055482
33	25	0.0022069	-0.0083427	33	26	0.0106091	0.0034611	33	27	-0.0021073	0.0023028
33	28	-0.0000216	0.0010238	33	29	-0.0165246	0.0043071	33	30	-0.0007327	-0.0182026
33	31	0.0027262	0.0004076	33	32	0.0063910	-0.0056685	33	33	0.0023107	0.0078022
34	1	-0.0044522	0.0005215	34	2	0.0040159	0.0055831	34	3	0.0135866	0.0069395
34	4	-0.0045458	-0.0024391	34	5	-0.0019001	0.0017889	34	6	0.0035866	0.0077565
34	7	0.0005908	-0.0036027	34	8	-0.0108472	0.0008693	34	9	0.0027208	0.0051107
34	10	-0.0066711	-0.0029991	34	11	-0.0056830	-0.0005002	34	12	0.0121840	-0.0031163
34	13	-0.0040485	0.0028989	34	14	-0.0012525	0.0084437	34	15	0.0002431	0.0043708
34	16	-0.0027068	-0.0054382	34	17	-0.0046797	0.0002231	34	18	-0.0106057	-0.0049166
34	19	-0.0000648	0.0024214	34	20	0.0056330	-0.0051055	34	21	-0.0000617	-0.0044043
34	22	-0.0024326	0.0058662	34	23	0.0000817	-0.0086306	34	24	0.0047670	0.0046143
34	25	0.0039441	-0.0090266	34	26	0.0017397	-0.0122515	34	27	0.0117818	-0.0036483
34	28	0.0008579	-0.0172784	34	29	0.0038360	-0.0039425	34	30	-0.0185720	-0.0030747
34	31	-0.0034031	0.0009764	34	32	0.0046549	0.0007826	34	33	0.0113769	0.0021850
34	34	-0.0050207	0.0007776								
35	1	-0.0043968	-0.0080248	35	2	-0.0130824	0.0028017	35	3	0.0034020	0.0007837
35	4	0.0020092	-0.0005114	35	5	-0.0070693	-0.0023857	35	6	0.0055046	0.0066974
35	7	-0.0022629	0.0064662	35	8	0.0022389	0.0040781	35	9	-0.0038613	-0.0033280
35	10	-0.0081646	0.0065930	35	11	0.0041020	-0.0014464	35	12	0.0093521	-0.0073669
35	13	0.0002380	0.0026377	35	14	-0.0055772	-0.0050261	35	15	-0.0147471	0.0071380
35	16	-0.0053577	-0.0035805	35	17	0.0011622	-0.0077376	35	18	-0.0036636	-0.0082296
35	19	-0.0014735	-0.0047157	35	20	0.0009028	0.0011911	35	21	0.0087790	0.0011450
35	22	0.0017931	0.0049039	35	23	-0.0056421	-0.0023386	35	24	0.0034076	0.0053646
35	25	0.0054023	0.0005297	35	26	-0.0046852	0.0002217	35	27	0.0107402	-0.0121050
35	28	0.0064711	-0.0152437	35	29	0.0065577	0.0015286	35	30	-0.0025812	0.0036287
35	31	0.0047333	0.0041207	35	32	-0.0055148	-0.0058823	35	33	0.0050045	-0.0032252
35	34	-0.0015967	0.0036688	35	35	-0.0050281	-0.0057999				

Table A2 (Cont.)

Index		Value		Index		Value		Index		Value	
n	m	\hat{C}_{nm}	\hat{S}_{nm}	n	m	\hat{C}_{nm}	\hat{S}_{nm}	n	m	\hat{C}_{nm}	\hat{S}_{nm}
36	1	0.0018957	0.0016095	36	2	-0.0061383	0.0011224	36	3	0.0013769	-0.0098215
36	4	0.0036924	-0.0017350	36	5	-0.0048339	0.0003472	36	6	0.0078002	-0.0018845
36	7	0.0008896	0.0026608	36	8	0.0026375	-0.0026002	36	9	0.0049744	-0.0041979
36	10	0.0025635	0.0029774	36	11	-0.0008336	0.0000839	36	12	0.0022301	-0.0034152
36	13	-0.0059977	0.0045112	36	14	-0.0071148	-0.0043397	36	15	0.0007663	0.0018517
36	16	0.0015270	-0.0010100	36	17	0.0077378	-0.0051656	36	18	0.0018641	0.0054986
36	19	-0.0053334	-0.0017429	36	20	-0.0058142	0.0016376	36	21	0.0057245	-0.0034990
36	22	-0.0002602	-0.0004746	36	23	-0.0017896	0.0000565	36	24	0.0031955	-0.0025567
36	25	0.0027565	0.0125228	36	26	0.0047485	0.0054535	36	27	-0.0073446	0.0073519
36	28	0.0019641	-0.0027457	36	29	0.0027505	-0.0001790	36	30	-0.0082085	0.0034201
36	31	-0.0057383	-0.0034000	36	32	0.0078490	0.0035238	36	33	0.0042232	-0.0062782
36	34	-0.0056281	0.0049513	36	35	-0.0009340	-0.0079309	36	36	0.0022393	-0.0049526
37	1	-0.0005514	-0.0008669	37	2	0.0005968	-0.0093565	37	3	-0.0018981	0.0011347
37	4	0.0037287	-0.0023565	37	5	-0.0059636	0.0040203	37	6	-0.0021949	0.0057925
37	7	0.0042511	0.0064276	37	8	-0.0019373	-0.0044323	37	9	0.0019859	-0.0034700
37	10	-0.0011641	0.0031385	37	11	0.0028840	0.0005254	37	12	-0.0000345	-0.0008069
37	13	0.0001671	-0.0060440	37	14	-0.0054200	-0.0021527	37	15	0.0069177	0.0005220
37	16	0.0007061	0.0121330	37	17	0.0029524	-0.0033368	37	18	0.0020895	0.0018306
37	19	-0.0053365	0.0014460	37	20	-0.0072517	-0.0022524	37	21	0.0016142	-0.0016353
37	22	0.0046787	-0.0001244	37	23	-0.0005769	-0.0001155	37	24	-0.0037193	-0.0046354
37	25	0.0029489	-0.0001239	37	26	0.0035250	0.0077298	37	27	-0.0022459	0.0032774
37	28	0.0122147	0.0050076	37	29	0.0071106	0.0036127	37	30	-0.0060457	0.0111611
37	31	0.0044474	-0.0057427	37	32	-0.0031249	0.0039523	37	33	0.0007835	-0.0152006
37	34	0.0043190	-0.0007410	37	35	-0.0076687	-0.0055042	37	36	-0.0028080	-0.0021425
37	37	0.0041733	-0.0019075								
38	1	0.0038532	-0.0010378	38	2	0.0036451	0.0021050	38	3	0.0027472	0.0018405
38	4	0.0007990	-0.0013187	38	5	-0.0051818	0.0061791	38	6	-0.0114041	0.0016025
38	7	0.0001399	-0.0068405	38	8	0.0007296	0.0044548	38	9	0.0049159	-0.0029647
38	10	0.0003617	-0.0052751	38	11	-0.0008396	0.0057127	38	12	0.0004208	-0.0022974
38	13	-0.0016223	-0.0077326	38	14	-0.0041582	0.0039002	38	15	0.0007391	-0.0029252
38	16	-0.0048063	0.0064294	38	17	0.0016157	0.0035040	38	18	0.0061122	-0.0022844
38	19	0.0011241	-0.0013828	38	20	0.0000315	-0.0007332	38	21	0.0012028	-0.0004093
38	22	0.0013656	0.0055659	38	23	-0.0000968	0.0023371	38	24	-0.0061535	0.0002115
38	25	-0.0011108	0.0015148	38	26	-0.0051763	0.0046574	38	27	-0.0012593	0.0074816
38	28	-0.0047407	-0.0037989	38	29	0.0064826	0.0027000	38	30	0.0007473	0.0023630
38	31	0.0036481	-0.0026939	38	32	0.0043838	0.0030703	38	33	-0.0000454	0.0075786
38	34	-0.0040744	0.0006785	38	35	0.0032108	0.0025251	38	36	0.0006947	-0.0011597
38	37	-0.0023832	0.0019860	38	38	0.0032005	0.0005058				

Table A2 (Cont.)

Index		Value		Index		Value		Index		Value	
n	m	\hat{C}_{nm}	\hat{S}_{nm}	n	m	\hat{C}_{nm}	\hat{S}_{nm}	n	m	\hat{C}_{nm}	\hat{S}_{nm}
39	1	0.0002270	0.0063859	39	2	0.0045582	0.0055301	39	3	-0.0038665	0.0040813
39	4	-0.0033651	-0.0071771	39	5	0.0018477	0.0061390	39	6	-0.0005306	0.0021801
39	7	0.0025637	-0.0003751	39	8	-0.0001843	0.0073218	39	9	0.0040138	0.0042030
39	10	-0.0013638	0.0029006	39	11	0.0108639	0.0014557	39	12	-0.0029223	0.0076250
39	13	-0.0017650	-0.0037241	39	14	-0.0056397	0.0005088	39	15	-0.0056706	0.0021484
39	16	-0.0013408	-0.0007028	39	17	0.0000767	-0.0024847	39	18	0.0020814	-0.0010580
39	19	0.0038589	0.0026518	39	20	0.0010280	-0.0074054	39	21	-0.0046925	-0.0008723
39	22	-0.0047055	-0.0004377	39	23	-0.0026038	0.0024838	39	24	-0.0058847	0.0052090
39	25	-0.0012510	-0.0018020	39	26	-0.0052645	0.0077261	39	27	-0.0070066	-0.0021044
39	28	-0.0034020	-0.0095294	39	29	-0.0015583	-0.0027531	39	30	0.0058733	-0.0096582
39	31	0.0013721	-0.0073797	39	32	0.0010381	0.0062718	39	33	-0.0054922	0.0008433
39	34	-0.0005848	0.0013625	39	35	-0.0113845	0.0030331	39	36	0.0014458	-0.0007617
39	37	-0.0003014	-0.0034608	39	38	-0.0028753	0.0032108	39	39	0.0011866	0.0008285
40	1	0.0008942	-0.0010173	40	2	-0.0034428	0.0028440	40	3	0.0002044	0.0002281
40	4	-0.0008763	-0.0069992	40	5	0.0098638	-0.0009594	40	6	-0.0023640	0.0021471
40	7	-0.0012625	0.0003635	40	8	0.0057442	0.0030076	40	9	-0.0011779	-0.0009034
40	10	-0.0031140	0.0029427	40	11	0.0002609	-0.0001546	40	12	0.0036271	0.0034425
40	13	-0.0056222	-0.0024255	40	14	-0.0000544	0.0019799	40	15	-0.0035319	-0.0015369
40	16	-0.0023262	-0.0052814	40	17	0.0017635	-0.0018111	40	18	0.0010162	0.0000057
40	19	-0.0011293	-0.0013708	40	20	-0.0019202	0.0045548	40	21	-0.0016374	0.0006171
40	22	-0.0092305	-0.0112502	40	23	-0.0015688	-0.0091492	40	24	0.0026753	0.0022915
40	25	0.0020417	-0.0024911	40	26	0.0046273	-0.0004564	40	27	-0.0013353	0.0009105
40	28	0.0021768	0.0043514	40	29	0.0008763	0.0003577	40	30	0.0003238	0.0003866
40	31	-0.0046164	-0.0004605	40	32	-0.0024430	-0.0011967	40	33	-0.0030614	-0.0030055
40	34	0.0048478	0.0009260	40	35	0.0075288	-0.0048124	40	36	-0.0002256	0.0052145
40	37	-0.0041174	0.0021886	40	38	-0.0018050	0.0053467	40	39	0.0043437	0.0019081
40	40	0.0004109	-0.0014801								
41	1	-0.0031183	-0.0044386	41	2	0.0039691	0.0024801	41	3	-0.0011302	0.0035116
41	4	-0.0016740	0.0023849	41	5	0.0025409	-0.0016030	41	6	-0.0003624	-0.0017187
41	7	0.0004366	0.0036379	41	8	-0.0008286	-0.0051112	41	9	-0.0026867	0.0040962
41	10	0.0036057	-0.0005565	41	11	0.0022423	-0.0056500	41	12	-0.0005817	0.0013300
41	13	-0.0022163	0.0031258	41	14	0.0019019	0.0011099	41	15	-0.0011878	0.0006823
41	16	-0.0009858	-0.0012730	41	17	-0.0022272	-0.0005434	41	18	0.0015837	0.0054577
41	19	-0.0026716	-0.0013517	41	20	0.0010010	-0.0028817	41	21	0.0005251	-0.0008362
41	22	-0.0073622	-0.0020207	41	23	0.0008496	-0.0092326	41	24	0.0044653	-0.0001960
41	25	0.0000523	0.0022402	41	26	0.0041957	-0.0049607	41	27	0.0001040	0.0005927
41	28	-0.0008968	-0.0037137	41	29	-0.0046363	0.0034150	41	30	0.0013241	-0.0014048
41	31	0.0077389	0.0006446	41	32	-0.0045952	0.0036365	41	33	-0.0045774	0.0080447
41	34	-0.0013885	0.0012960	41	35	-0.0090238	0.0055850	41	36	0.0019464	-0.0001476
41	37	-0.0000656	-0.0085865	41	38	-0.0083410	0.0019902	41	39	-0.0048634	0.0004196
41	40	0.0017886	-0.0015636	41	41	0.0028263	0.0044759				

Table A2 (Cont.)

Index		Value		Index		Value		Index		Value	
n	m	\hat{C}_{nm}	\hat{S}_{nm}	n	m	\hat{C}_{nm}	\hat{S}_{nm}	n	m	\hat{C}_{nm}	\hat{S}_{nm}
42	1	-0.0023657	0.0013434	42	2	-0.0032449	-0.0031457	42	3	0.0032140	0.0055350
42	4	0.0010282	0.0010182	42	5	-0.0054341	-0.0073984	42	6	0.0000982	-0.0005867
42	7	0.0046906	-0.0059109	42	8	0.0004458	0.0011354	42	9	0.0009035	0.0004727
42	10	0.0037363	0.0015722	42	11	0.0003804	-0.0004363	42	12	0.0043409	-0.0075812
42	13	-0.0016292	-0.0005399	42	14	-0.0022039	0.0049904	42	15	-0.0014843	0.0056455
42	16	0.0062800	-0.0038373	42	17	-0.0009626	-0.0029507	42	18	-0.0080602	0.0041772
42	19	-0.0041111	0.0000384	42	20	0.0052424	0.0012436	42	21	0.0031245	-0.0025051
42	22	-0.0024791	-0.0019007	42	23	-0.0031335	-0.0019469	42	24	0.0009741	0.0032527
42	25	-0.0040126	0.0002167	42	26	-0.0023263	-0.0047243	42	27	0.0031197	-0.0011269
42	28	-0.0029043	0.0017970	42	29	-0.0040742	-0.0003531	42	30	0.0037692	0.0016684
42	31	0.0044428	0.0038366	42	32	0.0038315	0.0047839	42	33	0.0014834	0.0045704
42	34	0.0027037	0.0064710	42	35	-0.0028880	0.0026029	42	36	0.0030355	-0.0034968
42	37	-0.0040500	0.0027927	42	38	0.0024143	-0.0083113	42	39	0.0005381	0.0091069
42	40	0.0011750	-0.0017936	42	41	0.0002429	0.0006090	42	42	-0.0067076	0.0019551
43	1	0.0011721	-0.0002486	43	2	-0.0060127	-0.0014714	43	3	-0.0020029	-0.0006538
43	4	0.0037895	-0.0009676	43	5	-0.0078834	0.0034299	43	6	0.0071177	-0.0004784
43	7	0.0001988	0.0008394	43	8	-0.0006748	0.0013219	43	9	-0.0004194	-0.0047636
43	10	-0.0021803	0.0008541	43	11	-0.0019889	0.0020233	43	12	-0.0024910	-0.0007121
43	13	0.0017516	-0.0026021	43	14	-0.0019560	0.0016261	43	15	0.0018972	0.0068114
43	16	0.0015647	0.0006363	43	17	0.0016001	-0.0020667	43	18	0.0019041	-0.0037023
43	19	-0.0059481	-0.0019279	43	20	0.0004224	0.0010650	43	21	0.0025747	0.0048355
43	22	0.0010219	-0.0003305	43	23	0.0006998	-0.0068238	43	24	0.0027808	0.0028047
43	25	-0.0017730	0.0006164	43	26	-0.0022067	0.0010605	43	27	0.0035168	0.0013369
43	28	-0.0029683	0.0058574	43	29	-0.0009918	0.0003351	43	30	-0.0061140	-0.0062854
43	31	-0.0017098	-0.0006566	43	32	-0.0029172	0.0047183	43	33	0.0027199	-0.0010961
43	34	0.0023363	-0.0019139	43	35	-0.0014155	0.0047145	43	36	-0.0015877	-0.0007543
43	37	0.0005244	0.0045486	43	38	-0.0033825	0.0004931	43	39	0.0014075	-0.0022824
43	40	0.0070392	-0.0000301	43	41	-0.0028092	-0.0000445	43	42	-0.0032828	0.0017616
43	43	-0.0012910	-0.0068244								

C-2

Table A2 (Cont.)

Index		Value		Index		Value		Index		Value	
n	m	\bar{C}_{nm}	\bar{S}_{nm}	n	m	\bar{C}_{nm}	\bar{S}_{nm}	n	m	\bar{C}_{nm}	\bar{S}_{nm}
44	1	0.0030933	0.0005288	44	2	0.0011230	0.0025701	44	3	0.0044653	-0.0046766
44	4	0.0015703	-0.0021859	44	5	0.0027613	-0.0006770	44	6	-0.0048461	0.0034748
44	7	0.0033008	0.0068248	44	8	-0.0030241	-0.0001415	44	9	0.0018673	-0.0057182
44	10	-0.0022759	-0.0035866	44	11	-0.0014501	0.0001103	44	12	-0.0003740	0.0001638
44	13	0.0027419	-0.0006192	44	14	-0.0008113	-0.0041948	44	15	0.0008407	-0.0042558
44	16	0.0035384	0.0016482	44	17	0.0021674	0.0040503	44	18	0.0032382	-0.0030356
44	19	0.0011996	-0.0012492	44	20	-0.0025220	-0.0023839	44	21	-0.0046136	-0.0018758
44	22	0.0043656	0.0021939	44	23	0.0011652	0.0037045	44	24	0.0024770	-0.0026138
44	25	-0.0005809	0.0006284	44	26	-0.0028711	-0.0000539	44	27	0.0024393	-0.0021295
44	28	-0.0017790	0.0027582	44	29	-0.0060988	0.0020602	44	30	0.0039433	0.0015203
44	31	0.0004585	0.0023182	44	32	-0.0026680	0.0019143	44	33	-0.0033097	-0.0009009
44	34	-0.0030429	0.0030820	44	35	-0.0040136	-0.0031107	44	36	0.0005689	-0.0062107
44	37	0.0086213	0.0040281	44	38	0.0017826	-0.0046446	44	39	0.0056495	0.0032293
44	40	-0.0043622	0.0033921	44	41	0.0009062	-0.0011726	44	42	-0.0024525	-0.0028307
44	43	0.0048498	-0.0045611	44	44	0.0049895	0.0004791				
45	1	0.0039120	-0.0045045	45	2	-0.0017563	-0.0015854	45	3	-0.0042169	-0.0013700
45	4	0.0035655	-0.0005552	45	5	0.0019740	0.0007594	45	6	-0.0012634	-0.0031103
45	7	0.0000167	0.0030308	45	8	-0.0019403	0.0005683	45	9	0.0032456	-0.0032031
45	10	0.0012890	0.0006452	45	11	-0.0004238	-0.0002663	45	12	-0.0035184	-0.0028352
45	13	-0.0024667	0.0006540	45	14	0.0024506	-0.0017663	45	15	-0.0014154	0.0019174
45	16	0.0029974	-0.0002625	45	17	0.0020852	0.0007579	45	18	-0.0008086	-0.0040218
45	19	-0.0026039	-0.0024556	45	20	0.0031174	0.0020391	45	21	-0.0024184	-0.0024014
45	22	0.0023649	0.0024350	45	23	0.0003647	0.0007381	45	24	-0.0054320	0.0032461
45	25	0.0041066	-0.0028570	45	26	-0.0015340	0.0020819	45	27	-0.0038419	0.0003745
45	28	0.0057263	-0.0003848	45	29	-0.0057646	-0.0031056	45	30	-0.0006261	-0.0001344
45	31	-0.0007318	-0.0024597	45	32	-0.0027631	-0.0014790	45	33	-0.0038803	-0.0026021
45	34	-0.0009224	0.0027862	45	35	-0.0034394	0.0048300	45	36	-0.0056852	0.0050022
45	37	-0.0051387	0.0025471	45	38	-0.0028375	0.0028997	45	39	-0.0022924	-0.0042720
45	40	0.0012590	-0.0031147	45	41	0.0003862	0.0002223	45	42	-0.0014105	-0.0084268
45	43	0.0003308	0.0051031	45	44	0.0090676	0.0006328	45	45	-0.0004950	0.0011089

Table A2 (Cont.)

Index		Value		Index		Value		Index		Value	
n	m	\hat{C}_{nm}	\hat{S}_{nm}	n	m	\hat{C}_{nm}	\hat{S}_{nm}	n	m	\hat{C}_{nm}	\hat{S}_{nm}
46	1	0.0023877	0.0025515	46	2	0.0045601	0.0013881	46	3	-0.0005950	-0.0009489
46	4	0.0021957	-0.0035188	46	5	-0.0045163	-0.0057836	46	6	-0.0038708	0.0006783
46	7	0.0030633	-0.0077433	46	8	0.0002484	0.0038750	46	9	0.0043429	0.0028585
46	10	0.0020757	-0.0002130	46	11	-0.0031726	-0.0015984	46	12	-0.0015536	0.0009250
46	13	-0.0009177	-0.0007372	46	14	-0.0009990	0.0005112	46	15	-0.0034983	-0.0013042
46	16	0.0001523	0.0007652	46	17	-0.0004427	0.0002276	46	18	0.0012296	-0.0019324
46	19	0.0007215	-0.0026773	46	20	-0.0021112	-0.0024835	46	21	-0.0044822	0.0014555
46	22	0.0048424	0.0017839	46	23	0.0014218	0.0026362	46	24	-0.0014666	-0.0025366
46	25	0.0022462	-0.0050091	46	26	0.0015980	0.0056275	46	27	0.0000158	-0.0008807
46	28	0.0003535	-0.0049579	46	29	-0.0015205	-0.0021427	46	30	-0.0028039	-0.0052277
46	31	-0.0016613	-0.0007733	46	32	-0.0009946	-0.0012314	46	33	0.0091666	0.0017335
46	34	-0.0022401	0.0018791	46	35	-0.0040921	0.0008224	46	36	0.0000495	-0.0015733
46	37	-0.0036981	0.0033681	46	38	-0.0029391	-0.0016059	46	39	0.0038667	-0.0014578
46	40	0.0003659	0.0000929	46	41	-0.0014964	-0.0043689	46	42	-0.0016058	0.0058628
46	43	-0.0044804	0.0084582	46	44	0.0019766	-0.0009231	46	45	-0.0004211	0.0029749
46	46	0.0002808	-0.0015660								
47	1	-0.0037995	-0.0018470	47	2	0.0013305	0.0010213	47	3	-0.0024297	0.0022240
47	4	-0.0001314	0.0008074	47	5	-0.0012973	-0.0015340	47	6	0.0013417	-0.0019763
47	7	0.0003561	-0.0046666	47	8	0.0030636	-0.0001732	47	9	-0.0012275	0.0021422
47	10	0.0015623	0.0007857	47	11	0.0018051	-0.0021382	47	12	0.0040333	-0.0005335
47	13	-0.0020252	0.0003843	47	14	0.0000279	-0.0011380	47	15	-0.0012780	-0.0003778
47	16	-0.0025736	-0.0005437	47	17	-0.0018568	0.0023447	47	18	-0.0013676	0.0063322
47	19	0.0023767	0.0005617	47	20	-0.0061786	-0.0001921	47	21	-0.0044729	-0.0007884
47	22	-0.0039504	0.0010899	47	23	0.0031757	0.0021112	47	24	-0.0013638	-0.0016741
47	25	-0.0025570	-0.0063860	47	26	0.0047232	-0.0005936	47	27	-0.0027589	-0.0032204
47	28	0.0028524	-0.0035210	47	29	0.0025492	-0.0003483	47	30	-0.0016257	0.0028612
47	31	0.0007881	0.0012860	47	32	-0.0014444	-0.0003171	47	33	-0.0030037	0.0030690
47	34	-0.0009884	0.0009785	47	35	-0.0043000	0.0013852	47	36	0.0056571	-0.0014459
47	37	0.0056693	0.0009009	47	38	0.0009165	0.0002531	47	39	-0.0005736	0.0064325
47	40	-0.0082015	0.0040078	47	41	-0.0022964	0.0053343	47	42	-0.0035968	-0.0024957
47	43	-0.0013056	-0.0001343	47	44	-0.0011419	0.0039055	47	45	0.0076565	0.0028456
47	46	0.0003788	-0.0015145	47	47	0.0015420	-0.0033260				

Table A2 (Cont.)

Index		Value		Index		Value		Index		Value	
n	m	\hat{C}_{nm}	\hat{S}_{nm}	n	m	\hat{C}_{nm}	\hat{S}_{nm}	n	m	\hat{C}_{nm}	\hat{S}_{nm}
48	1	0.0007189	0.0009549	48	2	0.0039447	0.0012968	48	3	-0.0012278	-0.0001304
48	4	-0.0016028	-0.0004350	48	5	0.0029676	-0.0026525	48	6	0.0018926	0.0043932
48	7	-0.0016395	0.0013703	48	8	0.0018857	0.0017512	48	9	-0.0010174	0.0024432
48	10	-0.0004192	0.0013279	48	11	0.0005319	-0.0003039	48	12	0.0012213	-0.0008504
48	13	0.0027117	0.0009434	48	14	-0.0019135	-0.0005661	48	15	0.0019669	-0.0010383
48	16	-0.0000758	0.0009826	48	17	0.0018096	0.0003278	48	18	-0.0015337	0.0028232
48	19	-0.0003924	0.0024583	48	20	-0.0030523	0.0035667	48	21	0.0003300	-0.0021982
48	22	-0.0035677	0.0018368	48	23	-0.0013436	-0.0002419	48	24	-0.0024117	-0.0012849
48	25	0.0002610	0.0002655	48	26	-0.0012895	-0.0037129	48	27	-0.0043774	0.0040409
48	28	0.0029411	-0.0021944	48	29	-0.0002750	-0.0025582	48	30	-0.0022640	-0.0011125
48	31	-0.0015649	-0.0018695	48	32	0.0003714	-0.0017765	48	33	0.0014045	-0.0004607
48	34	-0.0009394	0.0033857	48	35	-0.0011952	-0.0018035	48	36	-0.0021802	0.0025910
48	37	-0.0029957	-0.0009785	48	38	-0.0069040	-0.0005300	48	39	0.0036105	-0.0059021
48	40	0.0019930	0.0009868	48	41	0.0001972	-0.0065037	48	42	0.0018819	0.0023825
48	43	0.0010389	0.0056010	48	44	0.0006110	-0.0012669	48	45	0.0020826	0.0022432
48	46	-0.0021991	0.0056475	48	47	0.0035071	0.0043794	48	48	0.0029045	-0.0011051
49	1	0.0023387	-0.0005980	49	2	0.0007801	0.0027669	49	3	-0.0016439	0.0021815
49	4	-0.0009181	0.0058899	49	5	0.0006383	0.0004919	49	6	-0.0007761	0.0001936
49	7	0.0007992	0.0007629	49	8	-0.0015791	0.0013665	49	9	-0.0010302	0.0031071
49	10	-0.0029602	0.0002146	49	11	0.0036471	0.0003744	49	12	-0.0032632	-0.0023814
49	13	0.0028872	0.0028859	49	14	0.0005038	-0.0001173	49	15	0.0012757	-0.0006943
49	16	0.0004975	-0.0048412	49	17	-0.0013309	-0.0007282	49	18	-0.0003168	-0.0017333
49	19	-0.0014782	-0.0001211	49	20	0.0047611	0.0005353	49	21	-0.0024984	-0.0028636
49	22	-0.0005218	0.0017922	49	23	0.0032065	0.0009413	49	24	0.0022058	0.0007481
49	25	-0.0020747	0.0022634	49	26	-0.0056583	0.0014661	49	27	-0.0026267	0.0015147
49	28	-0.0005072	-0.0081673	49	29	-0.0017398	0.0023113	49	30	0.0027163	0.0007572
49	31	0.0005365	-0.0047351	49	32	-0.0004455	-0.0041774	49	33	0.0009447	-0.0022208
49	34	0.0042314	0.0000899	49	35	0.0033295	0.0009881	49	36	-0.0017493	0.0024083
49	37	-0.0017024	0.0024717	49	38	0.0008739	-0.0008332	49	39	0.0018330	0.0009432
49	40	-0.0011371	0.0002339	49	41	0.0003935	-0.0037834	49	42	-0.0023583	0.0006942
49	43	0.0037112	-0.0075586	49	44	0.0039455	0.0063597	49	45	0.0023015	-0.0022778
49	46	0.0007307	0.0019710	49	47	0.0004255	-0.0015056	49	48	0.0003664	0.0006131
49	49	0.0007135	0.0011369								

Table A2 (Cont.)

Index		Value		Index		Value		Index		Value	
n	m	\tilde{C}_{nm}	\tilde{S}_{nm}	n	m	\tilde{C}_{nm}	\tilde{S}_{nm}	n	m	\tilde{C}_{nm}	\tilde{S}_{nm}
50	1	0.0019380	-0.0018856	50	2	-0.0033020	-0.0038657	50	3	-0.0010767	-0.0005062
50	4	-0.0066965	0.0019645	50	5	-0.0017818	-0.0017015	50	6	-0.0003600	0.0012664
50	7	0.0028188	0.0028442	50	8	-0.0024931	-0.0005833	50	9	-0.0021321	0.0016423
50	10	-0.0022597	-0.0008336	50	11	-0.0021467	0.0011245	50	12	-0.0015792	0.0043379
50	13	0.0013943	0.0001148	50	14	-0.0023746	0.0013868	50	15	-0.0018172	-0.0014945
50	16	0.0007175	-0.0044253	50	17	0.0013475	-0.0033455	50	18	0.0024525	-0.0024792
50	19	0.0009753	0.0007547	50	20	0.0019704	-0.0010310	50	21	-0.0000851	-0.0000011
50	22	0.0003631	-0.0006919	50	23	-0.0001298	-0.0037551	50	24	0.0062070	0.0011396
50	25	0.0032399	0.0011292	50	26	-0.0037527	0.0001747	50	27	0.0023751	-0.0018076
50	28	-0.0005902	0.0046041	50	29	0.0029357	0.0026527	50	30	0.0025455	0.0033822
50	31	0.0003577	0.0031442	50	32	-0.0017186	0.0018285	50	33	-0.0025683	-0.0017725
50	34	-0.0010921	-0.0010005	50	35	0.0013188	0.0006623	50	36	0.0005842	0.0008776
50	37	-0.0023893	-0.0005954	50	38	-0.0019843	-0.0048631	50	39	-0.0045125	0.0066772
50	40	0.0038308	0.0036611	50	41	-0.0025454	-0.0024214	50	42	0.0026618	-0.0018714
50	43	0.0026755	-0.0054678	50	44	-0.0019064	-0.0020531	50	45	-0.0013891	0.0023028
50	46	-0.0021796	0.0014056	50	47	-0.0038600	-0.0061788	50	48	-0.0021930	-0.0012660
50	49	0.0027190	-0.0036872	50	50	0.0016426	0.0008856				

Appendix B
Tidal Coefficients

Table B1: Ocean Tidal Coefficient Recovery for PGS-3337

Ocean Tidal Constituents			Harmonic Coefficients		Tidal Characteristics		Statistics			
Tide	Degree	Order	A	B	Amp(cm)	Phase(°)	σ_A	σ_B	σ_{Amp}	σ_{Phase}
Sa	2	0	-1.260	-2.487	1.3937	26.865	0.993	0.966	0.971	20.3
Ssa	2	0	1.778	0.821	0.9789	245.221	0.916	0.842	0.903	25.0
Mm	2	0	0.564	-0.146	0.2916	284.543	0.664	0.647	0.662	63.6
Mf	2	0	1.567	0.635	0.8455	247.945	0.537	0.541	0.538	18.3
K ₁	2	1	1.309	-2.154	2.5206	328.721	0.284	0.301	0.296	6.6
O ₁	2	1	-1.757	2.052	2.7014	319.427	0.228	0.220	0.223	4.8
P ₁	2	1	-0.817	0.437	0.9268	298.133	0.296	0.286	0.293	17.8
K ₂	2	2	-0.284	0.160	0.3266	299.417	0.070	0.070	0.069	12.2
M ₂	2	2	-2.053	2.532	3.2597	320.963	0.068	0.072	0.070	1.2
S ₂	2	2	-0.691	0.420	0.8085	301.269	0.073	0.068	0.071	4.9
N ₂	2	2	-0.301	0.641	0.7079	334.831	0.089	0.089	0.088	7.2
T ₂	2	2	0.034	0.091	0.0975	20.297	0.068	0.072	0.071	40.0
K ₁	3	1	-0.817	-0.435	0.9259	61.967	0.127	0.133	0.128	8.2
O ₁	3	1	2.269	0.778	2.3985	71.077	0.215	0.210	0.214	5.0
P ₁	3	1	0.129	0.267	0.2967	25.688	0.139	0.129	0.131	26.5
K ₂	3	2	-0.262	-0.557	0.6156	205.141	0.055	0.050	0.051	5.1
M ₂	3	2	-0.010	-0.073	0.0733	187.917	0.083	0.084	0.084	64.7
S ₂	3	2	-0.237	-0.209	0.3157	228.586	0.055	0.053	0.054	9.8
N ₂	3	2	0.195	-0.036	0.1982	100.428	0.088	0.088	0.087	25.3
T ₂	3	2	-0.077	-0.095	0.1225	219.062	0.055	0.051	0.052	25.0
K ₁	4	1	2.169	0.837	2.3245	248.905	0.425	0.530	0.440	12.8
O ₁	4	1	-1.688	0.235	1.7040	277.924	0.420	0.398	0.419	13.4
P ₁	4	1	-0.375	-0.073	0.3825	259.007	0.425	0.412	0.424	61.8
K ₂	4	2	0.171	-0.021	0.1719	97.120	0.087	0.089	0.086	29.6
M ₂	4	2	0.743	-0.553	0.9259	126.642	0.094	0.098	0.095	6.0
S ₂	4	2	0.363	0.017	0.3633	87.362	0.092	0.103	0.091	16.2
N ₂	4	2	0.086	-0.160	0.1818	151.687	0.098	0.097	0.097	30.9
T ₂	4	2	0.030	0.061	0.0677	25.850	0.107	0.098	0.099	88.8
K ₂	5	2	0.050	0.008	0.0504	81.066	0.073	0.065	0.072	74.4
M ₂	5	2	0.040	0.269	0.2715	8.418	0.075	0.074	0.073	15.8
S ₂	5	2	0.101	0.141	0.1735	35.563	0.088	0.077	0.081	27.9
N ₂	5	2	-0.056	0.166	0.1752	341.260	0.080	0.080	0.079	26.2
T ₂	5	2	0.100	0.055	0.1142	61.088	0.076	0.078	0.076	39.0

Appendix C

Color Plates

Plate 1. A series of graphics depicting the important terms in the ocean variability that effect the estimation of the dynamic topography from altimetry.

(a) The mean value of the sea-state ($W_{\frac{1}{3}}$) over the SEASAT lifetime.

(b) Ocean tide differences ($\langle \eta_T \rangle$) between the Schwiderski (1981, 1982, 1983) and Parke (1982) models at the SEASAT sampled sub-satellite points.

(c) Map of mesoscale energy ($\langle \eta \rangle$) seen from an analysis of the SEASAT data using colinear pass analyses (Cheney *et al.*, 1983).

Plate 2. A comparison of $\bar{\eta}_A$ from PGS-3337 and $\bar{\eta}_\rho$.

Plate 3. The correlation between $\bar{\eta}_\rho$ and $h_{N_{ref}}$ from PGS-3337.

Plate 4. A graphical presentation of the altimeter residuals from the PGS-3337 reference orbits binned within 5-degree blocks.

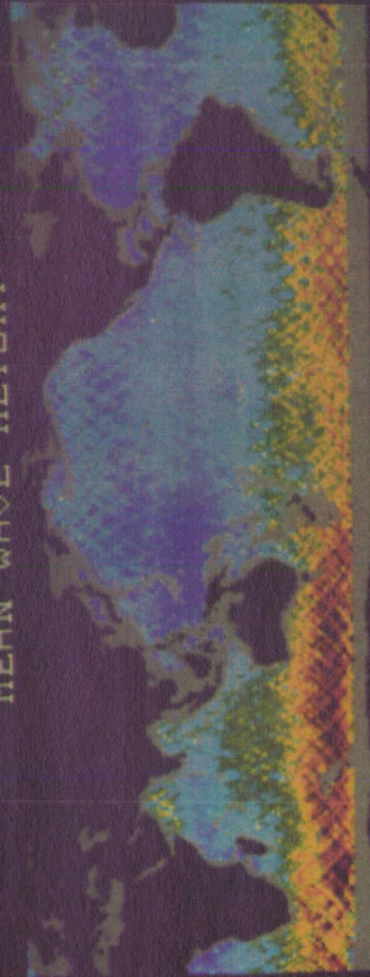
(a) The number of altimeter observations utilized in the PGS-3337 solution present in each of the 5-degree blocks.

(b) The rms of the residuals.

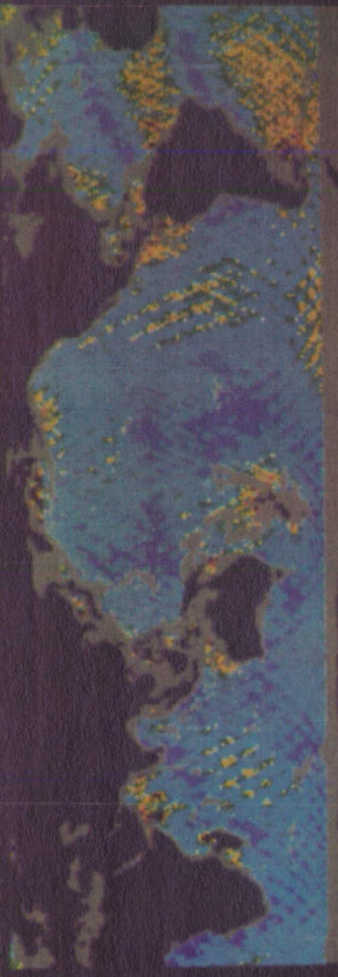
(c) The mean of the residuals.

(d) The mean of the absolute values of the residuals.

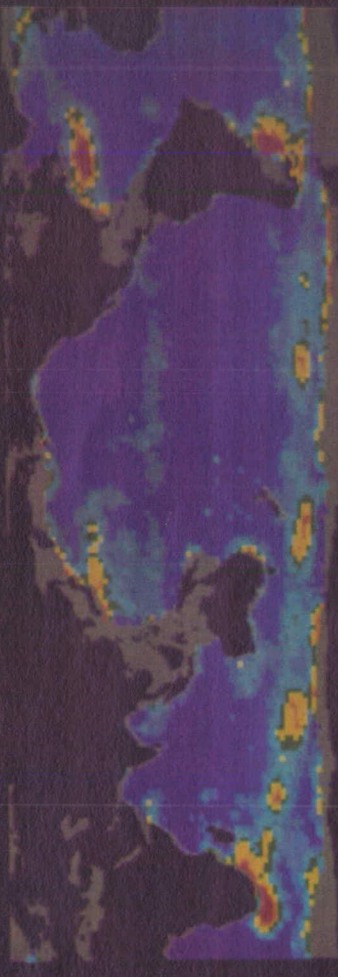
MEAN WAVE HEIGHT



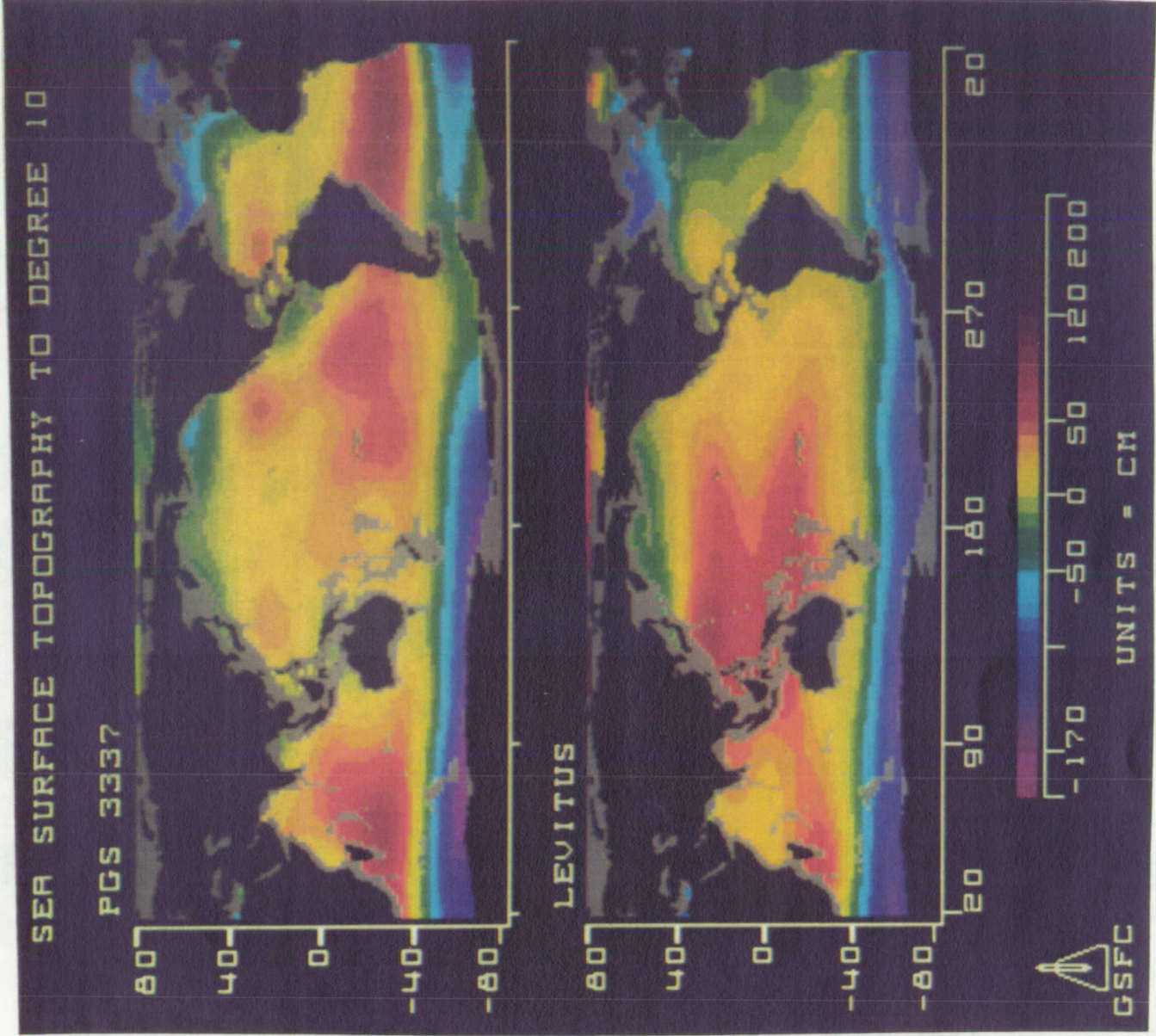
MEAN DIFFERENCES BETWEEN TIDAL MODELS



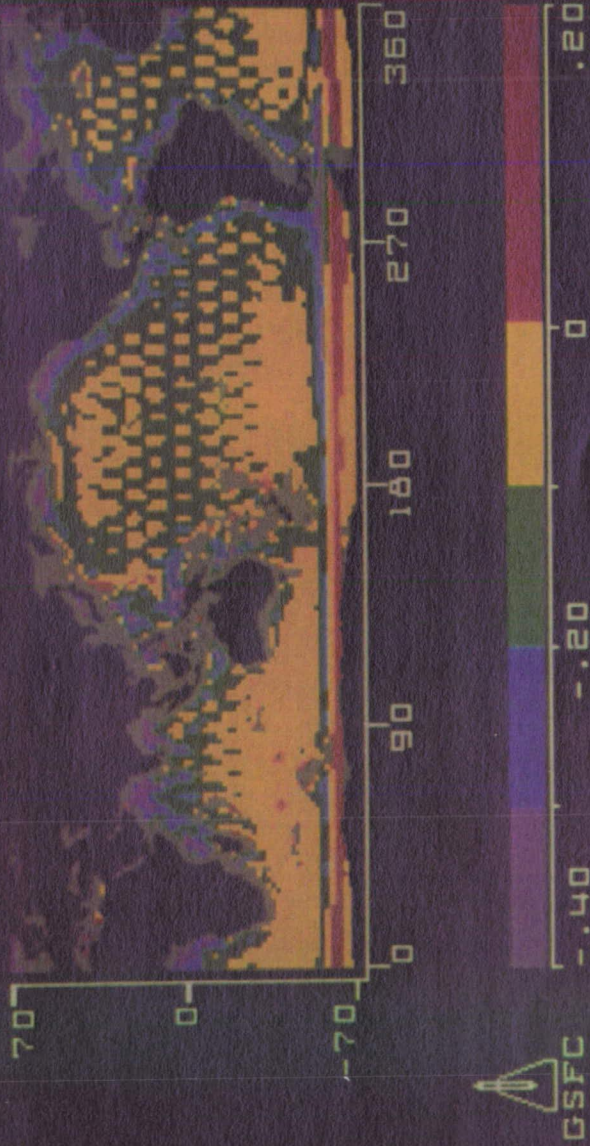
SEA LEVEL VARIABILITY



ORIGINAL PAGE
COLOR PHOTOGRAPH

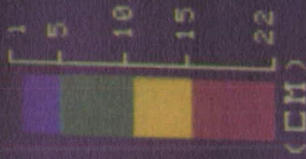


POS 3337 QSST & GEOID CORRELATION



SEASAT - 7/27/78 TO 10/5/78

NUMBER OF
OBS/BIN



BINNED RESIDUALS



RMS



MEAN



MEAN
OF THE
ABS VAL





Report Documentation Page

1. Report No. NASA TM -100735		2. Government Accession No.		3. Recipient's Catalog No.	
4. Title and Subtitle Dynamic Sea Surface Topography, Gravity, and Improved Orbit Accuracies from the Direct Evaluation of SEASAT Altimeter Data				5. Report Date May, 1989	
				6. Performing Organization Code 626	
7. Author(s) J.G. Marsh, F. Lerch, C.J. Koblinsky, S.M. Klosko, J.W. Robbins, R.G. Williamson, and G.B. Patel				8. Performing Organization Report No. 89B0111	
				10. Work Unit No. 161-20-25	
9. Performing Organization Name and Address Code 626 - Space Geodesy Branch Goddard Space Flight Center Greenbelt, MD 20771				11. Contract or Grant No.	
				13. Type of Report and Period Covered Technical Memorandum	
12. Sponsoring Agency Name and Address National Aeronautics and Space Administration Washington, D.C. 20546-0001				14. Sponsoring Agency Code	
15. Supplementary Notes S.M. Klosko, J.W. Robbins, R.G. Williamson, and G.B. Patel are affiliated with ST Systems, Inc., Lanham, Maryland 20906. J.G. Marsh, F. Lerch, and C.J. Koblinsky are at Code 626, GSFC, Greenbelt, Maryland 20771.					
16. Abstract This document describes a method for the simultaneous solution of dynamic ocean topography, gravity and orbits using satellite altimeter data. A GEM-T1 based gravitational model called PGS-3337 that incorporates SEASAT altimetry, surface gravimetry and satellite tracking data has been determined complete to degree and order 50. The altimeter data is utilized as a dynamic observation of the satellite's height above the sea surface with a degree 10 model of dynamic topography being recovered simultaneously with the orbit parameters, gravity and tidal terms in this model. PGS-3337 has a geoid uncertainty of 60 cm RMS globally, with the uncertainty over the altimeter tracked ocean being in the 25 cm range. Doppler determined orbits for SEASAT, show large improvements, with the sub-30 cm radial accuracies being achieved. When altimeter data is used in the orbit determination process, radial orbital accuracies of 20 cm are achieved. The RMS of fit to the altimeter data directly gives 30 cm fits for SEASAT when using PGS-3337 and its geoid and dynamic topography model. Contained in these RMS errors is residual geoid, orbit, tides, mesoscale variability, measurement noise, media modeling errors, and sea state error effects. This performance level is two to three times better than that achieved with earlier GEM models using the dynamic topography from long-term oceanographic averages. The recovered dynamic topography reveals the global long wavelength circulation of the oceans with a resolution of 1500 km. The power in the dynamic topography recovery is now found to be closer to that of oceanographic studies than for previous satellite solutions. This is attributed primarily to the improved modeling of the geoid which has occurred. Study of the altimeter residuals reveals regions where tidal models are poor and sea state effects are major limitations.					
17. Key Words (Suggested by Author(s)) Dynamic Topography Ocean Circulation Satellite Altimetry Gravitational Models			18. Distribution Statement Unclassified - Unlimited Subject categories 46		
19. Security Classif. (of this report) Unclassified		20. Security Classif. (of this page) Unclassified		21. No. of pages 102	22. Price